UNIVERSITY
OF TRENTO - Italy
DEPARTMENT OF INDUSTRIAL ENGINEERING

XXX cycle

Doctoral School in Materials, Mechatronics
and Systems Engineering

Calcium Phosphate Powders for Biomedical Applications:

Synthesis, Thermal Behavior and Non-Conventional Sintering

Matteo Frasnelli

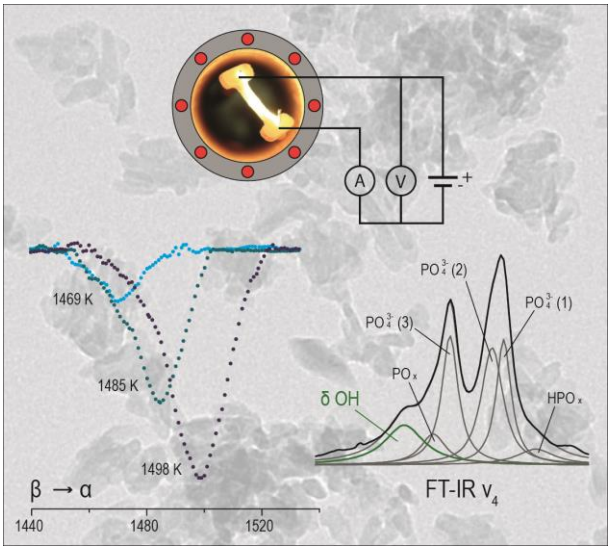

April 2018

CALCIUM PHOSPHATE POWDERS FOR BIOMEDICAL APPLICATIONS:

SYNTHESIS, THERMAL BEHAVIOR AND NON-CONVENTIONAL SINTERING

Matteo Frasnelli

E-mail: matteo.frasnelli@unitn.it

Approved by:

Prof. Vincenzo Maria Sglavo, Advisor
Department of Industrial Engineering
University of Trento, Italy

Prof. Sandra Diré, Advisor
Department of Industrial Engineering
University of Trento, Italy

Ph.D. Commission:

Prof. Gian Domenico Sorarù,
Department of Industrial Engineering
University of Trento, Italy

Prof. Richard Todd,
Department of Materials
University of Oxford, United Kingdom

Dr. Alessandra Sanson,
CNR-ISTEC
Faenza, Italy

University of Trento,

Department of Industrial Engineering

April 2018

University of Trento - Department of Industrial Engineering

Doctoral Thesis

Matteo Frasnelli - 2018
Published in Trento (Italy) – by University of Trento

To my friend Andrea

Abstract

The present work was focused on the synthesis of three different calcium phosphate powders with possible application as bioceramics, their chemical, structural and thermal characterization, and finally their consolidation into dense compounds by conventional and flash sintering techniques.

In the first part, Mg-doped (0 - 2 mol% Mg^{2+}) tricalcium phosphate powders with micrometric size were produced by solid state reaction, and the influence of dopant on their sintering behavior and, specifically, on the β→α phase transition was studied. It was shown that magnesium stabilizes β-phase and ensures, after conventional sintering, much better densification and final mechanical properties. Moreover, annealing treatments on sintered compounds are suitable to convert the retained α- into β-TCP only in presence of Mg.

Un-doped β-TCP was additionally subjected to flash sintering, thus obtaining dense microstructure at temperatures lower than 1000°C in just 10 min and avoiding any phase transition. A specific physical model based on of thermal-balance equations was considered to investigate the flash sintering process in detail; it was possible to point out that thermal runaway is the main mechanisms that triggers the process, which could be described also in terms of electric behavior of the material, real sample temperature and flash onset. Moreover, the observed blackening effect and the development of an additional resistance contribution at the electrodes were taken into account and discussed.

In the second part of the work, Mg-doped (0 - 5 mol% Mg^{2+}) tricalcium phosphate nanometric (~ 20 nm) powders were synthetized by chemical precipitation, thus obtaining highly-defected CDHA easily convertible into β-TCP at 750°C. Magnesium doping was found to inhibit the first crystallization and to promote β-TCP formation directly. The nanopowders were conventionally sintered to produce dense (~90%) β-TCP with sub-micrometric gran size.

Flash sintering was also carried out on the nanopowders, demonstrating that the flash event can occur only after CDHA→β-TCP reaction, since the precursor is too resistive for allowing the electrical current flow. A non-linear electrical behavior was found for the β-phase, associated with the grain growth. Flash sintering was also applied in isothermal mode, producing dense sub-micrometric β-TCP at 900°C in just few seconds. It was also possible to build two maps relating the processing parameters for flash sintering on the basis of thermal model and the material behavior.

Finally, hydroxyapatite nanopowders were synthesized by chemical precipitation with different amount of Sr^{2+} replacing Ca^{2+} into the apatite structure (0 - 100 mol%). The nanopowders were deeply characterized from a morphological, chemical and structural point of view (SEM, TEM, ICP, XRD, FT-IR, ^{31}P-NMR, ^{1}H-NMR, N_2 sorption) finding a relation between the experimental evidences and the amount of Sr.

Table of contents

Chapter I

Introduction

1.1 Calcium Phosphates

1.1.1 Classes of bioceramics

The concept and the definition of "biomaterial" has changed in the last few decades due to the new compounds that incessantly are recognized as suitable for medical applications, leading to a gradual delineation of the early and ambiguous idea of "material able to interact with biological systems". A more complex and commonly accepted definition was proposed by prof. D.F. Williams in 2009 as a result of a detailed argumentation [1]:

"A biomaterial is a substance that has been engineered to take a form which, alone or as part of a complex system, is used to direct, by control of interactions with components of living systems, the course of any therapeutic or diagnostic procedure, in human or veterinary medicine".

Hence, it can be stated that the key factor turning a simple material into a biomaterial is the control of its properties considering both the final biological application and the desired biological response. The "bio" prefix is not strictly related with the biological nature of the material itself (e.g. proteins), but can be assumed as a quality of any classes of material, like biometals (i.e. Ti6Al4V alloy) [2][3], biopolymers (e.g. polylactide PLA) [4], bioglasses (e.g. 45S5®) [5][6], and bioceramics (e.g. hydroxyapatite HA) [7][8]. Therefore, a more useful classification can be based on the biological response induced by the biomaterial, as proposed by prof. L.L. Hench [9]. The work is actually referred to bioceramics, but the description of the implant-tissue interaction could be easily extended to the other classes of materials. However, a bioceramic can be defined as:

- *toxic*, when the material induces the death of the surrounding tissue;
- *non-toxic and biological inactive*, when the body isolates the implant by means of a thick fibrous tissue (i.e. periprosthetic capsule). Also indicated as *almost inert*, these materials are usually nonporous and morphologically fixed to the biological tissue by taking advantage of the surface

irregularities and defects. Examples of inactive bioceramics are alumina [10] and zirconia [11];

- *nontoxic and biologically active* (or *bioactive*), when an interphase forms between the implant and the biological tissue. The bonding layer can be composed by chemical bonds (bioactive fixation), as in the case of surface-active dense ceramics (e.g. dense HA), or it can be characterized by the tissue ingrowth into the porous ceramic (e.g. porous HA) through a biological fixation;

- *non-toxic and resorbable*, when the material gradually dissolves, and the surrounding tissue is stimulated to replace it. Example of bioresorbable ceramics are bioglasses and tricalcium phosphate, TCP [12].

Bioresorbable ceramics are the most promising materials and perfectly fit the latest requirements of tissue engineering, where the implant should not be considered just a substitute of the original biological functionality, but it should restore or improve such function by helping the body to heal itself (regenerative medicine). Regardless of the chemical composition of the released species, the material dissolution rate must at first match the repairing rate of the body tissue, in order to ensure good adhesion and sufficient mechanical strength during the entire treatment. Too slow dissolution leads to excessive elongation of the healing process, whereas too rapid dissolution could induce mechanical instability and, in addition, too high local concentration of released species and cytotoxicity.

Among them, calcium phosphates (CaPs), object of the present study, represent one of the most promising class of biomaterials in the field of bone regeneration.

1.1.2 Bone structure

Due to the main application field of CaPs, a short overview about structure, chemistry, functionalities, and mechanical properties of natural bone is here reported.

Bone is the solid anatomic portion forming the skeletal system of vertebrates, characterized by an extracellular matrix, basically type I collagen (~30 wt%), a mineralized fraction (~60 wt%), and water (~10 wt%). Because of the presence of cells, bones can be considered effectively as alive organs, in spite of the presence of inorganic compounds.

Apart from the quite evident support functionality for the body weight and the articular movements, bones provide protection to vital organs, transmit the sound inside the ears, contain stem cells (marrow), represent a storage for mineral elements, and buffer the pH fluctuation in the blood.

Bone structure is a perfect example of hierarchical organization, where each sub-level is characterized by a specific configuration and role (Fig. I-1). Starting from a macroscopic point of view, many type of morphologies are differentiate inside the human body, on the basis of their respective function: long, short, plate, and irregular. In any case, two main bone tissues are present in various relative amount and position [13]:

- cortical (or compact); the external layer of the bones, with a thickness variable between less than a millimeter and few centimeters, according to the mechanical stress to which is subjected. Porosity is limited to ~6%;

- cancellous (or trabecular); spongy tissue, with ~80% of porosity, placed in the inner part of the bone, constituted by an interconnected framework of rod/plate trabeculae of 50-300 μm, and able to well-support compressive loads.

For what concerns the microscopic level, planar arrangements called lamellae (width 3-7 μm) are identifiable. Such platelets are stacked either according to a random direction, in the range ±30 deg, modelling every single trabecula of the cancellous tissue or wrapped into concentric layers around the so-called Haversian canals, forming cylindrical structures (diameter ~100 μm) named osteons, aligned to the bone direction within the cortical tissue. Yet, lamellae are composed by fibrils of 100 nm in diameter, resulting from the aggregation of collagen (type I) molecules and apatite nanocrystals, regularly placed every ~67 nm along the chains.

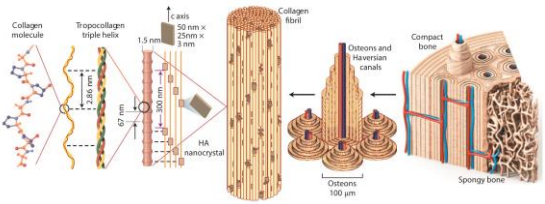

Figure I - 1. Hierarchical structure of human bone. Reproduced from [14].

The bone composition is completed by four main types of cells, located within the solid matrix of the tissue. The first one, osteoblasts, are formed by the differentiation of osteogenic cells in the bone marrow and are responsible of the bone formation. The process occurs in two steps, by secreting the collagen matrix, self-assembled into fibrils, and the subsequential mineralization. As a matter of fact, the interaction between specific anionic proteins and the regularly-sequenced functional groups of the fibrils, leads to the stereochemical orientation of negative charges on the chains, and the consequent nucleation of free Ca^{2+} and PO_4^{-3} ions into apatite. Crystals growth and coarsening are inhibited by the restricted extracellular space among the staggered collagen molecules, and thus the final result is a regular succession of discrete and nanometric HA plates accounting for the bone hardness and isotropy. The bio-mineralization process starts 13 days after the matrix is formed, then proceeds very rapidly, up to 70%, within few days (primary mineralization). The remaining is over several years (secondary mineralization). Therefore, mature osteoblast cells are gradually trapped inside the bone tissue just created, behaving as stress sensors (osteocytes) or physical barrier on the top of the new tissue (lining cells). Finally, the last typology of bone cells is constituted by osteoclasts, responsible for the secretion of specific enzymes able to reabsorb the collagen matrix and solubilized the mineral fraction by locally enhance the acidity. The combined action of osteoblasts (creation) and osteoclasts (destruction) represents a classic dynamic-equilibrium, leading to the complete replacement of the overall human skeleton every ~60 days.

As above introduced, the mineralized fraction of the human bone is basically composed by the so-called biological apatite, i.e. a multi-substituted hydroxyapatite $Ca_{10}(PO_4)_6(OH)_2$, covered with a variable hydrated layer. The most common ions replacing calcium are Na^+, Mg^{2+}, K^+, whereas HPO_4^{2-}, CO_3^{2-}, Cl^- , and F^- can be easily found in place of de-protonate phosphates (B-type substitution) or the hydroxyl groups (A-type substitution) [15]. Consequently, the Ca/P ratio, very significant parameter to identify a calcium phosphate species, presents random deviations (positive or negative) from the HA stoichiometric value of 1.67. For instance, considering the generic formula of B-type carbonated apatite, namely one of the possible (locally) composition of the mineral human bone is

$$Ca_{10-x}(PO_4)_{6-x}(CO_3)_x(OH)_{2-x} \tag{1a}$$

where $0<x<2$, the crystal neutrality imposing an increment of Ca/P up to 2 with the maximum CO_3^{-2} content.

Conversely, the partial hydration of the phosphate groups leads to a decrement of the atomic ratio up to 1.5, according to:

$$Ca_{10-x}(HPO_4)_x(PO_4)_{6-x}(OH)_{2-x} \quad (1b)$$

where *0<x<1*. In general, biological apatites differ from the synthetic ones by the lack of OH^- and the presence of HPO_4^{2-} [16]. The average chemical composition of bone is reported in Tab. I-1, with other human calcified tissues.

	Enamel	*Dentin*	*Bone*	*HA*
Ca^{2+}, wt%	36.5	35.1	34.8	39.6
PO_4^{3-} / HPO_4^{2-}, wt%	54.3	51.8	46.6	56.7
Ca/P, at. ratio	1.63	1.61	1.71	1.67
Na^+, wt%	0.50	0.60	0.9	-
Mg^{2+}, wt%	0.44	1.23	0.72	-
K^+, wt%	0.08	0.05	0.03	-
CO_3^{2-}, wt%	3.5	5.6	7.4	-
F^-, wt%	0.01	0.06	0.03	-
Cl^-, wt%	0.30	0.01	0.13	-
a, ±0.003 Å	9.441	9.421	9.410	9.43
c, ±0.003 Å	6.880	6.887	6.890	6.891

Table I - 1. Chemical composition and structural parameters of human bone, enamel, dentin, and synthetic HA [17].

For what concerns the crystalline structure of biological apatites, detailed investigation is complicated by their nano-sized nature, quite similar to an amorphous material, and by the absence of a reference single crystal, as well. However, the lattice follows most likely the same arrangement of the synthetic HA, i.e. hexagonal $P6_3/m$, with cell parameters variably scattered around the reference values due to the multiplicity of the atomic substituents.

Crystal morphology is described as plate-like shape [18] with thickness of 1.5-9 nm and planar dimensions in the range 10-200 nm, the latest associable to the *a-c* plane of the crystalline cell. Due to the stereospecificity of the biomineralized process, the platelets are oriented with their *c-axis* along the collagen fibrils direction, i.e.

parallel to the bone axis in cortical tissue. The size and the relative dimension of the crystals strongly depends to the health state, the age and the species of the individual, although a single subject always shows a distribution of values.

In conclusion, bones are a perfect example of composite materials with some mechanical properties that exceed those of their single elements and their combination (according to the phase rule). For instance, cortical bone presents fracture toughness and tensile strength larger than synthetic hydroxyapatite. Specifically, collagen matrix is responsible for elasticity and resistance to traction, whereas the mineralized fraction accounts for hardness, toughness, and resistance to compression (Tab. I-2). In addition, the internal architecture of the trabeculae can be reorganized on the basis of the load intensity, as well as the thickness of the cortical tissue [14].

	Compact bone	*Trabecular bone*	*HA*
Young's modulus, GPa	14-20	0.05-0.5	80-110
Tensile strength, MPa	50-150	10-20	50
Compressive strength, MPa	170-193	7-10	400-900
Fracture toughness, MPa $m^{0.5}$	2-12	0.1	0.7-1.2
Strain to failure, %	1-3	5-7	-

Table I - 2. Mechanical properties of compact and trabecular bone tissues, and synthetic dense hydroxyapatite [19].

1.1.3 CaP-bone interaction

As previously anticipated, the most important feature of CaP compounds is their capability to be solubilized by the biological fluids and thereby to promote new bone formation (i.e. osteogenesis). The mechanism is based on the partial dissolution of CaP ceramics and the consequent increment of Ca^{2+} and PO_4^{3-} local concentration at the implant/bone interface. As a result, saturation level is exceeded and re-precipitation as apatite microcrystals occurs on the host-bone surface [20]. The crystallization process may cause the incorporation of other ions (e.g. Mg^{2+}, CO_3^{2-}) and organic macromolecules as proteins and growth factors present in the surrounding biological fluids. Therefore, cell attachment, proliferation and differentiation are facilitated, as well as the secretion of new collagen matrix and the successive bone growth inside the ceramic porosity.

However, several authors [21][22] have suggested that the formation of HA crystals upon the bone mineralization and remodelling processes is intermediated by some transient precursor phases, although the exact mechanism remains controversial. In particular, amorphous calcium phosphate (ACP) has been identified in early mineralized tissue. Successively, ACP directly transforms into stoichiometric HA, or into non-stoichiometric apatites by passing through a further intermediate phase, characterized by HPO_4^{2-} groups, such as octacalcium phosphate (OCP), or dibasic calcium phosphate dihydrate (DCPD).

Dissolution can be performed by macrophages and osteoclasts, analogously to bone remodelling, or by extracellular activity, namely lowering the local pH. The process rate, key factor in the reliability of the implant, is strongly influenced by multiple factors; partially they depend on the ceramic, as well as chemical formulation (Ca/P ratio, ionic substituents), initial porosity, crystallite size, defects and residual stresses; partially on the environment conditions (pH, temperature, fluid convention). In general, resorption is enhanced by higher contact areas between CaP and biological fluids, thereby small grains / particles and macroporosity (~100 μm of diameter) [23]. The resulting rate should be comparable to the new bone growing rate, which in turn depends on age, sex, and health status of the patient, varying from 3 to 36 months [24].

In summary, the properties for which CaPs is used in medical application, in addition to the already cited bioactivity and resorbability, are [25]:

- *osteoinductivity*: capability to induced bone healing or osteogenesis;
- *osteoconductivity*: or osseointegration [26], capability to forma a connective interphase with the living bone, preventing relative movements without any fibral tissue involvement;
- *mechanical stability*: capability to prevent mechanical failure, unless their brittle nature and the quite high level of porosity, resulting into low tensile and impact resistance. Because of that, CaPs are generally used as defect filler or coating on metallic grafts, avoiding as much as possible severe load-bearing conditions;
- *biostability*: capability to maintain their biological properties *in vivo*;
- *crystallinity*: amorphous fraction may cause too fast dissolution and cytotoxicity;

- *wettability*: or hydrophilicity, capability to attract water and proteins, enhancing the cell adhesion and differentiation.

1.1.4 CaP chemistry

The generic definition "Calcium phosphates" (CaPs) indicates the wide family of calcium salts derived by the neutralization of orthophosphate acid H_3PO_4 and its condensed forms. They can be considered effectively as ionic compounds, where Ca^{2+} ions are placed into the interstitials of a lattice formed by interconnected PO_4^{3-} tetrahedra. Phosphate group is the basic unit of CaPs; is characterized by a central phosphorous atom, with oxidation number equal to +5, capable to bond four oxygen atoms in a tetrahedral arrangement. The additional electron is used to create a π bond, stabilized by resonance, whereas the ion globally carries a formal charge of -3, distributed on the three single-bonded oxygens. As a consequence, phosphate groups are in equilibrium with three conjugated bases, according to [27]:

$$H_3PO_4 + H_2O \rightleftarrows H_2PO_4^- + H_3O^+ \qquad pK_{a1} = 2.2 \tag{2a}$$

$$H_2PO_4^- + H_2O \rightleftarrows HPO_4^{2-} + H_3O^+ \qquad pK_{a2} = 7.2 \tag{2b}$$

$$HPO_4^{2-} + H_2O \rightleftarrows PO_4^{3-} + H_3O^+ \qquad pK_{a3} = 12.0 \tag{2c}$$

Observing the equilibrium constant values, it can be noticed that all the four species are present in a phosphate aqueous solution, being their relative concentration dependent from the pH: completely deprotonated ion is predominant just in strong alkaline media. In addition, each species can form ionic salts with calcium. The compound multiplicity is further enlarged by the possible condensation between phosphate tetrahedra, following the simplified scheme:

$$-P-OH + HO-P- \rightarrow -P-O-P- + H_2O \tag{3}$$

According to the number of hydroxyl groups involved, the mechanism leads to the formation of linear, cyclic, or spatial polyphosphate; among them, the most relevant are pyrophosphate $P_2O_7^{4-}$, and metaphosphate PO_3^- ions.

After these considerations, the complexity of the calcium phosphate chemistry is quite evident. An easier approach to univocally identify a CaP compound consists of representing the species through the general formula C_xP_y, where:

$$(CaO)_x \cdot (P_2O_5)_y \cdot (H_2O)_z \tag{4}$$

and describing its stability field by a series of pseudo-binary equilibrium phase diagrams, based on the system $CaO\text{-}P_2O_5$ at different partial pressure of H_2O (Fig. I-2a and b).

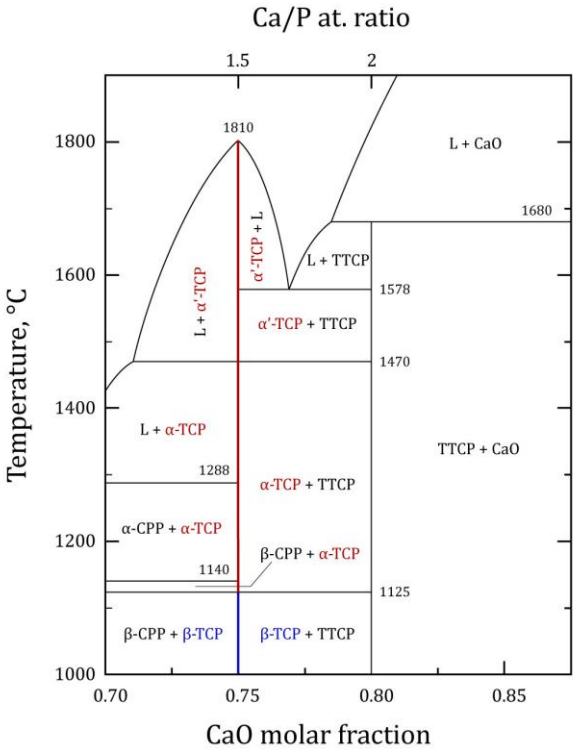

Figure I – 2a. Equilibrium phase diagram of the system $CaO\text{-}P_2O_5$ without presence of water. Colored vertical lines represent the stoichiometric compound β-TCP (blue), and α-TCP (red). Redrawn on the basis of [28] and [29].

The stoichiometric ratio between calcium and phosphorous atoms (Ca/P) hence becomes one of the most common parameter used in the field. Compounds with Ca/P ratio in the range 1.5-1.67 are usually called apatites, word created by the geologist Werner (1786) on the basis of the Greek terms *apatan* (~to deceive) since in nature this kind of mineral is often confused with others.

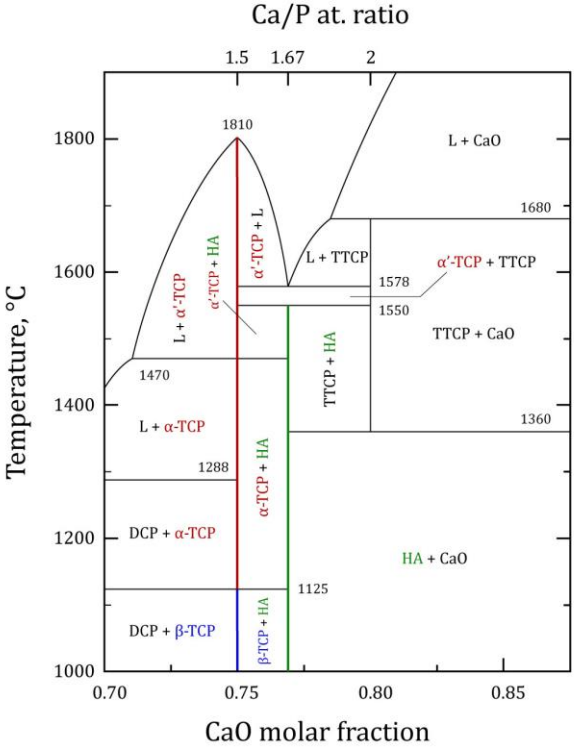

Figure I – 2b. Equilibrium phase diagram of the system $CaO-P_2O_5$ with 500 mm Hg of water partial pressure. Colored vertical lines represent the stoichiometric compound β-TCP (blue), α-TCP (red), and HA (green). Redrawn on the basis of [28] and [29].

For instance, considering the complete absence of water, the equilibrium phase diagram predicts the presence of tricalcium phosphate $Ca_3(PO_4)_2$ (TCP) at Ca/P ratio equal to 1.5. The stoichiometric compound is subjected to two consecutive phase

transitions: the first (1125°C) between β and α polymorphs; the second (1470°C) from α to α'. Melting point is reported around 1810°C, although small compositional deviations lead to eutectic points at 1288°C (Ca/P < 1.5) and 1578°C (Ca/P > 1.5) [29]. At the same time, biphasic regions of TCP with calcium pyrophosphate $Ca_2P_2O_7$ (CPP), and with tetracalcium phosphate $Ca_4(PO_4)_2O$ (TTCP) are present [28]. Conversely, in the presence of water, TCP side compounds are dicalcium phosphate $CaHPO_4$ (DCP) and, up to 1550°C, hydroxyapatite $Ca_{10}(PO_4)_6(OH)_2$ (HA); solidus line is unchanged.

In general, $CaO\text{-}P_2O_5$ equilibrium phase diagrams are a valid tool to produce, by a solid-state route or a wet-synthesis process, the desired CaP compound by mixing in the right amount calcium and phosphate source materials. Actually, the slow kinetic of some reactions has to be additionally considered, especially for what concerns reconstructive transformations, and the possibility of CaPs to accommodate slight stoichiometric imbalances as lattice defects, avoiding the formation of boundary phases.

1.1.5 TCP

Tricalcium phosphate $Ca_3(PO_4)_2$ (TCP) is the calcium salt of the third acidic dissociation of (ortho)phosphoric acid. TCP can be found in three main forms: β-TCP, occurring at low-temperature, up to 1125°C and the high-temperature stable phases α (up to 1470°C) and α' [30]. Among these, α'-TCP polymorph does not possess any biological interest, due to the restricted stability field and the spontaneous reconversion into α-TCP upon cooling [31]. Conversely, α-TCP can be retained at low temperature as metastable phase [32]. With respect to β form, it shows very different features, like monoclinic structure (space group $P2_1/a$, Z=24) [33], higher specific energy and, above all, higher resorption rate (0.0025 g L^{-1} at 25°C) [34], larger than bone growth. Therefore, biomedical applications in which α-TCP may be used are limited to CaP cements [35].

β-TCP presents a rhombohedral crystal structure (space group R3c, Z=21), related to whitlockite ($Ca_{18}Mg_2H_2(PO_4)_{14}$), a mineral phase found in dental calculi and urinary stones [36]. The unit cell is characterized by the parameters $a = b = 10.4352$ Å, $c = 37.4029$ Å and $\alpha = \beta = 90°$, $\gamma = 120°$, with a calculated volume of 3527 $Å^3$. Within the structure are recognizable two different type of columns, aligned along the c-axis, reciprocally organized according to a hexagonal coordination.

In details, the two columns are based on the recurring polyhedral sequences:

$$P(1)O_4 - Ca(4)O_3 - Ca(5)O_6 \tag{5a}$$

$$P(3)O_4 - Ca(1)O_7 - Ca(3)O_8 - Ca(2)O_8 - P(2)O_4 \tag{5b}$$

which show three not-equivalent phosphorous sites, and five not-equivalent calcium sites. The first sequence is the most relevant from a crystallographic point of view: being the total charge equal to +1, the electroneutrality of the crystal is ensured by a bivalent cationic vacancy every two polyhedral sequences. In other words, Ca(4) site exhibits an occupational factor of ~0.50. In addition, this plane-triangular interstice shows Ca-O bond length values higher than the sum of the respective ionic radii, revealing the underbonded nature of the metal ion. As a consequence, the presence of monovalent cations within the β-TCP lattice, as impurities or dopant agents, is accommodated by replacing Ca^{2+} into the Ca(4) position and filling up the vacancy [37].

Diametrically opposed is the behavior of Ca(5) site: the octahedral interstice exhibits Ca-O bond shorter than the ionic radii, and thus Ca^{2+} results overbonded. Introducing bivalent cationic substituents, above al Mg^{2+}, calcium is replaced in this site up to complete saturation.

β-TCP is considered either osteoinductive and osteoconductive; if placed in contact with the biological fluids, it can induce the precipitation of an apatitic layer which promotes bone growth. Its resorption rate (0.0005 g L^{-1} at 25°C) [34], makes TCP suitable for CaP bone cements, bone-substitution ceramics, and polishing agent in commercial toothpaste, as well [38]. It is also used as food additive (E341) [39].

The easier route to produce TCP consists in solid-state reaction at high temperature (~1000°C) between calcium and phosphate source materials, conveniently mixed according the stoichiometric Ca/P ratio of 1.5. More than one process is equally feasible, starting from calcium carbonate and ammonium phosphate, DCP anhydrous [36], or CPP [40]. The direct precipitation of TCP from aqueous solutions is not possible [21], since the first product occurring, according to the Ostwald step rule [41], is the so-called calcium deficient hydroxyapatite (CDHA), and therefore an additional heating treatments above 800°C is needed to crystallize TCP [42]. Alternatively, tricalcium phosphate can be precipitated in organic medium, such as methanol [43].

The β to α phase transition at ~1125°C constitutes the main technological issue encountered during the consolidation/densification of TCP components, especially upon high temperature process such as plasma spray coating [44]. As a matter of fact, the transformation is associated with an important volumetric expansion (7%) due to the different lattice volume and density of the two polymorphs, which introduces cracks and stops the shrinkage [45]. Moreover, the transition appears frequently irreversible upon cooling, leading to the presence of retained α phase at room temperature in the sintered TCP products, which changes the resorption rate of the material in the biological system.

This behavior was firstly studied by Monma et. al [46], demonstrating that β→α reaction is a reconstructive process following a first-order kinetic. A large activation energy of 250 kcal mol^{-1} was determined, due to the complex reorganization of the crystal structure, and inhibiting α→ β reconversion, at least for cooling rate higher than 10°C min^{-1}. Nevertheless, some authors have reported β phase in quenched α-TCP, as the result of a partial reconversion in spite of the rapid cooling treatment performed [47][48]. The phenomenon has been recently clarified by Carrodeguas et al. [49], stating that β-TCP presence after quenching can be only due to β-stabilizing impurities, or to the incomplete β→α transformation upon heating.

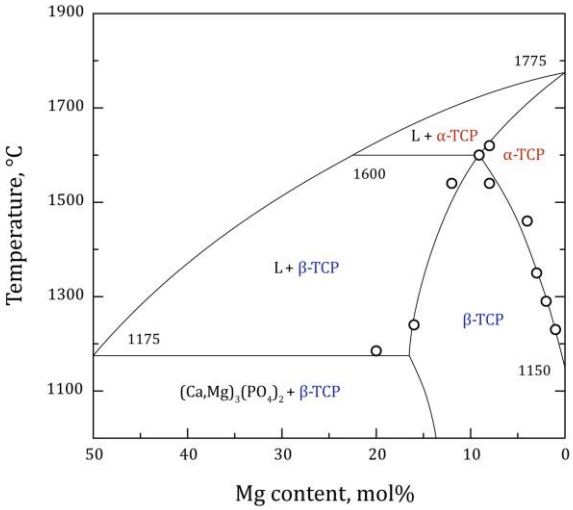

Figure I - 3. Equilibrium phase diagram of the system $Mg_3(PO_4)_2$-$Ca_3(PO_4)_5$. Redrawn on the basis of [50].

In details, calcium-substitutional ions such as K^+, Na^+, Ag^+, Mg^{2+}, Sr^{2+} and Zn^{2+} have been proposed in previous works [37][51][52][53][54][55] as possible solutions to increase β→α temperature and facilitate β-TCP sintering. Among then, magnesium seems to exhibits the most appreciable results [56], proportional to the amount of Ca^{2+} ions replaced by Mg^{2+}. An equilibrium phase diagram based on the system $Mg_3(PO_4)_2$-$Ca_3(PO_4)_2$ was proposed by Ando [57] and successively revised by Enderle et al. [50]. Maximum magnesium solubility occurs for 14 mol% of Mg^{2+}→Ca^{2+} substitution, corresponding to the completely occupation of both Ca(4) and Ca(5) sites; however, once Ca(5) interstice is saturated (9.1 mol% of Mg), β stability limit is maintained at 1600°C (Fig. I-3).

As previously reported, magnesium is naturally present in the mineralized fraction of the bone tissue. However, Mg doping biphasic HA/TCP formulation (9.5 mol% Mg) has been successfully tested *in vivo* [53] showing good biocompatibility

1.1.6 HA

Hydroxyapatite $Ca_{10}(PO_4)_6(OH)_2$ (HA) is characterized by Ca/P ratio of 1.67 and by the presence of hydroxyl group within the lattice. Although the great chemical affinity with the mineral fraction of bone tissue, HA is the lesser soluble salt (0.0003 g L^{-1} at 25°C) [34] among CaPs. Because of that, HA is generally considered osteoconductive, but not osteoinductive; anyway, ionic substituent like CO_3^{2-} lead to higher solubility and, as consequence, higher bioactivity. The clinical applications of hydroxyapatite regard repair of bone defects or fractures, ear prosthesis, dental surgery, drug delivery and, above all, coating on orthopedic / dental implants [7].

The crystal structure of HA is bi-pyramidal hexagonal, with space group $P6_3/m$ and cell parameters a = b = 9.418 Å, c = 6.884 Å, α = β = 90°, γ = 120°. At ¼ and ¾ of the c-axis, phosphate tetrahedrons are regularly placed on two basal planes [58]. Taking into account the HA unit cell, ten Ca^{2+} ions are placed within two non-equivalent interstices, six Ca(2) sites forming two staggered triangles, located above the phosphate basal plane, and four Ca(1) sites, aligned to the c-axis at the cell edges. Within the Ca(2) triangular channel, two OH- groups are placed aligned with the *c-axis*.

As well as for TCP, stoichiometric HA can be produced by solid state reactions between calcium and phosphate raw materials, properly mixed in the molar ratio 10:6. Additionally, wet-synthesis in aqueous media are equally feasible, as well as the

hydrolysis of other CaPs (DCP, TCP, CPP) at ~150°C, this allowing a better control on purity and grain size [59].

The thermal stability of hydroxyapatite strongly depends to the partial pressure of water vapor [60]. For instance, equilibrium phase diagram at P_{H2O} = 500 mm Hg [28] predicts at 1550°C the decomposition reaction of HA into α-TCP and TTCP:

$$Ca_{10}(PO_4)_6(OH)_2 \rightarrow 2\ \alpha\text{–}Ca_3(PO_4)_2 + Ca_4(PO_4)_2O + H_2O \quad (6)$$

Anyway, partial dehydration of HA could take place around 850-900°C, leading to the formation of the so-called oxyhydroxyapatite according to the reversible process [61]:

$$Ca_{10}(PO_4)_6(OH)_2 \rightarrow Ca_{10}(PO_4)_6(OH)_{2-2y} + y\ H_2O \quad (7)$$

Sintering of HA has been investigated by several authors and recently reviewed [62] by covering either conventional and assisted techniques, performed on wet-precipitated or commercial powders. For instance, nanometric HA powders can be fully-densified, without degradation or any secondary phases, by pressureless sintering in 1 hour (1100°C, 20°C min^{-1}) [63], by HP in 30 min (20 MPa, 1200°C, 15°C min^{-1}) [64], or by SPS in 1 min (50 MPa, 950°C, 100°C min^{-1}) [65].

1.1.7 ACP and CDHA

Amorphous calcium phosphates (ACPs) are a subcategory of CaPs where the atoms positions do not present long-range order. Basically, ACPs are the very first transient precursors of calcium phosphates synthesized by precipitation in aqueous media, due to their lower surface energy [66]. Their composition, in terms of Ca/P ratio, can vary between 1.18 and 2.5, according to the relative amounts of the reagents and to the solution pH [16]; in general, ACPs formation is promoted by higher concentration of Ca^{2+} and PO_4^{3-}, and strong alkaline environment. With the specific term ATCP the amorphous apatitic compound with Ca/P ratio equal to 1.50 is usually indicated, namely the precursor of tricalcium phosphates.

ACPs are used as component in CaP cements, dental or bone substitution applications, because of their ability to be solubilized at acidic pH and enhance the tissue remineralization. However, their resorption rate is very rapid [34], even more than α-TCP, and therefore local imbalances of pH and cytotoxicity may occur.

Despite the amorphous nature, a short-range order was detected in ATCP, corresponding to a spherical basic unit (~0.95 nm) called Posner's cluster [67], with composition $Ca_9(PO_4)_6$ and S_6 symmetry [68], the same of β-TCP. Such clusters can arrange into larger structure of ~20-300 nm under the effect of large amount of adsorbed water. Anyway, ACPs tend to spontaneously crystallized into CDHA [69], especially if the compound is maintained in its mother solution under moderate stirring, or temperature is increased. Most likely, Posner's clusters constitute the nuclei for CDHA crystal formation.

Calcium deficient hydroxyapatite (CDHA) can be expressed by the generical formula:

$$Ca_{10-x}(HPO_4)_x(PO_4)_{6-x}(OH)_{2-x} \quad \text{(1b)}$$

where $0<x<1$, and Ca/P ratio is given by (10-x)/6, thus varying between 1.5 (x = 1, TCP) and 1.67 (x = 0, HA). As a consequence, thermal treatments carried out at ~800°C induce its transformation into biphasic mixture of β-TCP and HA, according to the level rule.

CDHA is the synthetic compound which possesses the most similar composition to the mineralized bone tissue, thus is currently included in almost all the CaP cements commercially available [34]; its solubility is between which of β-TCP and HA, as expected. From a structural point of view, CDHA can be considered as stoichiometric HA lattice, but with point defects (atom vacancies) and more disorder, as easily observable in the related X-ray diffraction patterns.

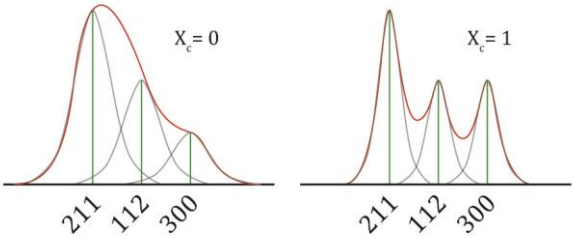

Figure I - 4. Schematic representation of the XRD main broad peak of CDHA, for X_c equal to zero (left) and equal to 1 (right).

With respect to stoichiometric and well-crystallized HA, CDHA spectrum shows a pronounced difference between the intensity of the 112 and 300 reflections (Fig. I-4). Therefore, Landi et. al. [70] defined the apatite crystallinity degree X_c as:

$$X_C = \left(1 - \frac{I_{112} - I_{300}}{I_{300}}\right)\% \tag{8}$$

where X_c ranges from zero (i.e. $I_{300} = I_{112}/2$), up to 100% (i.e. $I_{300} = I_{112}$) like in HA.

1.2 Sintering

1.2.1 Conventional sintering

As well as other ceramic materials, CaPs compounds are characterized by relatively strong chemical bonds, responsible for high melting points and brittle mechanical behavior. Thus, their production usually involves a thermal treatment at high temperature, lower than T_m, called sintering and performed on powder compact (i.e. the green body). The process leads to the gradual removal of the initial porosity and an increase of density associated to evident shrinkage and consolidation of the product in its almost-definitive shape.

From a thermodynamic point of view, sintering is an irreversible process, associated with a decrease in the Gibb's free energy of the system. Considering the absence of an external load, (i.e. pressureless sintering), the driving force of the process is the pressure gradient existing on the two side of a curved surface, according to the Laplace's law [71]:

$$\Delta P = \gamma\left(\frac{1}{r_1} + \frac{1}{r_2}\right) \tag{9}$$

where γ is the surface energy, and r_1 and r_2 the two principal curvatures of the considered surface. The model well describes a set of spherical granules (i.e. the raw powders) placed in contact upon the green body shaping. Therefore, either concave ($r<0$, i.e. interstices) and convex ($r>0$, particles) surfaces tend to assume a flat configuration ($r=\infty$) to eliminate the pressure gradient, by accepting and donating atoms, respectively. The mechanism can take place in reasonable time because of the limited distance to be covered by the atoms. Analogously, it can be demonstrated

that the atom vacancy concentration, with respect with a flat surface, is higher for negative curvature, and lower for positive curvature. Once again, atom migration from convex to concave surfaces is spontaneously induced in order to nullify the vacancy gradient.

Mass transport is governed by diffusional equations derived by the Fick's law, where the diffusional coefficient *D* accounts for the specific source, mechanisms and path followed by the atoms. In general, the process is thermally activated and, as consequence, promoted by higher temperature. Nevertheless, diffusion through the surface requires less energy than through grain boundaries (*GBs*), and further less than lattice; therefore, it is the first active mechanism in a sintering treatment, leading to neck formation between particles, but not to densification. In general, the kinetic of sintering can be described by two equations, respectively referred to the neck growth and the shrinkage / densification as a function of time *t* [72]:

$$\left(\frac{X}{r}\right)^m = \frac{H}{r^n} t \tag{10a}$$

$$\left(\frac{\Delta L}{L_0}\right)^{m/2} = -\frac{H}{2^m r^n} t \tag{10b}$$

where *X* and *r* are the semi-length and the curvature of the neck, *ΔL* the variation of the distance L_0 between two grain centers, *m* and *n* numerical exponents depending on the mechanism, and *H* a function containing geometrical parameters and the diffusional coefficient of the system.

The main stages of sintering can be described as:

- *initial stage*: concavities near the contact points of the granules are reduced by gradually forming interparticle necks and *GBs*. Since the material shrinkage is almost negligible, the stage is also indicated as pre-sintering.

- *intermediate stage*: pores have achieved an equilibrium shape but still constitute a continuous network; shrinkage and densification (~90%) occur by reducing the pore dimension and the distance between the grain centers.

- *final stage*: pores become isolated at the grain edges, shrinking up to completely disappear. The microstructural evolution is additionally characterized by grain growth or coarsening.

For the specific case of pressureless sintering of CaP apatites $Ca_{10-x}(HPO_4)_x(PO_4)_{6-x}(OH)_{2-x}$, neck formation was investigated as a function of the partial pressure of water in the system, and otherwise expressed as the variation of surface area *S* over time by the empirical relation [73]:

$$\frac{dS}{dt} = k(T, Ca/P)\ {P_{H_2O}}^{0.68}\ S^8 \tag{11}$$

where *k* is a kinetic coefficient depending on the process temperature and the chemical composition of the compound, namely related to the activation energy of the surface diffusion (~120 kJ mol^{-1}). Water vapor seems to catalyze the first stage of apatite sintering. Interestingly, kinetic coefficients determined at 700°C are equal to $9.2 \cdot 10^{-3}$ for Ca/P = 1.67 (stoichiometric HA), and 1.35 for Ca/P = 1.535 (CDHA precursor of β-TCP). In other words, surface reduction rate becomes almost 100 times larger by decreasing the Ca/P ratio, most likely due to an increment of Ca^{2+} and OH^- vacancies in the apatite lattice, which promote the mass transport through surface paths.

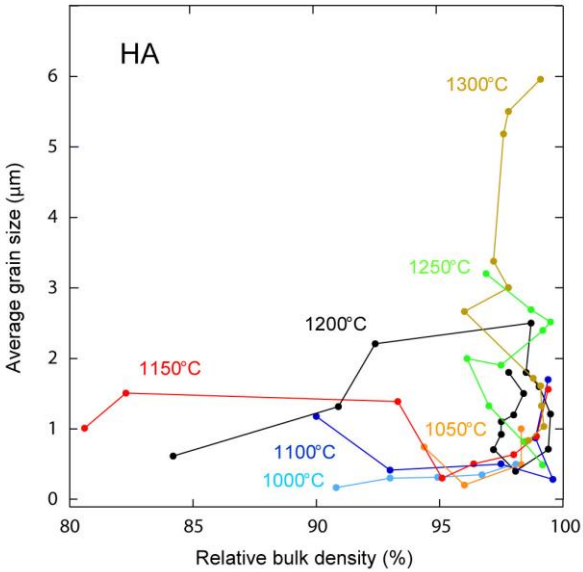

Figure I – 5a. Sintering trajectories of HA reproduced on the basis of [62]. Data collected by various authors: colored lines join data points related to the same sintering temperature.

As a direct consequence, grain growth and coalescence start before densification, significantly reducing the driving force for sintering at higher temperature. This phenomenon can account for decreasing the apatite sinterability with Ca/P ratio, as observed in literature [62]. One possible solution consists into the application of high heating rates up to ~800°C, in order to kinetically inhibit the surface reduction, or even to decompose CDHA into β-TCP / HA mixture, finely grind the product and restart a new sintering process.

Successively, starting from ~750°C, volume and grain boundary diffusions are both activated (~440 kJ mol^{-1}), leading to a progressive separation and closure of the porosity, which up to this moment was still interconnected and predominant [70]. Once again, curved grain boundaries achieve a thermodynamically stable flat configuration, with an equilibrium angle of ~120° and a coordination of 6, i.e. ideally hexagonal grains. The pinning action on the GBs mobility, previously carried out by the several pores present, is drastically reduced, and thus grain growth can occur according to:

$$\ln D = \ln Kt - \frac{Q}{RT} \tag{12}$$

where *D* is the average grain size, *K* a pre-exponential coefficient, *t* the time, *T* the temperature, *R* the gas constant. The activation energy of the process (*Q*) for stoichiometric HA, results in the range 200-240 kJ mol-1, under the simplified hypotheses of negligible initial grain size (G_0) and a kinetic exponential factor *n* equal to 1 [74].

Sintering of β-TCP has been much less investigated in the literature than HA. Although the sintering behavior of these two CaPs is quite similar, it has to be recalled that sinterability decreases with the Ca/P ratio, and also β→α-TCP phase transition around 1150°C, extensively discussed above, limits the maximum process temperature. Moreover, small quantities of $Ca_2P_2O_7$ (*CPP*) impurities strongly reduce β-TCP densification, inducing abnormal grain growth [75]. Interestingly, mixtures of β-TCP / HA, indicated as biphasic calcium phosphates (*BCPs*), seem to exhibit lower sinterability than pure-single phases [76]. Because of such difficulties, β-TCP compounds are frequently consolidated by non-conventional techniques, such as hot-pressing (*HP*) [77], spark plasma sintering (*SPS*) [78] or plasma spray [44].

Sintering trajectories of HA and TCP compounds are reported in Fig. I-5a and b, on the basis of a review paper [62]. In particular, just few cases of fully-dense β-TCP polymorphs (T<1150°C) are reported, starting from nanosized powders and performing pressureless or *HP* sintering.

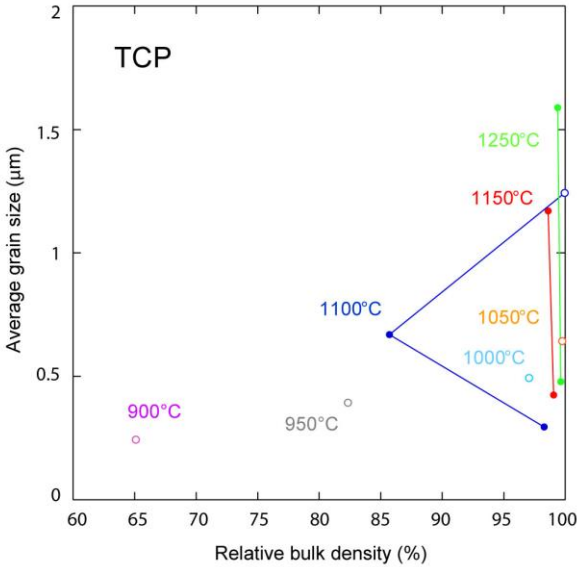

Figure I – 5b. Sintering trajectories of TCP reproduced on the basis of [62]. Data collected by various authors: colored lines join data points related to the same sintering temperature. Empty points are referred to *HP* processes.

1.2.2 Flash Sintering

Flash sintering is an electrical field-assisted sintering (*EFAS*) technique recently proposed in order to consolidate ceramic green bodies at relatively low temperature and in short times. With respect to spark plasma sintering (*SPS*) (a field-assisted process which requires conductive dies and the application of high pressure [79]), flash sintering (*FS*) involves direct Joule heating of samples and much simpler equipment. At the same time, the extremely rapid heating rate (~100 °C min^{-1}) simplifies the consolidation of meta-stable phases or non-oxide ceramics, inhibiting the grain growth and ensuring optimal final properties at the material (mechanical strength, transparency, …).

Flash sintering technique was first proposed and investigated in 2010 by Cologna et al. [80], working on tetragonal 3YSZ nanopowders and achieving almost

instantaneous densification of the material at 850°C, with the application of 120 V cm^{-1}. Successively, the complete definition of FS was reported by Raj et al. in a US patent application [81] as follows:

"A method of sintering a material comprising simultaneously exposing the material to an electric field and to heat, such that the material is sintered, wherein the electrical field is between 7.5 V/cm and 1000 V/cm, wherein the onset of sintering is accompanied by a power dissipation between 10 to 1000 mW mm^{-3}, wherein the onset of sintering is accompanied by a non-linear increase in the conductivity of the material, and wherein the time between the onset of sintering and the completion of sintering is less than one minute"

Such definition entails the electrical behavior of the considered material being described by a negative temperature coefficient (*NTC*) of resistivity, namely the main characteristic to enhance their conductivity (by migration of electrons, holes, ions, or defects) by increasing the temperature [82]. Moreover, the concept of flash event is introduced through the sintering onset, usually identified by the furnace temperature at which it occurs (T_{on}), and related with power and conductivity surges.

Interestingly, very different ceramic materials have been tested under FS condition in the last few years, always showing the common phenomenology descripted above:

- insulators: Al_2O_3 [83][84], $BaTiO_3$ [85], $KNbO_3$ [86], $SrTiO_3$ [87];
- semi-conductors: TiO_2 [88][89], ZnO [90], SiC [91], B_4C [92], SnO_2 [93];
- oxygen ion conductors: 3YSZ [94], 8YSZ [95][96], GDC [97][98];
- metal-like conductors: Co_2MnO_4 [99], $MoSi_2$ [100], ZrB_2 [101];

The basic FS experimental equipment is quite easy and consists of a conventional furnace, two conductive electrodes (usually Pt alloy), a power supply (*DC* or *AC*) and a multimeter. Treatments can be additionally performed within a dilatometer in order to detect sample shrinkage, as well as CCD camera, UV/VIS spectrometer [102], or even X-ray diffractometer [88] can be accessorized to study the FS material behavior from different point of view. Also the specimen shape plays an important role in the overall process, affecting the geometry and the connection with the electrodes. The very first FS experiment [80] was carried out on dogbone-like samples with rectangular cross-section, where the electrodes were composed of Pt wires, inserted within two holes at the sample extremities. In spite of the peculiar geometry, such configuration remains the most adopted in literature, ensuring an

optimal connection with the power source, and regular field-lines in the central portion of the specimens. Other options consist into rectangular bars, with electrode wires coiled around the sample extremities, or cylindrical pellets coupled with plate electrodes.

Flash sintering tests can be divided into two categories according to the thermal program adopted during the application of the electric field, namely constant heating rate (isochronal) or constant temperature (isothermal).

In both the cases, three main stages are identifiable:

- *stage I* or incubation; the system works in voltage control;
- *stage II* or flash event;
- *stage III*; the system works in current control.

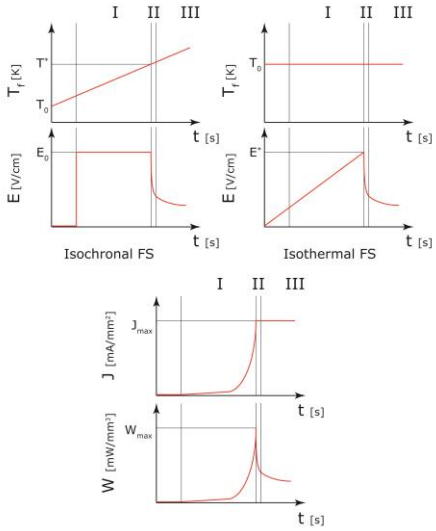

Figure I - 6. Schematic representation of the typical behavior of a ceramic material subjected to FS process: isochronal mode (left) and isothermal mode (right).

In a typical isochronal experiment (Fig. I-6), constant heating rate and constant electric field *E* are applicated to the material. Due to its high resistivity at low temperature, the current flowing through the sample is initially almost neglectable (stage I). Then, recalling the *NTC* condition, the increment in the furnace temperature leads to a gradual growth of the current, additional source of heat by Joule effect, and at the end, to an abrupt surge of both current and dissipated power (stage II). Starting from this instant, rapid shrinkage affects the material. In order to avoid system damages, the maximum current J_{max} is limited to a preset value, and thus the treatment proceeds by maintaining a constant current (stage III) for a variable time. Very similarly, in an isothermal FS experiment, sample is maintained at a constant temperature, while the electric field is gradually increased (stage I). Once a critical value is reached, the current resulting from the combination of *E* and *T* rapidly arises up to the limit (stage II and III), causing material densification.

After several works reported in literature, it is quite commonly accepted that the physical condition leading to the flash event in a ceramic material, conventionally heated and simultaneously crossed by current, is a positive combination of *NTC* of resistance and Joule effect, known as thermal runaway mechanism [103][104]. However, the explanation about the successive extremely fast densification of the material is still under discussion: some studies seem to prove the completely thermal nature of the process [105], whereas others hypothesize alternative mechanism based on Frenkel pairs nucleation [88][94], supported by the observation of luminescence phenomena. The key factor in the understanding of flash sintering is undoubtedly the exact determination of the real sample temperature (T_S) during the process, made difficult by the limited time window of the event. Moreover, the inner current flow causes a sensible temperature gradient between the specimen skin and core, and thus direct measurements realized by pyrometer tend to underestimate the actual sample temperature. The most common route consists into the application of physical [106] or mathematical [107] models in order to estimate T_S by a thermal balance of the system, and consequently to compare such previsions with experimental evidence.

The only reference in literature of CaP flash sintering, is the recent work of Bajpai [108] regarding the achievement of almost fully-dense HA (dogbone specimens) in isochronal and *DC* conditions, at 1024°C and 1000 V cm^{-1}.

Aim of the work

Calcium phosphate bioceramics, especially hydroxyapatite and tricalcium phosphate, have been intensively studied in the last years because of their excellent biocompatibility, osteoinductivity, and bio-resorbability properties, which make them ideal candidates for bone regenerative medicine. Nevertheless, both chemistry and thermal behavior of calcium phosphates are still object of discussion in literature. For instance, sinterability of β-TCP is strongly affected by the phase transition into the α polymorph, which limits the biological and mechanical properties of the final sintered materials.

The aim of the present work was to investigate the influence of magnesium as dopant of TCP, synthetized by two alternative different routes, on physical and structural properties and to produce dense β-TCP samples by using an innovative electrical field-assisted technique known as flash sintering. In addition, strontium substituted hydroxyapatite nanopowders were also synthesized and characterized, as possible drug release vectors.

Chapter II

Materials and Methods

2.1 Solid state reaction: Magnesium doping β-TCP

Beta - Tricalcium phosphate powders were synthesized by solid-state reaction with different amount of Mg^{2+} doping ions. High purity raw materials, calcium carbonate ($CaCO_3$, >99.95 wt%, Sigma-Aldrich), ammonium phosphate dibasic ($(NH_4)_2HPO_4$, >99.0 wt%, Fluka) and magnesium oxide (MgO, 98.8 wt%, Farve) were mixed to obtain 0, 1, and 2 mol% Mg^{2+} containing TCP; the corresponding samples were labelled as Mg0, Mg1 and Mg2 (Mg-TCP series).

The high purity starting materials were weighted in stoichiometric quantity to obtain (Ca+Mg)/P molar ratio equal to 1.50; the mix was then homogenized in a ZrO_2 ball mixer with ethanol and dried at 80°C. The dried powders were placed into an alumina crucible and solid-state reaction was performed at 1000°C for 30 h (heating rate 10°C min^{-1}, free cooling).

According to previous works [109], the expected reaction is:

$$(3-x)\ CaCO_3 + 2\ (NH_4)_2HPO_4 + x\ MgO \rightarrow Ca_{3-x}Mg_x(PO_4)_2 + (3-x)\ CO_2 + 3\ H_2O + 4\ NH_3 \quad (13)$$

where the amount (mol%) of dopant can be expressed as Mg/(Ca+Mg)·100 = *x*/0.03.

2.2 Precipitation method: Magnesium doping β-TCP

Calcium phosphate nanopowders (Ca/P ratio = 1.5) were synthesized by chemical precipitation via aqueous media in two different compositions, without any doping ions (nMg0) and with 5 mol% magnesium (nMg5) substituting calcium (nMg-TCP series). The n prefix was added to distinguish these nanometric-size compositions from the equivalent micrometric powders obtained via solid-state reaction and above described.

Hence, nitrate solutions (50 ml, 0.6 M) were prepared starting from calcium nitrate tetrahydrate $Ca(NO_3)_2 \cdot 4H_2O$ (Sigma Aldrich, powder >99.0%) and, for the

doped composition, magnesium nitrate hexahydrate $Mg(NO_3)_2 \cdot 6H_2O$ (Fluka, powder 99%) as well. For the phosphate solutions (50 ml, 0.4 M), ammonium phosphate dibasic $(NH_4)_2HPO_4$ (Fluka, powder >99.0%) and ammonium hydroxide NH_4OH (Carlo Erba, 30 vol%) were equimolarly mixed to obtain a buffer at pH ~9. The syntheses were carried out by rapidly adding the nitrate solution to the phosphate buffer, under vigorous stirring at room temperature, according to the reaction:

$$(9-3x)\ Ca(NO_3)_2 \cdot 4H_2O + 3x\ Mg(NO_3)_2 \cdot 6H_2O + 6\ (NH_4)_2HPO_4 + 6\ NH_4OH \rightarrow Ca_{9-3x}Mg_{3x}(HPO_4)(PO_4)_5OH + 18\ NH_4NO_3 + (41+6x)\ H_2O \quad (14)$$

where the molar amount (mol%) of Mg^{2+} replacing Ca^{2+} can be expressed as Mg/(Mg+Ca)·100 = 100*x*/3 [110]. After 2 hours of aging, the resulting suspensions were repeatedly washed with distilled water, centrifugated (7000 rpm), and finally dried at 80°C overnight.

2.3 Precipitation method: Strontium doping HA

In a very similar way, HA nanopowders were synthesized by aqueous precipitation method with different Sr^{2+} contents, following the procedure described by Bigi et al. [111]. High-purity calcium nitrate tetrahydrate ($Ca(NO_3)_2 \cdot 4H_2O$, 99 wt%, Sigma Aldrich A.C.S. reagent), and strontium nitrate anhydrous ($Sr(NO_3)_2$, 98%w, Alfa Aesar) were used to prepare the Ca+Sr nitrate solutions (50mL, 1.08 M overall); whereas ammonium phosphate dibasic ($(NH_4)_2HPO_4$, >99.0 wt%, Fluka) and ammonium hydroxide NH_4OH (Carlo Erba, 30 vol%) were once again mixed to obtain the phosphate buffer at pH ~10 (50 mL, 0.65 M).

In order to avoid carbonatation, the syntheses were carried out in N_2 constant flow, adding the phosphate solution to the nitrate solution at 90 °C under vigorous stirring. The solutions were additionally stirred at 90 °C in N_2 static atmosphere for 5 h; then, the white precipitates were repeatedly centrifuged (7000 rpm for 10 min), washed and finally dried at 80 °C overnight. The expected reaction was:

$$(10-y)\ Ca(NO_3)_2 \cdot 4H_2O + y\ Sr(NO_3)_2 + 6\ (NH_4)_2HPO_4 + 8\ NH_4OH \rightarrow Ca_{10-y}Sr_y(PO_4)_6(OH)_2 + 20\ NH_4NO_3 + (46-4y)\ H_2O \quad (15)$$

Strontium content in the final HA powder was tailored changing the relative amount of $Ca(NO_3)_2 \cdot 4H_2O$ and $Sr(NO_3)_2$ in the nitrate solutions, to obtain Sr/(Sr + Ca)

ratio of 0, 5, 10, 25, 50, 75 and 100 mol%; nanopowders were labelled as nSrX, where X= Sr mol% = 10*y* (nSr-HA series).

2.4 Powder characterization

2.4.1 ICP-OES
Inductively Coupled Plasma - Optical Emission Spectrometry

Purity and real doping content of powders (Mg-TCP, nMg-TCP and nSr-HA) were initially checked by ICP-OES (Spectro Ciros Vision CCD, 125–770 nm) using hydroxyapatite ultrapure standard (>99.995% trace metal basis, Sigma–Aldrich), a multi-element standard (Merck KGaA, type IV) and a specific Sr standard (1000 ppm, BHD SpectroSol). The samples were solubilized in ultrapure nitric acid (70 vol%) and diluted with pure water (reverse osmosis, $\sigma < 0.1$ µS cm^{-1}), adding standards and Cs (100 g/L) as ionization suppressor. The emission lines chosen for the analysis were 184 and 393 nm for Ca, 178 nm for P, 279 nm for Mg, and 217 nm for Sr.

2.4.2 XRD
X-Ray Diffraction

Two different diffractometers were used to analyze the synthesized powders and the related sintered samples, taking advantage of the peculiar features of each instrument. Then, the spectra were analyzed by the Rietveld-base software Maud (ver. 2.55) [112].

The first diffractometer is Rigaku DMAX III 4057A2, based on Bragg-Brentano configuration, working with Cu Kα as source radiation (8.08 keV) at 40 kV / 30 mA. Data were collected within the 2Theta range 10°–60°, with an angular resolution of 0.03° and an acquisition time of 10 s/step. Due to the extreme precision of the source / detector movements, this device is the best option for the peak position determination and, consequently, it was used to measure the cell parameters and the crystallite sizes of the phases detected. Instrumental broadening was taken into account by using Si powder standard (SRM 640b – NIST) for calibration.

Conversely, a Debye–Scherrer diffractometer (Italstrutture CPS) equipped with curved detector and working at the same operating conditions (Cu Kα 8.08 keV, 40 kV / 30 mA), allows to obtain higher signal/noise ratio with only 10 min acquisition time; it was therefore used for the quantitative analysis of the samples.

JCPDS cards chosen for the spectra refinement are summarized in Tab. II-1, with the corresponding densities ρ_{cry} (crystallographic) and ρ_{th} (measured). Under these conditions, the detection limit *DL* of the instrument can be estimated equal to 1 wt% for a single crystalline phase.

Phase	*Name*	*JCPDS #*	ρ_{cry}, g cm^{-3}	ρ_{th}, g cm^{-3}
β-TCP	β Tricalcium Phosphate	09-0169	3.12	3.07
α-TCP	α Tricalcium Phosphate	29-0359	2.81	2.86
HA	Hydroxyapatite	09-0432	3.08	3.14
SrHA	Strontiumapatite	33-1348	3.84	3.95

Table II - 1. JCPDS cards used for the refinement by Maud software, and density values of the related crystalline phases.

2.4.3 FT-IR
Fourier Transform – Infrared Spectroscopy

FTIR spectra were acquired in the range of 4000–400 cm^{-1} (resolution=4 cm^{-1}, 64 scans) using an Avatar Thermo FTIR spectrometer. For the tests, sample powders were manually mixed in mortar with anhydrous KBr, uniaxially pressed in thin circular pellets, and analyzed in transmission mode.

2.4.4 SS-NMR
Solid State Nuclear Magnetic Resonance

Solid state NMR analysis on ^{31}P and ^{1}H nuclei was performed using a Bruker 300WB instrument (nSr-HA series). Sample powders were compacted within ZrO_2 rotors (d = 4 mm), and placed in rotation under Magic Angle Spinning (MAS) at 11 kHz by flowing air.

^{31}P-MAS experiments were recorded at 121.49 MHz, both under proton-decoupling (^{31}P SP) and under cross-polarization (^{31}P CP) configuration, using ammonium dihydrogen phosphate $NH_4H_2PO_4$ as secondary reference. ^{31}P SP tests consisted in a single pulse (π/2) of 3.6 μs, followed by a recycle delay of 300 s. High-

power proton decoupling were used during the entire signal acquisition (16 scan). ^{31}P CP tests have been recorded with a contact time of 0.5 ms (100 scans).

Conversely, ^{1}H-MAS experiments were carried out at 300.13 MHz, π/2 pulse of 5 μs, and 5 s of recycle delay (16 scans), using pure ethanol as secondary reference.

2.4.5 Nitrogen sorption

N_2 physisorption analyses were carried out on a Micromeritics ASAP 2010 analyzer on the nanometric-size powders (nMg-TCP and nSr-HA series). Specific surface area (SSA) and pore volume distributions were calculated from N_2 adsorption/desorption isotherms applying BET equation and BJH model, respectively. SSA values were also used to estimate the average particle dimensions *D*, by the well know relationship:

$$D = \frac{\Psi}{\rho_{th}\, SSA} \tag{16}$$

where ρ_{th} is the theoretical density of the considered material (see Tab 3) and ψ a particle shape factor.

2.4.6 TEM
Transmission Electron Microscopy

Nanopowder size and morphology (nMg-TCP and nSr-HA series) were investigated by Zeiss EM10 TEM operating at 80 kV. Powders were dissolved in acetone and sonicated for 10 min; then the resulting suspensions were deposited on the copper grids, allowing solvent evaporation overnight.

2.4.7 TG-DTA
Thermogravimetric – Differential Thermal Analysis

The thermal behavior of the synthesized powders was studied by a Netzsch Gerätebau STA409/DAS 414 system, using calcined alumina as reference. Experiments were carried out in static air with different constant heating rate (v = 2, 5, 10, 20, 40 °C min^{-1}), up to 1200°C.

Following an isochronal approach, indeed, it is possible to graphically determine the activation energy Q (J mol^{-1}) of a detected thermal event from the Kissinger equation [6]:

$$\ln\frac{T_*^2}{v} = \frac{Q}{R}\frac{1}{T_*} + const \tag{17}$$

where T_* represents the peak temperature (K) measured at the different heating rate v, and R the gas constant (8.31 J K^{-1}mol^{-1}).

2.5 Thermal treatments

2.5.1 Conventional sintering

The sintering behavior of Mg-TCP series was initially studied by dilatometric analysis, shaping the powders into circular pellets (thickness ~3 mm, diameter 12 mm) by uniaxial pressing (for 5 min at 5 t). Horizontal-loading dilatometer (Linseis L75 Platinum Series) with Al_2O_3 ram and boat was employed and tests were performed with heating rate of 20°C min^{-1} up to 1550°C. Similarly, isothermal sintering was investigated on Mg0 composition, with heating rate of 40°C min^{-1} up to 900°C or 1100°C and 2 h holding time.

In addition, the same type of green pellets was sintered in air atmosphere at 1400°C (heating rate 10°C min^{-1}, 2 hours holding time), and then alternatively subjected to two different cooling processes: a controlled cooling at -10°C/min inside the furnace (C series), and a quickly air-quenching outside the furnace (Q series).

Similarly, nMg-TCP nanopowders were shaped into circular pellets (thickness ~3 mm, diameter 6 mm) by uniaxial pressing (for 5 min at 5 t). Dilatometry were carried out at 20°C min^{-1} up to 1200°C, and sintering treatments at 10°C min^{-1}, up to 1000 °C.

2.5.2 Annealing

The possible reconversion of the retained α-TCP phase into β-TCP was investigated by performing an annealing treatment on previously sintered and quenched Mg-TCP samples (QA series). Two different approaches were adopted: constant heating rate (2 °C min^{-1}) within the dilatometer (quartz boat and ram) and isothermal treatments at

700, 730, and 775 °C for 1, 2, 3, and 10 h (Mg1 composition, only). The latter samples, after the quantification of β-phase by XRD (w_β, weight fraction), were used to investigate the kinetic of α→β reconversion according to the Avrami equation:

$$f(t) = w_\beta = 1 - e^{-kt^n} \tag{18a}$$

where *n* is the Avrami parameter, depending on the transformation mechanisms, and *k* the kinetic factor, depending on the temperature according to the Arrhenius law:

$$k(T) = k_0\, e^{-Q/RT} \tag{19a}$$

where k_0 is the pre-exponential coefficient, *Q* the activation energy of the transformation and *R* the gas constant. Both equations can be linearized to determine *n*, *k* and *Q*:

$$\ln\big(-\ln\big(1 - w_\beta\big)\big) = \ln k + n \ln t \tag{18b}$$

$$\ln k = \ln k_0 - \frac{Q}{R}\frac{1}{T} \tag{19b}$$

2.5.3 Isochronal Flash Sintering

Flash sintering experiments were performed on tricalcium phosphate powders (TCP and nMg-TCP) within the dilatometer above descripted. Cylindrical green pellets (d = 8 mm, height = 2–5 mm) were shaped by uniaxial pressing the powder at ∼70 MPa, and then placed into the instrument between two Pt-Rh flat electrodes following the scheme in Fig. II-1. The electrical field was generated by a DC power supply (EW5R120, Glassman High Voltage Inc.); additionally, silver paste was applied on the sample surface to improve the electrical connection with the electrodes. Voltage and current were constantly detected by a multimeter (Keithley 2100, 1 Hz), while linear shrinkage and furnace temperature were simultaneously measured by the dilatometer.

For all experiments, constant heating rate of 20 °C min^{-1} and current limit J_{max} of 2 mA mm^{-2} (i.e. 100 mA) were adopted, whereas different E fields (range 500-2000 V cm^{-1}) were applied and maintained constant since the dilatometer furnace reached 500°C.

Once the flash event occurred and the system was switched to current control (stage III), the sample was kept in this condition for a variable time.

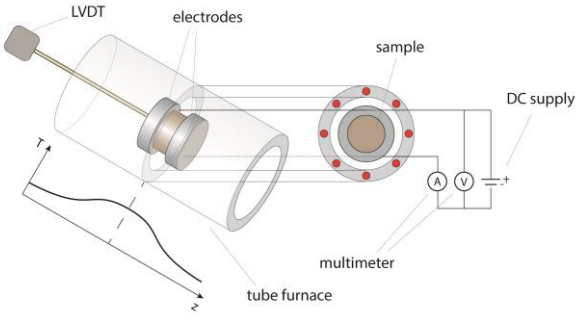

Figure II - 1. Schematic representation of the experimental setup used for the isochronal flash sintering tests.

2.5.4 Isothermal Flash Sintering

Some flash experiments were also performed in isothermal condition on dog-bone-shaped specimens (see Fig II-2), limiting the maximum current flow at 7.5 mA mm^{-2}. For this purpose, the synthesized nanopowders (nMg0 composition, only) were uniaxially pressed at ~150 MPa, obtaining samples with a rectangular central section of (1.5 x 3.1 x 12.0) mm, and pre-sintered at 800°C for 30 min.

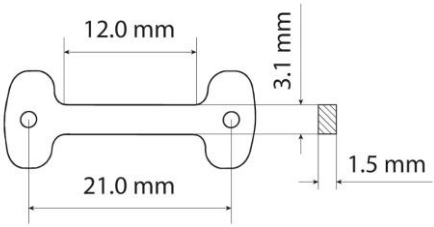

Figure II - 2. Dogbone-like sample used for the isothermal flash sintering tests.

Two through-holes allowed to insert directly the Pt wires and connect the specimen to the electrical circuit described above; no conductive paste was applied.

Then, flash sintering treatments were carried out within a horizontal tubular furnace (Nabertherm P330) pre-heated and maintained at 900°C (Fig. II-3), whereas E field was gradually increased up to 750 V cm^{-1}.

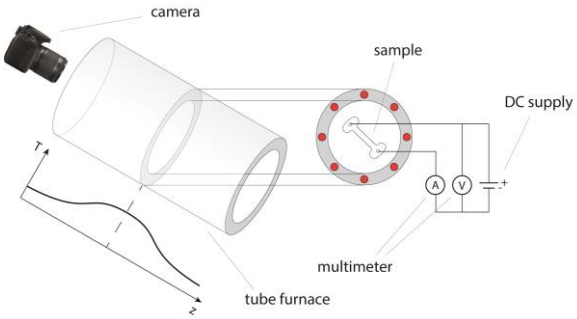

Figure II - 3. Schematic representation of the experimental setup used for the isothermal flash sintering tests.

2.6 Sintered body characterization

2.6.1 SEM
Scanning Electron Microscopy

The microstructure of sintered specimens, as well as the morphology of the synthesized powders and the dimension of the hardness indentations were determined by Jeol JSM 5500 scanning electron microscope (SEM).

2.6.2 Density – Archimede's method

In agreement with ASTM C830-00 standard, open porosity P_{open} (vol%) and densification ρ/ρ_{th} (%) of the sintered samples were determined by the Archimedes' method using an analytical balance (Gibertini E42S, ± 0.1 mg) according to the equations:

$$P_{open} = 100\,\frac{W - D}{W - S} \tag{20}$$

$$\rho/\rho_{th} = \frac{100}{\rho_{th}} \frac{D}{W-S} \tag{21}$$

where D, S, and W represent dry, suspended, and saturated weight, and ρ_{th} the theoretical density of the material (see Tab II-1). In case of a multi-phase specimen, the overall density can be estimated as:

$$\frac{1}{\rho_{th}} = \sum \frac{w_i}{\rho_i} \tag{22}$$

where w_i and ρ_i represent the weight fraction (by XRD refinement) and the density of the *i*-th phase, respectively.

2.6.3 Vickers Hardness

The sintered Mg-TCP samples subjected to controlled cooling (C series) and air-quenching (Q series) were molded in epoxy resin, polished with SiC papers (180 to 1200 grit), and finished with 6 μm diamond abrasive. Then, the specimens (3 for each composition) were subjected to Vickers indentation, using an indenter set up to achieve the applied load (equal to 5 kg) in 30 s, with 5 s holding time. The indentations performed were observed and measured by SEM up to collect at least 3 acceptable data for each different sample (i.e. 9 values for each composition). Vickers hardness was calculated as:

$$HV = \frac{1.8544\ F}{d^2} \tag{23}$$

where *F* is the indentation load and $d = (d_1+d_2)/2$, representing the average value between the two-measured diagonal length of a single indentation.

2.6.4 Mechanical Strength – Piston-on-three-ball test

The mechanical characterization of Mg-TCP series was integrated by biaxial flexure test (piston-on-3-ball load scheme) carried out on circular pellets (thickness ~3 mm, diameter ~20 mm, 5 for each composition). The samples were shaped by cold-pressing the powders at the same previously reported conditions (5 min at 5 t), sintering and cooling processes being maintained similar to those for C and Q series

described above. According to ISO 6872 standard, the maximum tensile stress σ_{max} (MPa) for a specimen subject to this load configuration can be calculated as [113]:

$$\sigma_{max} = \frac{-0.2837P(X-Y)}{t^2} \tag{24a}$$

$$X = (1+\nu)\ln\left(\frac{c^2}{R^2}\right) + \left(\frac{1-\nu}{2}\right)\left(\frac{c^2}{R^2}\right) \tag{24b}$$

$$Y = (1+\nu)\left[1+\ln\left(\frac{a^2}{R^2}\right)\right] + (1-\nu)\left(\frac{a^2}{R^2}\right) \tag{24c}$$

where *P* is the failure load, v the Poisson ratio (assumed equal to 0.27), *a* the radius of the circle passing through the 3 balls center (6.29 mm), *c* the piston radius (0.98 mm), *R* and *t* the radius (mm) and the thickness (mm) of the disk specimen, respectively. Tests were performed at 0.025 mm s^{-1} (i.e. displacement control) with an Universal Testing Machine (MTS - MPS 810).

2.7 Thermal modelling of FS

As already discussed in the Introduction, the real temperature of a material subjected to FS conditions is a crucial step to understand the phenomenon and to identify the technical parameters necessary to induce the process.

A green body of mass *m* and specific heat C_p is considered; the following thermal balance can be introduced:

$$mC_p\frac{dT}{dt} = W_{in} - W_{out} \tag{25}$$

More specifically, the positive power contribution W_{in} is due to Joule heating effect:

$$W_{in} = VI = RI^2 = V^2/R \tag{26}$$

where V is the voltage, I the current, and R the resistance, according to the first Ohm's law. Conversely, the term W_{out} is due to the temperature differences between specimen (T_s) and furnace (T_f), causing a negative thermal flux from the material by radiation (~ΔT^4) and through the two electrodes (~ΔT):

$$W_{out} = \sigma_{SB}\varepsilon S_{rad}\left(T_s^4 - T_f^4\right) + 2h_{cont}S_{cont}\left(T_s - T_f\right) \tag{27}$$

where σ_{SB} is the Stefan-Boltzmann constant, ε the optical emissivity, h_{cont} the contact conduction coefficient, S_{rad} and S_{cont} the specimen surfaces involved in the specific thermal exchange mechanism. More in detail, the second term describes the heat losses through the imperfect interface between specimen and electrodes, characterized by mixed conduction mechanism through the contact points, and convection through the cavity / open porosity [114]. The present model assumes a uniform temperature T_s throughout the specimen.

The overall balance can be therefore written as:

$$mC_p\frac{dT_s}{dt} = VI - \sigma_{SB}\varepsilon S_{rad}\left(T_s^4 - T_f^4\right) - 2h_{cont}S_{cont}\left(T_s - T_f\right) \tag{28}$$

Finally, the evolution of the sample temperature between two consecutive instants t_i and t_{i+1} can be expressed by:

$$T_{s\,i+1} = T_{s\,i} + \frac{t_{i+1} - t_i}{mC_p}\left[V_i I_i - \sigma_{SB}\varepsilon S_{rad\,i}\left(T_{s\,i}^4 - T_{f\,i}^4\right) - 2h_{cont}S_{cont\,i}\left(T_{s\,i} - T_{f\,i}\right)\right] \tag{29}$$

This approach was further adapted to the two different FS configuration applied on TCP. All the adopted physical constants are summarized in Tab. II-2 and further discussed in Chapt. 3.1.

Symbol	*Quantity*	*Value*	*Unit*	*Ref.*
C_p	Specific Heat	0.7	J g^{-1} K^{-1}	[115]
ε	Optical Emissivity	0.8	/	
h_{cont}	Contact Conductivity	10	W m^{-2} K^{-1}	[114]
σ_{SB}	Stefan-Boltzmann Constant	$5.67\cdot10^{-8}$	W m^{-2} K^{-4}	
R_g	Gas Constant	8.31	J K^{-1} mol^{-1}	

Table II - 2. Physical constants used in the thermal equations.

An alternative way to determine T_s is to employ an electrical property of the material, for instance the resistivity ρ_s, that depends on the temperature:

$$\rho_s = \rho_{0s} \exp\left(\frac{Q_s}{R_g T_s}\right) \tag{30}$$

Such equation shows an Arrhenius-like trend, that is typical of an ionic conductor [82], with ρ_{0s} as a pre-exponential coefficient, Q_s the activation energy of the process, and R_g the perfect gas constant. In addition, the same relation can be extended at the resistance of the samples, being the two quantities linked by geometrical parameters:

$$R_s = \frac{\rho_s L_0}{\pi r_0^2} = R_{0s} \exp\left(\frac{Q_s}{R_g T_s}\right) \tag{31}$$

However, Q_s and ρ_{0s} (or R_{0s}) can be graphically determined by fitting the measured resistivity before the flash event, when $T_s \approx T_f$, according to the linearized form:

$$\ln \rho_s = \ln \rho_{0s} + \frac{Q_s}{R_g} \frac{1}{T_f} \tag{32}$$

Finally, by extending the Arrhenius behavior beyond the flash event, the sample temperature T_{extra} can be extrapolated by inverting the above equation:

$$T_{extra} = \frac{Q_s}{R_g \ln(\rho_s / \rho_{0s})} \tag{33}$$

2.7.1 Cylindrical samples – Isochronal FS

For the cylindrical specimens with radius *r* and length *L*, considering the axial-symmetry of the FS configuration adopted, the heat losses by contact occur basically through the base surfaces of the ceramic samples, placed in contact with the flat electrodes, whereas the radiative area corresponds to the lateral surface of the cylinder. In addition, being the tests performed within the dilatometer, it is possible to measure the instantaneous length variation and calculate the actual surface, under the hypothesis of an isotropic shrinkage *e* of the material:

$$e = \frac{L_0 - L_i}{L_0} = \frac{r_0 - r_i}{r_0} \tag{34}$$

$$S_{rad\,i} = 2\pi r_0 L_0 (1-e)^2 \tag{35}$$

$$S_{cont\,i} = \pi r_0^2 (1-e)^2 \tag{36}$$

Eq. 29 becomes:

$$T_{s\,i+1} = T_{s\,i} + \frac{t_{i+1} - t_i}{mC_P}\left[V_i I_i - 2\pi r_0 (1-e)^2 \left(\sigma_{SB}\varepsilon L_0 \left(T_{s\,i}^4 - T_{f\,i}^4\right) + h_{cont} r_0 \left(T_{s\,i} - T_{f\,i}\right)\right)\right] \tag{37}$$

Nevertheless, such thermal approach can be further used to predict the conditions leading to the flash event or, from a different point of view, to estimate the onset temperature T_{on} at which the applied electric field induces the massive current flow inside the material, and its shrinkage. In order to do that, the electrical quantities should be conveniently converted into their local forms:

$$V = EL_0 \tag{38}$$

$$I = J\pi r_0^2 \tag{39}$$

$$W_{in} = VI = EJ\,\pi r_0^2 L_0 = \frac{E^2}{\rho_s}\pi r_0^2 L_0 \tag{40}$$

For these calculations, the sample dimensions are assumed constant at their initial values: this is quite realistic being the shrinkage almost negligible up to the flash event. Therefore, Eq. 28 becomes:

$$mC_p \frac{dT_s}{dt} = \frac{E^2}{\rho_{0s}} \exp\left(-\frac{Q_s}{R_g T_s}\right)\pi r_0^2 L_0 - 2\pi r_0 \left(\sigma_{SB}\varepsilon L_0 \left(T_s^4 - T_f^4\right) + h_{cont} r_0 \left(T_s - T_f\right)\right) \tag{41}$$

and dividing both the terms for the sample volume $\pi r_0^2 L_0$:

$$\frac{dT_s}{dt} = \frac{1}{\delta_{green} C_p}\left[\frac{E^2}{\rho_{s0}} \exp\left(-\frac{Q_s}{R_g T_s}\right) - \frac{2\sigma_{SB}\varepsilon}{r_0}\left(T_s^4 - T_f^4\right) - \frac{2h_{cont}}{L_0}\left(T_s - T_f\right)\right] \tag{42}$$

where δ_{green} is the density of the green specimen. Then, a change of integral variable is performed on the basis of the heating treatment adopted (i.e. constant rate *v*):

$$T_f = T_0 + vt \tag{43}$$

$$dt = dT_f / v \tag{44}$$

$$\frac{dT_s}{dT_f} = \frac{1}{\delta_{green} C_p v}\left[\frac{E^2}{\rho_{s0}} \exp\left(-\frac{Q_s}{R_g T_s}\right) - \frac{2\sigma_{SB}\varepsilon}{r_0}\left(T_s^4 - T_f^4\right) - \frac{2h_{cont}}{L_0}\left(T_s - T_f\right)\right] \tag{45}$$

and the overall equation is transformed in an adimensional form:

$$\frac{d\tilde{T}_s}{d\tilde{T}_f} = a \exp\left(-\frac{1}{\tilde{T}_s}\right) - b\left(\tilde{T}_s^4 - \tilde{T}_f^4\right) - c\left(\tilde{T}_s - \tilde{T}_f\right) \tag{46a}$$

$$\tilde{T} = \frac{R_g}{Q_s} T \qquad a = \frac{E^2}{\rho_{0s}\delta_{green} C_p v} \qquad b = \frac{2\sigma_{SB}\varepsilon Q_s^4}{r_0 \delta_{green} C_p v R_g^4} \qquad c = \frac{2h_{cont} Q_s}{L_0 \delta_{green} C_p v R_g} \tag{46b}$$

A representative example of the differential equation shape is reported in Fig. II-4, corresponding to E = 1000 V cm^{-1}, v = 20 K min^{-1}, and δ_{green} = 1.80 g cm^{-3} (~ 60% of the theoretical density of β-TCP). The equation was solved by Wolfram Mathematica software (ver. 10.3) using NDSolve command and imposing T_s equal to T_f at 300 K as the boundary condition.

According to the thermal model, the process can be divided in two main steps:

- At the beginning, sample and furnace temperature are substantially the same, being the current flow in the material negligible. Hence, the heating treatment is governed by the furnace;

- Upon the flash event, the sample temperature significantly diverges from the furnace temperature. The heating control is completely managed by the Joule effect.

As a consequence, the onset of the flash event could be found by imposing a switchover condition between the furnace and the Joule regimes, namely when the Joule heating contributions (~*a*) equals the furnace heating by radiation (~*b*) and by the imperfect contact between specimen and electrodes (~*c*), the latter being considered in thermal equilibrium with the furnace [116][106]:

$$a \exp\left(-\frac{1}{\widetilde{T_s}}\right) = b\widetilde{T_f^4} + c\widetilde{T_f} \tag{47}$$

this representing the red plot in Fig. II-4. The onset temperature T_{on} is given by the intersection of the lines and is well approximated by the relation:

$$\beta\, a \exp\left(-\frac{1}{\widetilde{T_{on}}}\right) = b\widetilde{T_{on}^4} + c\widetilde{T_{on}} \tag{48}$$

where β is an empirical correction coefficient to compensate the approximation between the switchover condition (Eq. 47) and the onset temperature prevision (Eq. 48) [116].

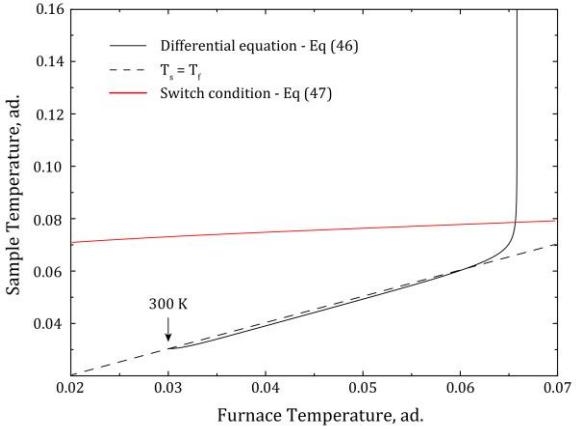

Figure II - 4. Graphical representation of the differential thermal equation (Eq. 46, black line) and the switch condition (Eq. 47, red line). Dashed line represents the relation $T_s = T_f$.

Finally, returning to the real physical quantities:

$$T_{on} = \frac{Q_s}{R_g}\left(-\ln\left[\frac{2\rho_{0s}}{\beta E^2}\left(\frac{\varepsilon\sigma_{SB}}{r_0}T_{on}^4 + \frac{h_{cont}}{L_0}T_{on}\right)\right]\right)^{-1} \tag{49}$$

This equation is used to fit the experimental data about the flash onset temperature, observed by changing the electric field E and the length L_0 of β-TCP cylindrical specimens. It is quite interesting that the system is completely described through the electric features of the materials (Q_s and ρ_{0s}, i.e. resistivity) and the heat exchange parameters (ε and h_{cont}), whereas C_p or δ_{green} are no longer present in this final expression.

2.7.2 Dogbone samples – Isothermal FS

For dogbone-like specimens, despite the more complex geometry, the above equations are simplified by removing the heat losses by conduction: the samples are suspended by the Pt wires within the furnace, and the contact interface between electrodes and material is not significant. The radiative surface S_{rad} was calculated as the lateral area of the rectangular central section (u x w x z), and assumed constant up to the flash event:

$$S_{rad} = 2u(w+z) \cong 190mm^2 \tag{50}$$

Therefore, the sample temperature evolution can be expressed by:

$$T_{s\,i+1} = T_{s\,i} + \frac{t_{i+1} - t_i}{mC_P}[V_i I_i - \sigma_{SB}\varepsilon S_{rad}(T_{s\,i}^4 - T_{iso}^4)] \tag{51}$$

where T_{iso} is the target temperature of the furnace, which is a constant.

As for the FS descriptive equations, a slightly different approach is adopted, based on the isothermal model proposed by Todd et al. [105]. According to that, if the difference between the constant furnace temperature T_{iso} and the real sample temperature T_s is expressed as:

$$\Delta T = T_s - T_{iso} \tag{52}$$

the produced power (W_{in}) and the evolved power (W_{out}) can be written, for the specific geometry, as:

$$W_{in} = uwz\frac{E^2}{\rho_{0s}}\exp\left(-\frac{Q_s}{R_g(T_{iso}+\Delta T)}\right) \tag{53}$$

$$W_{out} = 2u(w+z)\,\sigma_{SB}\varepsilon((T_{iso}+\Delta T)^4 - T_{iso}^4) \tag{54}$$

and represent, respectively, the heating and the cooling curves of the system.

The flash event occurs when, by imposing a sufficiently intense electric field E^*, the heating curve increases to become tangential to the cooling function (Fig. II-5). Therefore, once the material is overheated beyond a critical ΔT^* by means of Joule effect, the power losses increase less than the power produced, and a thermal-runaway mechanism takes place. The condition of tangency is realized when both $W_{in} = W_{out}$ and $dW_{in}/d\Delta T = dW_{out}/d\Delta T$ are verified:

$$uwz\frac{E^2}{\rho_{0s}}\exp\left(-\frac{Q_s}{R_g(T_{iso}+\Delta T)}\right) = 2u(w+z)\,\sigma_{SB}\varepsilon\left((T_{iso}^4+\Delta T^4) - T_{iso}^4\right) \tag{55a}$$

$$uwz\frac{E^2}{\rho_{0s}}\exp\left(-\frac{Q_s}{R_g(T_{iso}+\Delta T)}\right)\left(\frac{Q_s}{R_g(T_{iso}+\Delta T)^2}\right) = 8u(w+z)\,\sigma_{SB}\varepsilon(T_{iso}+\Delta T)^3 \tag{55b}$$

which allow to define the critical E^* and ΔT^*:

$$\frac{4R_g}{Q_s}(T_{iso}+\Delta T^*)^5 - (T_{iso}+\Delta T^*)^4 + T_{iso}^4 = 0 \tag{56a}$$

$$E^* = \left(\frac{8(w+z)}{wz}\frac{\sigma_{SB}\varepsilon\rho_{0s}R_g}{Q_s}\exp\left(\frac{Q_s}{R_g(T_{iso}+\Delta T)}\right)(T_{iso}+\Delta T^*)^5\right)^{1/2} \tag{56b}$$

The material heating is then usually limited by the power supply system, switching the control from voltage to current. The produced power starts to decrease, up to intersect the cooling curve and achieving a new equilibrium, according to:

$$W_{in} = uwz\, J^2 \rho_{0s} \exp\left(\frac{Q_s}{R_g(T_{iso} + \Delta T)}\right) \tag{57}$$

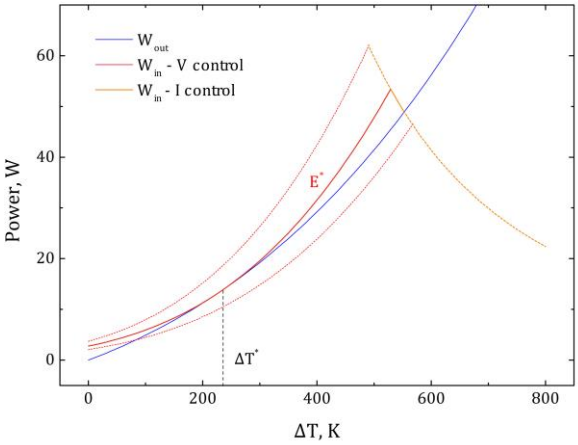

Figure II - 5. Graphical representation of the cooling curve W_{out} (Eq. 54, blue line), the heating curves W_{in} in the voltage control step (Eq. 53, red lines) for different electric fields, and the heating curves W_{in} in the current control step (Eq. 57, orange line). Critical conditions E^* and ΔT^* are also reported.

Chapter III

Results and Discussion

3.1 Solid state reaction: Magnesium doping β-TCP

This chapter is partially based on the published work:

Frasnelli M, Sglavo V.M: Effect of Mg^{2+} doping on beta-alpha phase transition in tricalcium phosphate (TCP) bioceramics, Acta Biomaterialia 33 (2016): 283–289.

3.1.1 Powder characterization

ICP-OES data are summarized on Tab. III-1, providing (Ca+Mg)/P atomic ratios very similar to the stoichiometric value of 1.50, typical for TCP. Other elements, such as Na, K, Sr, and Fe, were detected in quantity lower than 50 ppm. Conversely, Mg/(Ca+Mg) molar ratio, especially for the Mg1 composition, is slightly different from the nominal value. Nevertheless, such variations are taken into account in the following discussion by plotting the measured quantities as a function of the real Mg^{2+} amount (i.e. by ICP).

Sample	*nominal Mg,* mol%	*Mg/(Ca+Mg),* mol%	*(Ca+Mg)/P,* at. ratio	*Formula*	*MW,* g mol^{-1}
Mg0	0	0.00 ± 0.04	1.500 ± 0.001	$Ca_3(PO_4)_2$	310.18
Mg1	1	0.79 ± 0.04	1.507 ± 0.001	$Ca_{2.98}Mg_{0.02}(PO_4)_2$	309.86
Mg2	2	2.03 ± 0.04	1.508 ± 0.001	$Ca_{2.94}Mg_{0.06}(PO_4)_2$	309.23

Table III - 1. Chemical composition of the synthesized powders, determined by ICP-OES, proposed formula and estimated molecular weight MW.

For what concerns the crystalline phase composition, all powders show the typical reflection pattern of β-TCP polymorph, as reported in Fig. III-1. By increasing the dopant content peaks gradually shift to higher 2θ angles, thus proving the effective

incorporation of Mg^{2+} ions within the TCP structure and the consequent distortion of the crystalline cell. In addition, no signals related to MgO are present in the spectra.

Anyway, small and negligible amounts of HA can be detected and quantified by the weak peaks at ~31.77°, in agreement with the positive deviations from the Ca/P ratio of 1.50, as predicted by the $CaO–P_2O_5–H_2O$ phase diagram of Fig. I-2 [28][29]. Most likely, this is due to the incomplete reaction between H_3PO_4 and HA at ~800°C, during one of the last thermal decompositions leading to the formation of TCP by solid-state route [109].

$$3\ Ca_{10}(PO_4)_6(OH)_2 + 2\ H_3PO_{4\ (res)} \rightarrow 10\ Ca_3(PO_4)_2 + 6\ H_2O \quad (58)$$

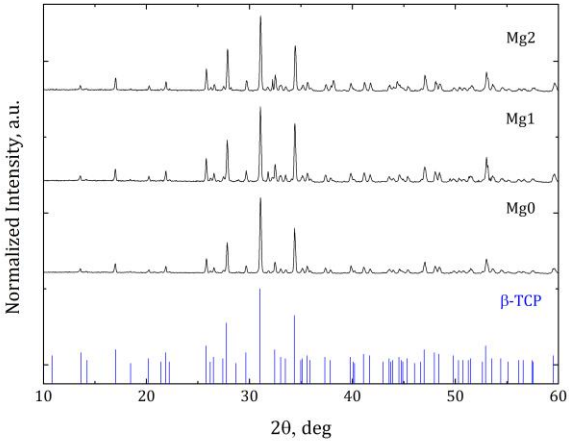

Figure III - 1. XRD patterns collected on the synthesized Mg-TCP powders. Blue vertical lines represent β-TCP (#09-0169) JCPDS reference.

Spectrum refinement (Tab. III-2) by Rietveld-based software allowed also to determine the cell parameters (*a* and *c*) for the Mg-TCP series, confirming the gradual cell contraction as a result of the M(5)-O bond stabilization [117]. Also the average crystallite size is subjected to an evident drop, moving from ~700 nm (Mg0) to ~300 nm (Mg2), similarly to the Sr-doped HA system (Chapt. 3.3) where the presence of secondary Me^{2+} ions promotes the crystal nucleation and inhibits their growth [118]. It has to be pointed out that crystallite size values higher than 200-300 nm can not be considered absolutely meaningful, due to the predominant contribution of the

instrumental broadening on the peaks; however, the observed trend as a function of Mg^{2+} presence is thought to be still significative.

Sample	*β-TCP*, wt%	*a*, 0.1 nm	*c*, 0.1 nm	*XS*, nm	*HA*, wt%
Mg0	98.0 ± 0.0	10.4357 ± 0.0006	37.3890 ± 0.0002	706 ± 90	2.0 ± 0.3
Mg1	94.0 ± 0.0	10.4259 ± 0.0006	37.3850 ± 0.0002	515 ± 37	6.0 ± 0.4
Mg2	98.0 ± 0.0	10.4071 ± 0.0003	37.3540 ± 0.0002	301 ± 24	2.0 ± 0.3

Table III - 2. Refined unit cell parameters (*a* and *c*), crystallite sizes (*XS*) and phase quantities obtained by XRD.

The thermal behavior of the synthesized Mg-TCP powders is reported as DTA plot in Fig. III-2

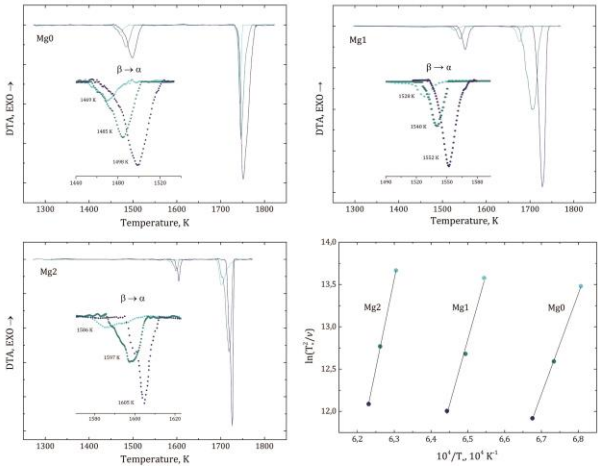

Figure III - 2. DTA curves of the synthesized Mg-TCP powders, carried out at different constant heating rate, and corresponding Kissinger plot: light blue dots (2 K min^{-1}), turquoise dots (5 K min^{-1}), and dark blue dots (10 K min^{-1}).

According to the literature [50], two endothermic signals characterize all the compositions: a weak peak around 1500-1600 K, related with β→α transition and postponed by increasing Mg^{2+} , and a more intense event at 1750 K, associable to α→α' reverse transformation.

The isochronal approach points out how by increasing the heating rate *v* for the same Mg-TCP composition, peaks are gradually shifted, sharper and intense. As for the β→α event (inserts), linear fitting of the identified temperatures by using Kissinger equation (Eq. 17) provides the activation energy of the process for the different specimens (Tab. III-3). For the undoped composition Mg0, a value of 237 kcal/mol was calculated, in good agreement with the value 250 kcal/mol reported in the literature [46]. This significantly large amount of energy can be justified taking into account the reconstructive nature of the phase transition considered, involving a drastic change in the lattice from rhombohedral to monoclinic structures. Conversely, the substitution of 0.79 and 2.03 mol% Ca^{2+} by Mg^{2+} leads to much higher activation energies, 310 and 421 kcal/mol, respectively, associated to the thermodynamic effect of the enhanced structural stability of β-TCP polymorph.

	Mg0	*Mg1*	*Mg2*
Differential Thermal Analysis			
β→α temperature, K			
at 2 K min^{-1}	1469	1528	1586
at 5 K min^{-1}	1485	1540	1597
at 10 K min^{-1}	1498	1552	1605
Kissinger fitting, Eq. 17			
Slope, K^{-1}	119277	156004	212142
Intercept	-67	-88	-120
R^2	0.999772	0.994097	0.999789
Q, kcal/mol	237	310	421
Dilatometry			
β→α temperature, K	1501	1553	1682
Shrinkage at 1800 K, %	2.24	5.76	9.01

Table III - 3. Collected data about the thermal behavior of Mg-TCP powders: β→α temperatures by DTA and dilatometry, final shrinkage and Kissinger fitting details.

The positive effect of Mg has implications for the sintering behavior of the powders as well. As it can be noticed from the dilatometric plot of Fig. 14, sintering starts at ~1200 K, but once β→α transition occurs, shrinkage is almost completely arrested, as a consequence of the TCP lattice expansion [53]. Nevertheless, an increment of transition temperature from 1500 K (Mg0) to 1680 K (Mg2) leads to enhance the final shrinkage from 2 to 9 %, respectively.

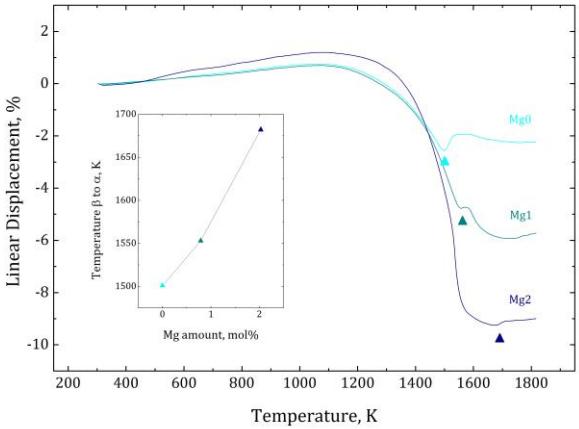

Figure III - 3. Dilatometric plot of the synthesized Mg-TCP powders: light blue line (Mg0), turquoise line (Mg1), and dark blue line (Mg2). Triangles indicate β→α temperatures, which are additionally plotted as a function of Mg amount (insert).

3.1.2 Conventional sintering

Tab. III-4 summarizes the XRD quantitative results of Mg-TCP samples sintered at 1400°C, and then alternatively cooled at 10°C/min (C series), or quenched in static air (Q series). The target temperature was chosen accordingly to DTA observation, in order to completely transform each composition into α-TCP and, in this way, to investigate the dopant influence on the α- metastability upon cooling. In detail, the maximum β→α temperature at 10°C/min (i.e. heating rate of the sintering treatments) was determined for Mg2 composition equal to 1332°C (1605 K); in addition, two additional hours of isotherms should ensure the thermodynamic equilibrium of the entire specimen.

Crystalline compositions of Mg0, indeed, confirm the previous hypothesis: regardless the cooling treatment, at room temperature the sintered material is formed

entirely by metastable α-TCP, as expected. Conversely, Mg1_C exhibits 46 wt% of β phase, this proving the partial and spontaneous reconversion of α-TCP into β-TCP upon the cooling process. By increasing the dopant amount, Mg2_C is even completely formed by β-TCP. Therefore, it can be pointed out that Mg also provides a positive contribution on β stabilization, inhibiting the α meta-stabilization upon cooling, very likely decreasing the activation energy of the α→β process. The effect, proportional to the dopant amount, has further kinetic consequences. By observing the Q series, Mg1 composition is completely α-TCP, whereas Mg2 appears partially reconverted (64 wt% β) despite the quenching treatment. In other words, Mg increases the critical cooling rate required to retain α phase at room temperature, allowing to accelerate the post-sintering treatments of β-TCP compounds.

Sample	*β phase,* wt%	*α phase,* wt%	ρ_{th}, g cm^{-3}
Mg0_C	0 ± 0	100 ± 0	2.86
Mg1_C	46 ± 2	54 ± 0	2.97
Mg2_C	100 ± 0	0 ± 0	3.06
Mg0_Q	0 ± 0	100 ± 0	2.86
Mg1_Q	0 ± 0	100 ± 0	2.86
Mg2_Q	64 ± 2	36 ± 2	2.99

Table III - 4. Crystalline composition (by XRD) and theoretical density ρ_{th} of the sintered Mg-TCP specimens, subjected to controlled cooling (C series) or quenching (Q series).

Sample	P_{open}, vol%	P_{closed}, vol%	ρ/ρ_{th}, %	*HV*, MPa	σ_B, MPa
Mg0_C	25 ± 1	5 ± 1	70	817 ± 60	31 ± 1
Mg1_C	20 ± 2	6 ± 1	74	1109 ± 153	18 ± 2
Mg2_C	8 ± 1	8 ± 1	84	1370 ± 83	32 ± 2
Mg0_Q	29 ± 1	1 ± 1	70	439 ± 84	9 ± 1
Mg1_Q	22 ± 1	2 ± 1	76	675 ± 91	11 ± 3
Mg2_Q	11 ± 2	4 ± 1	85	856 ± 104	5 ± 3

Table III - 5. Open porosity P_{open}, closed porosity P_{closed}, relative density ρ/ρ_{th}, Vickers hardness *HV*, and mechanical strength σ_B of the sintered Mg-TCP specimens, subjected to controlled cooling (C series) or quenching (Q series).

For what concerns the microstructure of the sintered samples, Archimedes' measurements (Tab. III-5) are in good agreement with the preliminary conclusions drawn by dilatometry: shrinkage was arrested upon the first sintering stages, when porosity is still predominant (20-30 vol%) and interconnected. Only for the Mg2 composition, β→α transition takes place when pores are partially isolated, i.e. open porosity is comparable with closed porosity, and 85% densification was achieved. As expected, cooling process does not seem to influence such features.

Further microstructural evidences can be found by observing the SEM images (Fig. III-4) of the polished and indented sample surfaces. Within the impression area, plastic deformation induces the closing of the interconnected porosity; diagonals are clearly visible and no cracks at the edge are present.

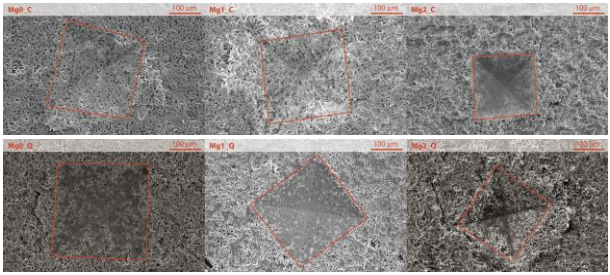

Figure III - 4. SEM images of representative Vickers indentation on the Mg-TCP sintered samples: C series (first row), and Q series (second row).

Vickers hardness results are summarized in Tab. III-5 and, as expected, the values grow with the dopant amount, from ~800 MPa (Mg0_C) to ~1350 MPa (Mg2_C), being the hardness strictly related with the microstructure and sintering behavior. At the same time, quenching introduces evident thermal stresses, leading to a decrease of 400-500 MPa but maintaining the same trend (Fig. III-5). Moreover, the samples presenting the most disperse data are Mg1_C and Mg2_Q, the only two cases of biphasic composition (β and α phase) after the respective cooling treatment.

Surprisingly, the mechanical resistance σ_B of the sintered pellets does not increases linearly with Mg^{2+}; no regular tendencies along C or Q series can also be observed. The only clear conclusion is that the thermal stresses induced by quenching reduce the material strength. However, the specimens interrupting the linear and positive trend along the single series are, also in this case, the biphasic composition Mg1_C and Mg2_Q. Despite the lack of performed measurements and the few

compositions considered, an explanation of this effect based on residual stresses can be proposed. More in detail, β to α transition taking place during sintering causes a volumetric expansion which completely involves the material, since β phase turns into α completely. In this way, residual stress can be easily relaxed, also considering the high temperature involved (1400°C). Then, upon cooling, Mg^{2+} promotes α to β spontaneous reconversion, associable with a volumetric shrinkage. If this reverse transition takes place completely (Mg2_C), residual stress can be once again relaxed during the controlled cooling. Conversely, if the reconversion occurs just partially, and both α and β phases are retained at room temperature, a residual tensile stress around ~10 MPa arises within the material, decreasing the final mechanical strength.

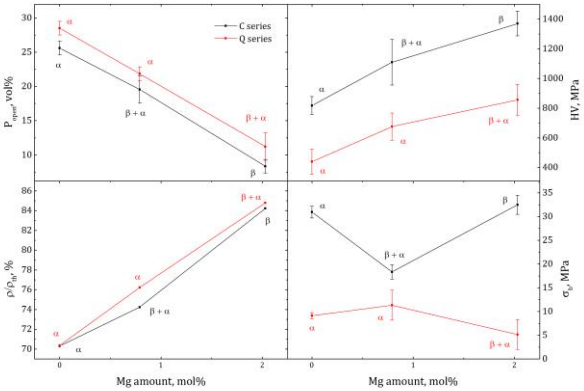

Figure III - 5. Open porosity P_{open}, relative density ρ/ρ_{th}, Vickers hardness *HV*, and mechanical strength σ_B of the sintered Mg-TCP specimens, as a function of Mg dopant amount: black line (C series), and red line (Q series). Crystalline phases detected by XRD have been also reported for clarity.

3.1.3 Annealing

The dilatometric plots of the sintered and quenched Mg-TCP specimens, subjected to an annealing treatment at constant heating rate (2°C/min), are reported in Fig. III-6. All compositions exhibit a very similar thermal expansion, with an average linear coefficient of $11.2 \cdot 10^{-6}$ °C^{-1}.

Then, just for the doped samples, a linear contraction is clearly observable around 1000 K, more intense for Mg1_A composition. By considering the

corresponding results about the crystalline phase composition by XRD (Tab. III-6), the event is associable with the reconversion of the retained α-TCP into β: undoped TCP is still formed by α phase, only, whereas Mg1_A and Mg2_A are both β phase.

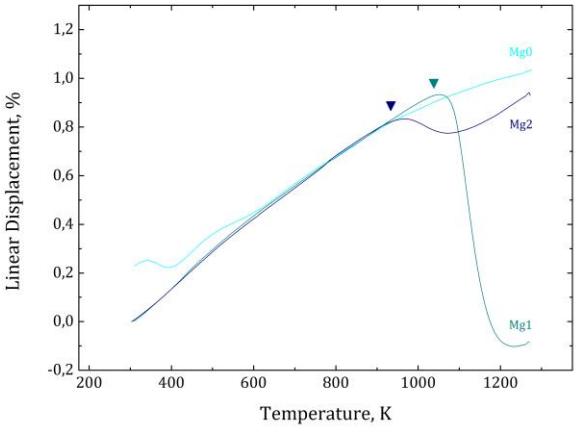

Figure III - 6. Dilatometric plot of the sintered and quenched Mg-TCP samples (A series): light blue line (Mg0), turquoise line (Mg1), and dark blue line (Mg2). Triangles indicate α→β temperatures.

Actually, this transition can occur also in absence of any dopant agent, as shown by Monma et al. [46], although the annealing treatment was applied to finer powders and not to massive bodies. Simply, if the active surface of the particles is reduced by sintering, a reconstructive process like α→β, governed by mass transport and, therefore, strictly dependent from the temperature, would require longer time to occur. Once again, Mg acts on the activation energy of the transition, allowing the complete reconversion into β and proportionally decreasing the α→β temperature.

Sample	*β phase*, wt%	*α phase*, wt%	*α→β temperature*, K
Mg0_A	0 ± 0	100 ± 0	/
Mg1_A	100 ± 0	0 ± 0	1038
Mg2_A	100 ± 0	0 ± 0	933

Table III - 6. Crystalline composition (by XRD) and α→β temperature of the sintered and quenched Mg-TCP specimens, subjected to annealing at 2°C/min by dilatometry (A series).

Moreover, it should be recalled that β→α transition is related with a lattice expansion; therefore, the inverse reaction is likely combined with a contraction, proportional to the amount of meta-stabilized α. Therefore, a linear shrinkage of ~0.1% for Mg2, having only 36 wt% of α after quenching, is reasonably smaller than the measured ~1% for Mg1, being 100 wt% α.

As an additional information, XRD spectra of Mg2 composition is reported in Fig. III-7 by varying the thermal treatment adopted.

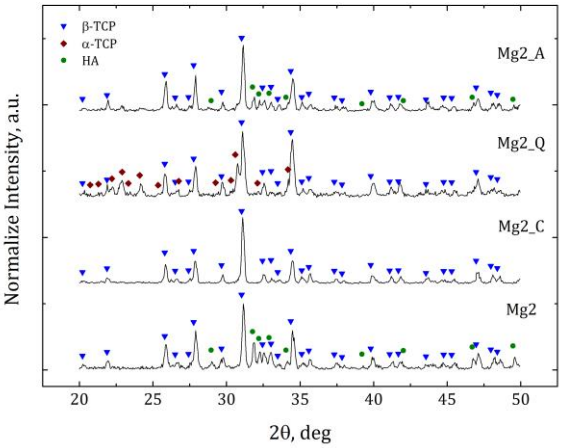

Figure III - 7. Crystalline phase evolution of a representative composition (Mg2) as a function of the different heating and cooling treatments: controlled cooling (Mg2_C), quenching (Mg2_Q), and annealing (Mg2_A). Symbols are referred to JCPDS cards #09-0169 (β-TCP, blue triangles), #09-0348 (α-TCP, red squares), and #09-0432 (HA, green circles), respectively.

Finally, the kinetic of α→β was investigated by carrying out isothermal annealing treatments at different times and temperatures. Mg1 sintered and quenched specimens were selected for the test, being possible for this composition to completely retain α-TCP at room temperature. As it can be noticed in Fig. III-8 (central), experimental points show a sigmoidal increment of the β-TCP transformed fraction w_β, by increasing the annealing time and temperature. For instance, after 3 h treatment (i.e. 10800 s, ln t ≈ 9.3), 15% (700°C), 34% (730°C), and 90% (775°C) reconversion occurred.

Therefore, each temperature series were fitted by using the linearized Avrami equation (Eq. 18b), leading to the determination of the corresponding kinetic factors *k(T)*. Slopes of the model lines, corresponding to the Avrami coefficient *n*, have been forced to be the same for the three series. In addition, activation energy *Q* of the process was calculated from the linear regression of kinetic factors, performed by using the Arrhenius law (Eq. 19b). Tab. III-7 shows the fitting parameters and the achieved results: for Mg1 composition, α→β is governed by n = 1.32 and Q = 66 kcal/mol, substantially lower than the value of 310 kcal/mol needed for β→α transition and compatible with the previous considerations.

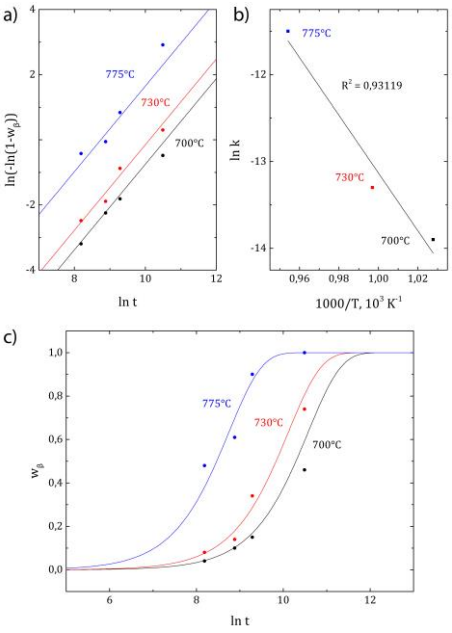

Figure III - 8. Avrami plot of the isothermal annealing treatments performed on Mg1 composition: black lines and points (700°C), red lines and points (730°C), and blue lines and points (775°C). From the left, linearized fitting (a) and cumulative plot (c) of the transformed phase w_β. On the right, kinetic coefficient as a function of temperature (b).

Temperature, °C	700	730	775
Avrami linear fitting, Eq. 18b			
Slope	1.3151	1.3151	1.3151
Intercept	-13.9	-13.3	-11.5
R^2	0.955917	0.964365	0.918607
Avrami coeff. n	1.32	1.32	1.32
Kinetic factor k	$9.19 \cdot 10^{-7}$	$1.67 \cdot 10^{-6}$	$1.01 \cdot 10^{-5}$
Arrhenius linear fitting, Eq. 19b			
Slope, K^{-1}		-33224	
Intercept		20.1	
R^2		0.931190	
Q, kcal/mol		66	

Table III - 7. Linear fitting parameters of the β-TCP weight fractions w_β of Mg1 composition (by XRD) as a function of annealing time and temperature. Estimated Avrami coefficient n and activation energy Q of the α→β transition have been also reported.

3.1.4 Isochronal Flash Sintering

The following chapter is partially based on the published paper:

Frasnelli M, Sglavo V.M: Flash sintering of tricalcium phosphate (TCP) bioceramics, J. of the European Ceramic Society 38 (2018): 279-285.

3.1.4.1 Flash sintering behavior

The undoped TCP powder, shaped into cylindrical specimens and placed within the dilatometer, was subjected to different flash sintering tests at constant heating rate of 20°C min^{-1}, as reported above. Fig. III-9 shows the linear displacement detected during the sintering process, under constant electric field; the conventional dilatometry (i.e., with no field) is once again reported for comparison.

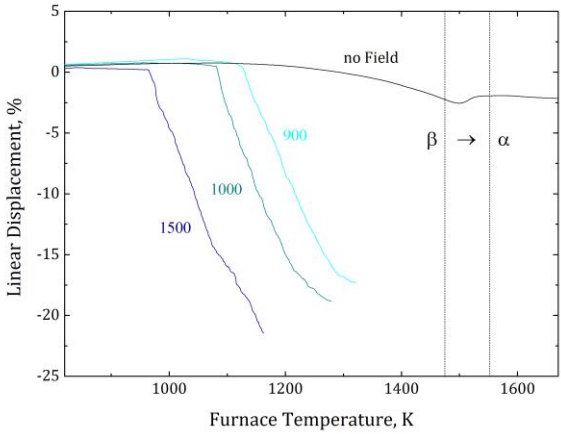

Figure III - 9. Dilatometric plots of TCP cylindrical specimens under conventional (i.e. no field) and FS conditions (10 min at 2 mA mm^{-2}). Numbers refer to the applied electric field (V cm^{-1}); vertical dotted lines represent the temperature range of β→α transition, determined by the first derivative of the conventional curve.

The FS curves show three effects:

- the starting point of the shrinkage, coincident with the onset temperature T_{on} of the flash event, is strongly anticipated by E, from 1125 K (900 V cm^{-1}) to 965 K (1500 V cm^{-1});

- the shrinkage takes place very rapidly, with an average rate of ~2 μm/s, whereas the conventional sintering proceeds at ~0.15 μm/s and, after the transition β→α, even more slowly (0.02 μm/s);

- for the entire FS process, the furnace temperature T_f remained below the β→α temperature.

As a direct consequence, the final shrinkage after only 10 min current control is around 20%, much higher than 2.3% value obtained without field: the relative density is 79% (900 V cm^{-1}), 86% (1000 V cm^{-1}), and 93% (1500 V cm^{-1}). Apparently, no phase transition occurs.

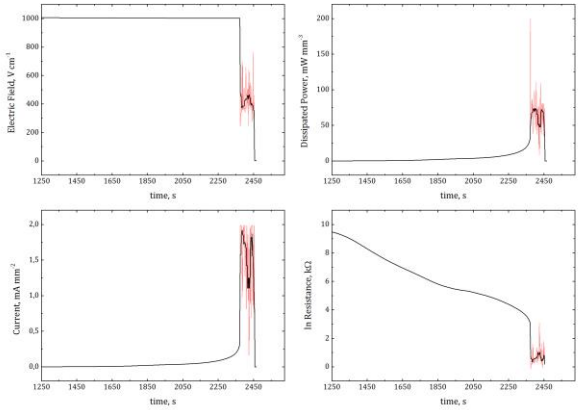

Figure III - 10. Representative example of FS test carried out at 1000 V cm^{-1}: electric field, current, power density, and resistance as a function of the process time; raw data (red lines) and smoothed data (black lines).

The behavior of TCP during flash sintering can be better understood through the evolution of its electrical features (Fig. III-10), which is quite similar to that reported in the literature for other materials [103]. Basically, the first stage of the process is characterized by the absolute constancy of the voltage and by the linearity of the logarithm of resistance, according to the Arrhenius law (Eq. 31); current and power density are both almost negligible, due to the limited temperature. As the test proceeds, and consequently T_f increases, the resistance decreases and the current starts flowing gradually through the material. This increment is not linear, but much more rapid: in few minutes the current limit is reached, and a power spike is detected in combination with a resistance drop. These phenomena clearly identify the onset of the flash event, as well the beginning of the rapid shrinkage observed by dilatometry. Then, the process must be switched to constant current mode, although all the electrical variables appear very scattered. The extended interface between the ceramic and the electrodes, indeed, seems to enhance the continue creation of multiple current paths, causing sparks and instantaneous variations of the field.

After these phenomenological considerations, the influence of the main technological variables, i.e. applied electric field and initial sample length L_0, on the overall FS process is quantified in terms of T_{on}. The aim is to determine the physical conditions inducing the flash event in TCP material and to find a descriptive model to explain and optimize such technology.

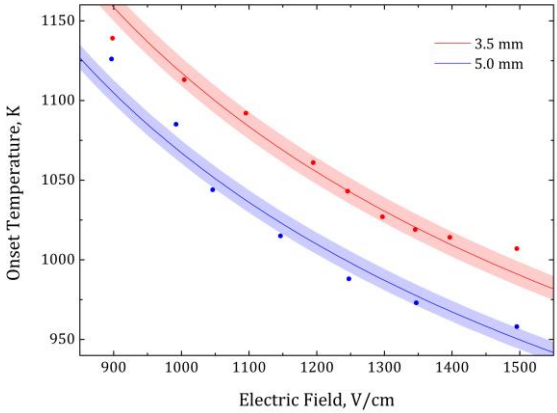

Figure III - 11. Experimental onset temperature T_{on} of the flash event, as a function of the applied electric field E, for sample length L_0 equal to 3.5 mm (red dots) and 5.0 mm (blue dots). Colored bands represent the best fits by using Eq. 49, considering an error of ± 0.1 mm on L_0.

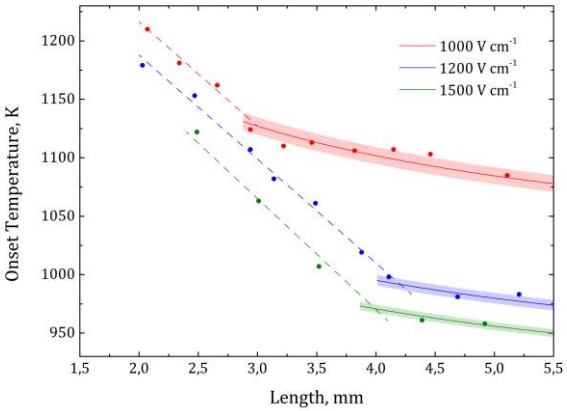

Figure III - 12. Experimental onset temperature T_{on} of the flash event, as a function of the sample length L_0, for applied electric fields E of 1000 V cm^{-1} (red dots), 1200 V cm^{-1} (blue dots), and 1500 V cm^{-1} (green dots). Colored bands represent the best fits by using Eq. 49, considering an error of ± 20 V cm^{-1} on E.

Fig. III-11 summarizes the experimental onset temperatures of two different L_0 series of specimens (3.5 and 5.0 mm) for different E: as observed in the dilatometric plots and reported for different materials [95], the field increment corresponds to a strong decrease of the furnace temperature at which flash occurs. In these specific conditions, T_{on} values are in the range 960-1130 K with the application of 1500-900 V cm^{-1}, respectively. It is quite meaningful that, if β-TCP was conventionally sintered in isothermal condition at 900°C (1173 K), temperature is not sufficient to activate any densification mechanisms, at least after 1 h (Fig. III-13), whereas at 1100°C (1373 K) the material shrinkage is just ~5% after 2 h. As a consequence, it can be stated that flash sintering allows to reduce both time and temperature with respect to conventional treatments.

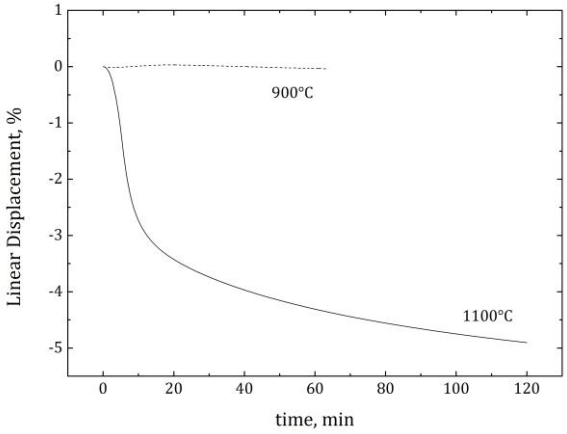

Figure III - 13. Dilatometric plot of the Mg0 composition, sintered in isothermal condition at 900°C (dashed line) and at 1100°C (solid line).

In addition, L_0 shows an apparently incoherent effect: flash event seems to be anticipated by longer samples, despite the higher mass and radiative surface. Such behavior is further confirmed in the second plot (Fig. III-12), relative to the onset temperature of three different E series (1000, 1200, and 1500 v cm^{-1}) by varying L_0. In addition, the dependence between T_{on} and sample dimension is strong and basically linear up to ~3-4 mm, and then suddenly becomes almost irrelevant.

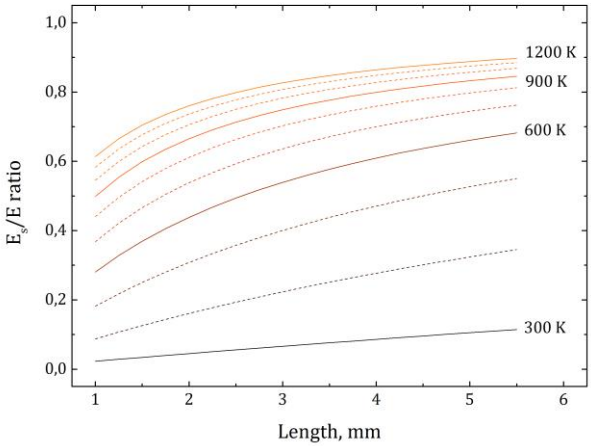

Figure III - 14. Representative trends of the sample field fraction E_s/E as a function of the initial sample length L_0, by varying the temperature.

The proposed explanation for this behavior consists in the introduction of an additional resistance term, independent from the sample length and correlated with the probable bias drop at the material-electrode interface, namely the contact resistance R_e. Therefore, the overall resistance R evaluated at the electrodes during the FS test (as V/I ratio) can be expressed as:

$$R = R_e + \frac{\rho_s L_0}{\pi r_0^2} \tag{59}$$

In other words, the system can be represented as two resistors in series, both described by their own Arrhenius law, the second one being directly proportional to L_0. Therefore, the fraction of electric field actually supplied to the material can be expressed as:

$$\frac{E_s}{E} = \frac{R_s}{R_s + R_e} = \frac{L_0}{L_0 + (R_e \pi r_0^2 / \rho_s)} \tag{60}$$

The relationship is plotted against L_0 in Fig. III-14, as a function of temperature: it is clear that the contact resistance affects to a greater extent shorter samples, which are subjected, around the flash event range, only to 60-80% of the nominal field. For instance, specimens with L_0 minor than ~3 mm and tested at 1200 V cm^{-1}, apart from

R_e, are effectively subjected to ~1000 V cm^{-1}, in good agreement with the experimental data of Fig. III-12.

Therefore, the contact resistance can be graphically quantified by Eq. 59, by plotting the total resistance R at three temperatures (lower than T_{on}), for a series of TCP specimens with different initial length L_0 (Fig. III-15). The intercepts of the linear fits provide the values of R_e (T), which is reported in the form of Arrhenius plot to determine the thermal parameters R_{e0} and Q_e (Tab. III-8).

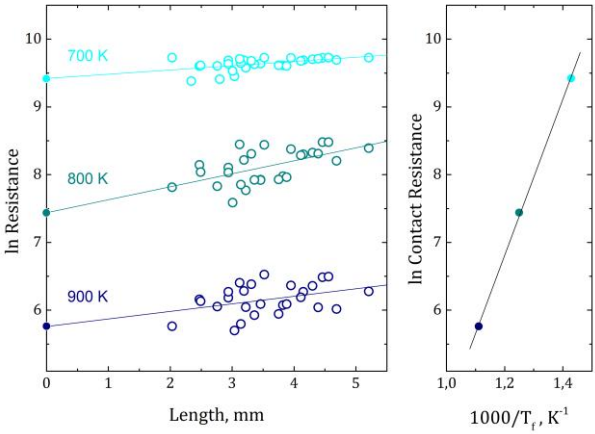

Figure III – 15. Graphical determination of the contact resistance R_e and its thermal parameters R_{e0} and Q_e. On the left, total resistance R determined at different temperatures by changing the initial length L_0 of the specimens, and linear fitting according to Eq. 59. On the right, Arrhenius plot of the so-determined R_e values (Eq. 31).

Finally, this contribution is subtracted from the total resistance R curves, obtaining the sample resistivity ρ_s as a function of temperature for various tested specimens (Fig. III-16); the average values of ρ_{s0} (0.0013 Ωm) and Q_s (82 kJ/mol) are in good agreement with similar previous work [84]. Since the resistivity curves are basically linear and parallel, the activation energy Q_s, proportional to the slope, shows slightly dispersive values; conversely, the line intercepts, equal to the logarithm of ρ_{s0}, are quite randomly scattered and the use of an average value, unfortunately, is one of the major source of error in the following data modelling.

Once the real electric behavior of TCP material is determined through ρ_{s0} and Q_s, Eq. 49 can be finally refined to fit the measured T_{on} points. More in detail, since the contact conductivity h_{cont} and the empirical correction coefficient β influence the fitting function in different ways (affecting the curve concavity / ~slope and its vertical onset, respectively) the two parameters were optimized simultaneously, but forcing the h_{cont} values to be equal for all experimental points series. The best fits are reported in Fig. III-11 and III-12 (β = 0.12-0.17) as colored bands, and appear completely coherent with the experimental observations. It can be stated, therefore, that the flash onset is mainly induced by a thermal runaway mechanism, well described by a power balance of the system. The influence of L_0 is now clearer: the longer the specimen, the lower is the heat dissipation by conduction, and therefore the thermal condition for flash event are achieved earlier.

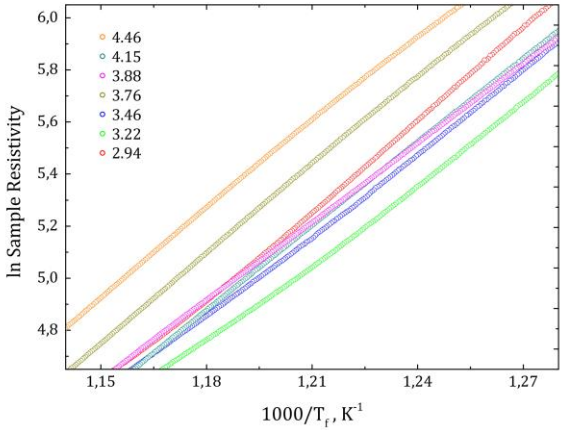

Figure III – 16. Arrhenius plot of the sample resistivity ρ_s (linear section) of TCP specimens with various initial lengths L_0 (mm, values reported in the legend), subjected to FS tests at different electric fields E.

For L_0 values lower than ~3 mm, the model diverges due to the prevalent contact resistance contribution, as explained before. In order to extend the validity and the accuracy of the fitting function, one possibility could be to take into account the actual sample field E_s rather than the nominal E, as well as the thermal parameters ρ_{s0} and Q_s for each different specimen, instead of the related average values. Nevertheless, this method would lead to a series of discrete points and not to a continuous function able to describe with sufficient precision the FS process on TCP material.

Arrhenius Linear Fitting	
Contact Resistance R_e, Eq. 31	
Slope, K^{-1}	11512
Intercept	-3.2
R^2	0.998820
Q_e, kJ/mol	96
R_{0e}, Ω	0.04
Sample Resistivity ρ_s, Eq. 32	
Average Slope, K^{-1}	9868
Average Intercept	-6.6
Q_s, kJ/mol	82
ρ_{0s}, Ωm	0.0013

Table III - 8. Activation energies and pre-exponential coefficients of contact resistance R_e, and sample resistivity ρ_s, graphically determined by Arrhenius-like approaches.

3.1.4.2 Microstructure and crystalline phases

Optical images collected in Fig. III-17 show the appearance of a representative TCP specimen after FS.

Focusing on the middle-cross section of the cylindrical sample, an inhomogeneous and burnished area is clear starting from the cathodic side (left) and proceeding to the core. Its extension, as observed after a large variety of tests, seems to be strictly proportional to the duration and to the intensity of the current control stage; namely, it is related to the number of electrons passing through the material upon the flash event. In the literature, similar blackening phenomena have been observed for other ceramic oxides [119] and explained by considering the partial reduction of the materials at the cathode, under poorly oxygen conditions.

As a matter of fact, the conduction mechanisms of β-TCP has been reported in the literature as being governed by ionic migration for temperatures higher than 800°C [120]. Similarly to HA, where the hydroxyl groups are responsible for the high temperature conductivity [121], oxygen ions O^{2-} have been proposed as the most probable charge carriers in β-TCP, with an activation energy of 1.25 eV [122]. However, migration of Ca^{2+}, or H^+ from partially protonated phosphate groups could also be possible [120].

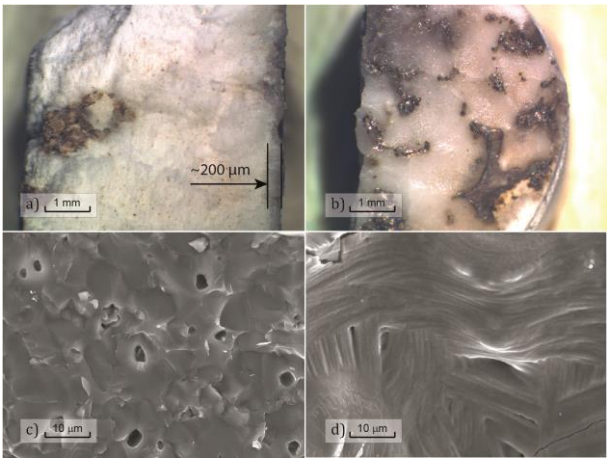

Figure III - 17. Optical and SEM images of a representative TCP sample (1500 V cm^{-1}): a) middle cross section (fracture surface); b) anodic surface; c) central portion of the bulk; d) blackened portion at the cathodic side.

Consequently, the following mechanism was here proposed to explain the blackening phenomenon. Specifically, the mutual charge transfer between the electrons (from the circuit) and the O^{2-} ionic carriers is realized at the ceramic-electrode interfaces through the reaction:

$$\frac{1}{2}\,O_2 + 2\,e^- + V_O^{\cdot\cdot} \rightleftharpoons O_O^{\times} \tag{61}$$

At the cathode surface, half molecule of environmental gaseous oxygen reacts with the electrons, forming one atomic oxygen O_O^x, which occupies a lattice vacancy $V_O^{\cdot\cdot}$, becoming formally neutral. Then, the charge transport in the material takes place by the O^{2-} migration toward the anode or, from the opposite point of view, by the $V_O^{\cdot\cdot}$ migration toward the cathode. At the anode surface, the inverse reaction occurs, with the production of O_2 gas, vacancies and electrons that balance the overall mass-charge of the system. Unfortunately, the cathodic reaction is strictly connected with the formation of a triple junction between oxygen / ceramic / electrode, that constitutes, as a matter of fact, the limiting factor of the entire process.

In the specific case of planar electrodes and cylindrical specimens, the oxygen supply is quite poor, especially when the material starts to densify and the open

porosity decreases. As a consequence, another semi-reaction occurs at the cathodic surface, involving TCP:

$$PO_4^{-3} + \delta\, V_O^{\cdot\cdot} + 2\delta\, e^- \rightarrow PO_{4-\delta}^{-3} + \delta\, O_O^{\times} \tag{62}$$

Substantially, the lack of O_2 is accommodated by the partial reduction of the phosphate groups PO_4^{-3}; phosphorous atoms locally assume a valence equal to 5-δ, thus resulting in a highly defected structure and in the black coloring. Therefore, the combination of Eq. 62 with the anodic reaction gives the global mechanism governing the current control stage:

$$PO_4^{-3} \rightarrow PO_{4-\delta}^{-3} + \frac{\delta}{2} O_2 \tag{63}$$

where it is quite clear, once again, that lower partial pressure of oxygen promotes the phosphate reduction and the blackening phenomena. On the other hand, a conventional heating treatment in air should allow, very likely, the oxygen diffusion within the specimen and the restoration of stoichiometric defects. Such effect was observed for flash sintered nano-TCP samples, where the heating ramp was maintained for additional ~10 min after the current were turned off (Chapt. 3.2).

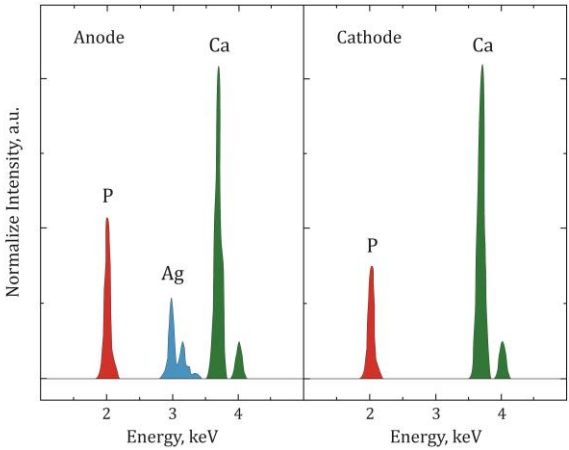

Figure III - 18. EDXS spectra of a representative TCP specimens after FS, relative to the anodic and cathodic bulk regions.

However, another peculiar characteristic of the FS specimens, shown in Fig. III-17, is the presence of an almost glassy and irregular layer (~200 μm) near the anodic side. According to the chemical reactions discussed before, the formation of gaseous oxygen at the anode interface could be responsible for a higher electrical resistance, very likely the predicted and quantified contact resistance R_e, thus causing local overheating and microstructural inhomogeneities. The surface shows some residues of oxidized silver paste and, only for some samples, a very small yellowish area, developed toward the bulk. For this latter, EXDS analysis (Fig. III-18) confirms the presence of Ag^+ ions diffused in the ceramic as a result of a secondary anodic reaction, whereas no silver was detected in the cathodic region.

Apart from these localized phenomena, the bulk appears homogeneous and dense, with some intergranular porosity and hexagonal-like grains of 5-7 μm. It is meaningful to recall that such microstructure was achieved after only 10 min maximum current application, whereas much longer conventional sintering process is able to ensure just 70% density, because of the β→α transition.

Interestingly, SEM image of the blackened cathodic zone provide evidences of the local formation of a liquid phase, being the microstructure typical of a melted and re-solidified material with a randomly oriented pattern. Probably, the partially reduction of the lattice induces a resistivity decrease, associated to greater $V_O^{\cdot\cdot}$ population, and therefore the current is preferentially canalized through the blackened zone, this leading to local thermal runaway and higher temperature. In any case, the CaO-P_2O_5-H_2O phase diagram (Fig. I-2) predicts, for Ca/P ratios slightly higher than 1.50, solidus around 1560 K [49].

As for the crystalline composition of FS specimens (Tab. III-9), the bulk material is essentially constituted by β-phase and just a very small amount (6 wt%) of α-TCP, thus validating the flash sintering as reliable technique to avoid the material transition (Fig. III-18).

	β phase, wt%	*α phase,* wt%	*HA phase,* wt%
Cathode	99 ± 1	0 ± 0	1 ± 0
Bulk	87 ± 2	6 ± 1	7 ± 1
Anode	62 ± 2	38 ± 2	0 ± 0

Table III - 9. Crystalline composition (by XRD) of the main portions of a representative FS specimen.

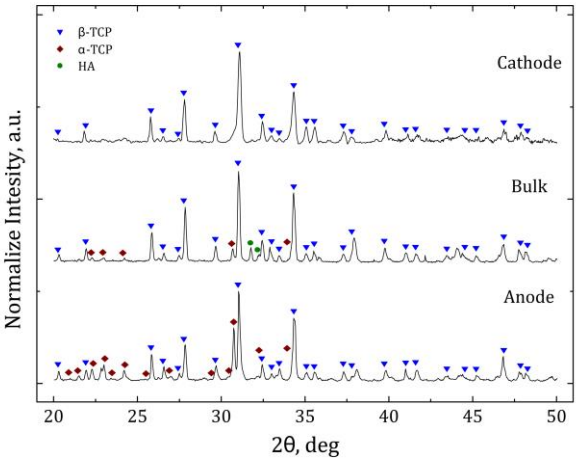

Figure III - 19. XRD patterns of different portions (cathode, anode, and bulk) of a representative TCP specimen (1000 V cm^{-1}). Symbols are referred to JCPDS cards #09-0169 (β-TCP, blue triangles), #09-0348 (α-TCP, red squares), and #09-0432 (HA, green circles), respectively.

Conversely, the anodic layer was mainly affected by the phase transformation, due to the strongly localized contact resistance, while the blackened area, in spite of the re-solidified structure, is formed entirely by β-TCP, very likely for kinetic reason. Similar behaviors were reported in other ultra-fast heating processes applied on TCP, as well as selective melting laser [123] and plasma spray [44].

Finally, the thermal balance of Eq. 37 was verified on different FS specimens, by plotting the calculated sample temperature T_S as a function of time (Fig. III-20). It should be recalled that, for the physical model here adopted, TCP samples are perfectly isotropic and homogeneous during the entire flash process. Although the previous considerations pointed out the presence of limited material portions clearly subjected to higher temperature, the approach can be still considered valid for the main part of the sintered body.

As expected, the curves exhibit quite similar trends to the power profiles, the differences between T_f and T_S being substantial once the Joule effect exceeds the furnace radiation. Upon the flash event, the sample temperature rapidly increases by ~400 K, and then fluctuates around an almost steady-state where β stability limit is

repeatedly surpassed for few seconds, in agreement with the small amount of α-TCP detected. Therefore, Eq. 37 is adequately calibrated on TCP system [91].

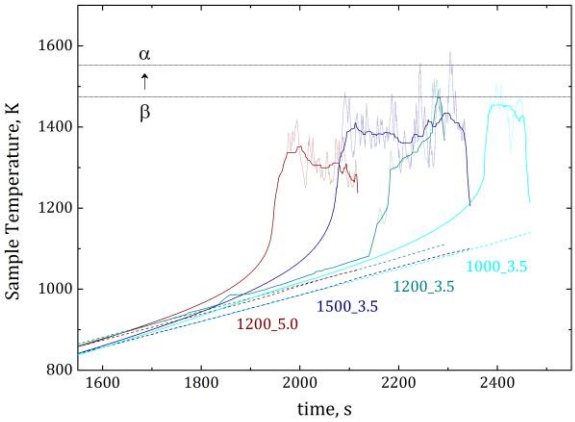

Figure III - 20. Time evolution of the sample temperature T_s according to Eq. 37, for different test conditions (E and L_0): light blue line (1000 V cm^{-1} and 3.5 mm), turquoise line (1200 V cm^{-1} and 3.5 mm), dark blue line (1500 V cm^{-1} and 3.5 mm), and dark red line (1200 V cm^{-1} and 5 mm). Horizontal dotted lines represent the temperature range of β→α transition.

Regardless such random effects, it can be noticed that the highest T_s value (1450 K) is achieved in the test performed at lower E and L_0. In other words, the minor available power is completely compensated by the higher furnace temperature at which the flash event occurs, which it clearly postponed. Moreover, if the adopted emissivity value increases from 0.8 to 1, the maximum temperature estimated by Eq. 37 is ~40 K lower.

The thermal model approach seems to be consistent for the TCP system, both in the prevision of the flash event onset temperature, and in the real sample temperature estimation. However, if the resistivity ρ_s is correlated with the estimated T_s, the resulting Arrhenius plot (Fig. III-21) shows an evident deviation from linearity, less strong than in T_f trend, but still present at the flash onset. It should be recalled that the material resistivity is not affected by the contact resistance, i.e. by the overheated anodic layer. Nevertheless, the model can not be considered completely reliable after the flash event, the reduction in the sample resistivity due to sintering and the higher conductivity of the blackened zone being ignored. As a matter of fact, if ρ_s linearity is hypothetically extended to the entire process, the extrapolated temperature

T_{extra} would increase from 1190 K to 1705 K in the last 4 s treatment, which would correspond to a heating rate of 130 K s^{-1}, quite unlikely. In conclusion, the real material behavior upon the flash event should follow an intermediate path, partial reduction and sintering accounting for the change in resistivity, although localized thermal gradient can cause re-solidified β-TCP microstructure.

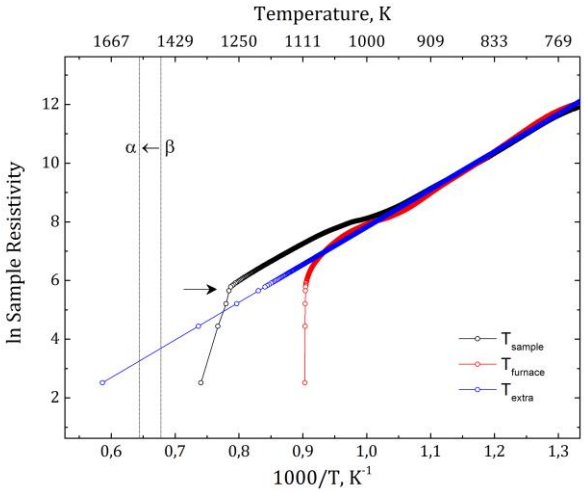

Figure III - 21. Arrhenius plot of the sample resistivity ρ_s of a representative TCP specimen (1000 V cm^{-1} and 3.5 mm) as a function of different temperature: furnace temperature T_f (red line and dots), sample temperature T_s (Eq. 37, black line and dots), and extrapolated sample temperature T_{extra} (Eq. 33, blue line and dots). Vertical dotted lines represent the temperature range of β→α transition.

3.2 Precipitation method: Magnesium doping β-TCP

3.2.1 Powder characterization

The chemical composition of nMg-TCP nanopowders, determined by ICP (Tab. III-10), is in good agreement with the nominal content of Mg, this confirming the reliability of the synthesis route here adopted. Other metal ions, such as Na^+, K^+, Ba^{2+}, and Sr^{2+}, were detected in quantity lower than 40 ppm. Positive deviations from the metal/P ratio = 3/2 is observed, which could lead to the formation of HA as minor phase upon calcination [124]. Therefore, the expected products of the chosen reaction synthesis

(Eq. 14), namely $Ca_{9-3x}Mg_{3x}(HPO_4)(PO_4)_5OH$, should be expressed more correctly by the generic formula:

$$Ca_{10-3x-z}Mg_{3x}(HPO_4)_z(PO_4)_{6-z}(OH)_{2-z} \quad (64)$$

where $0 < z < 1$ corresponds to the amount of HPO_4^{2-} groups. Therefore, Mg content expressed in mol% is equal to $300x/(10-z)$, and metal/P ratio is given by $(10-z)/6$.

	nMg0	*nMg5*
nominal Mg, mol%	0	5
Mg/(Ca+Mg), mol%	0.01 ± 0.04	4.79 ± 0.04
(Ca+Mg)/P, at. ratio	1.519 ± 0.001	1.507 ± 0.001
chemical formula	$Ca_{9.11}(HPO_4)_{0.89}(PO_4)_{5.11}(OH)_{1.11}$	$Ca_{8.61}Mg_{0.43}(HPO_4)_{0.96}(PO_4)_{5.04}(OH)_{1.04}$
MW, g mol^{-1}	954.98	944.09

Table III - 10. Magnesium content and metal/P ratio of the synthesized powders, determined by ICP-OES, proposed chemical formula and estimated molecular weight MW.

The characteristic functional groups PO_4^{3-}, HPO_4^{2-}, and OH^- were detected by FT-IR analysis (Fig. III-22) for both compositions, showing good correspondence with the values reported in literature [125]. Regardless the dopant presence, phosphate bands can be observed at 1093 and 1036 cm^{-1} (ν_3, broad), 962 cm^{-1} (ν_1), 602 and 565 cm^{-1} (ν_4, sharp), and 471 cm^{-1} (ν_2, weak); hydroxyl bands can be identified at 3570 cm^{-1} (ν stretching), and 630 cm^{-1} (δ bending). The peak description is completed by the very broad signal centered at 3427 cm^{-1}, associated to adsorbed water, and the vibration at 877 cm^{-1}, accounting for by HPO_4^{2-} groups [126]. Although the atmosphere was not controlled during the reactions, no evidence of CO_3^{2-} vibrations (1466 and 1411 cm^{-1}) can be pointed out. With respect to the differences between nMg0 and nMg5 spectra, the latter shows broadening of the phosphate ν_4 and ν_3 bands and consequent disappearance of OH signals, due to the multiplicity of the chemical environment (Ca and Mg) surrounding PO_4^{3-} groups. Moreover, a minor number of

hydroxyl groups are present in the doped structure, according to the proposed chemical formulas.

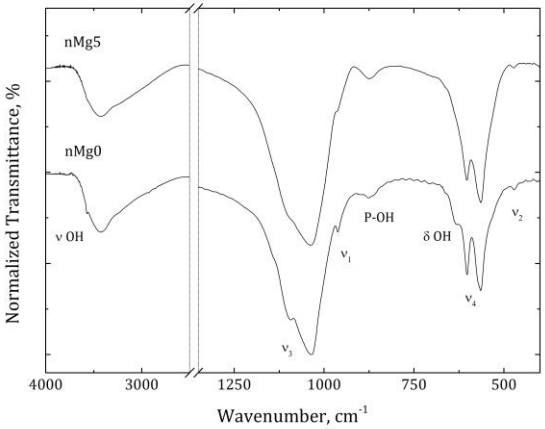

Figure III - 22. FT-IR spectra of the synthesized nMg-TCP nanopowders.

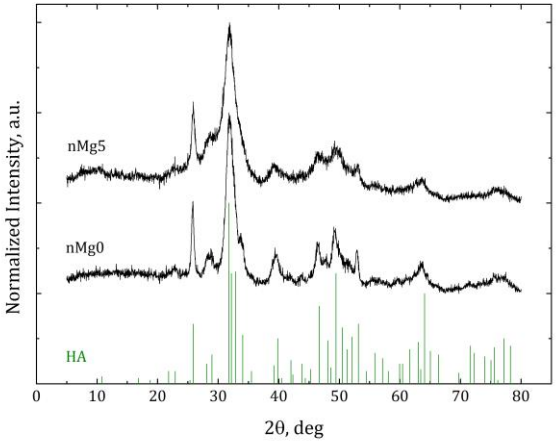

Figure III - 23. XRD patterns collected on the synthesized nMg-TCP powders. Green vertical lines represent HA (#09-0432) JCPDS reference.

XRD spectra (Fig. III-23) confirm the apatitic structure of the nanopowders; both patterns perfectly match with the HA characteristic reflections. Peaks are very broad and noisy, as expected for nanostructured and defected material, especially for the doped composition where the main peak (~31.8 deg) partially covers the minor side reflections.

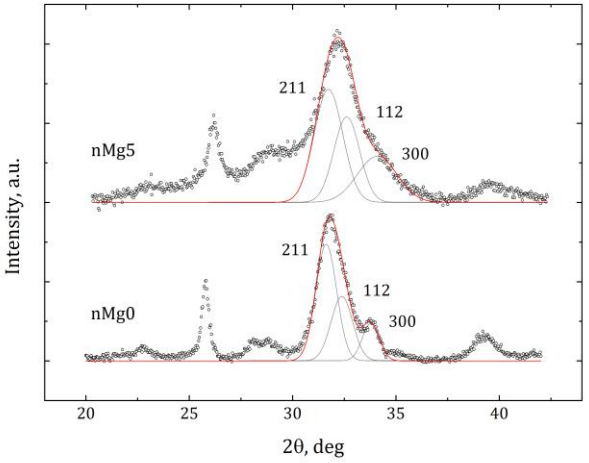

Figure III - 24. XRD profile fitting performed in the 2θ range 27-37 deg: experimental data (black circles), deconvoluted peaks (grey lines), and total fitted curve (red line).

In addition, the defected nature of CDHA lattice clearly emerges from the profile fitting analysis of the diffracted signal in the 2θ range 27-37 deg (Fig. III-24): the difference between 112 and 300 intensities is highlighted [127] and allows to calculate a crystallinity degree X_c (Eq. 8) of 26% (nMg0) and 14% (nMg5); these values agree with typical values for calcium phosphate powders synthesized by precipitation route [70].

The average extension of the coherent crystalline domains (i.e. crystallite size) are 9 nm (nMg0) and 6 nm (nMg5), respectively. The presence of secondary Me^{2+} ions seems to make the crystallization more difficult, as also observed in the present work for Mg-TCP micro-powder (Chapt. 3.1) [128] and for the Sr-HA system (Chapt. 3.3) [118]. Moreover, if compared with the spectrum of the undoped composition, very small shifts toward higher 2θ angles (~0.36 deg) affect the nMg5 diffraction peaks, this

resulting from the crystalline cell contraction [129] due to the replacement of Ca^{2+} ions by smaller Mg^{2+} ions. No other crystalline phases, like MgO or other calcium phosphates, were detected. The whole crystalline features are summarized in Tab. III-11:

Sample	*a*, 0.1 nm	*c*, 0.1 nm	*XS*, nm	X_C, %
nMg0	9.533 ± 0.002	6.889 ± 0.001	9 ± 1	26
nMg5	9.538 ± 0.004	6.877 ± 0.003	6 ± 1	14

Table III - 11. Refined unit cell parameters (*a* and *c*), crystallite sizes (*XS*) and crystalline degree (X_C) obtained by XRD, based on HA structure (JCPDS #09-0432).

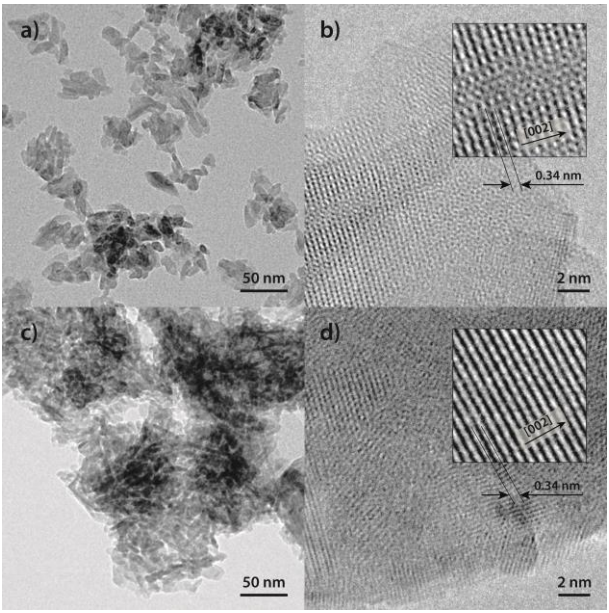

Figure III - 25. TEM images of nMg0 (a and b) and nMg5 (c and d) compositions at different magnifications. Courtesy of prof. S. Polizzi - Unive.

TEM images (Fig. III-25) of the synthesized compositions show, in both cases, particles with short nano-rods shape and narrow length distribution of 25 ± 3 nm (nMg0) and 18 ± 3 (nMg5). Mg-doped nanoparticles are slightly smaller and proportionally less elongated than pure composition, exhibiting a higher tendency to aggregate. By increasing the magnification, particles appear uniform and completely dense. No evidence of any amorphous external layer was observed [130]. Finally, the regular distance between the lattice fringes reported in the inset is equal to 0.34 nm, this being associated with the d-spacing of the apatitic (002) plane [131][132][133].

Under the hypothesis of nanoparticles with ideal rod-like shape, and taking into account the theoretical crystalline HA density (i.e. 3.14 g cm^{-3}) [134], specific surface area *SSA* was calculated by the ratio between average surfaces and volumes based on TEM measurements: values equal to 210 ± 41 m^2g^{-1} and 329 ± 33 m^2g^{-1} were obtained for nMg0 and nMg5, respectively (Tab. III-12). These values are almost twice the corresponding SSA measured by N_2 sorption, equal to 116 and 158 $m^2 g^{-1}$: this point out that particles are essentially dense and the nanorod are slightly flattened, with a nearly plate-like morphology more accentuated in nMg5 than nMg0.

As a matter of fact, the ads/des isotherms (Fig. III-26) of nMg0 composition resemble IVa-type curves, specific for meso-porous powders with small interactions (i.e. capillary condensation) between N_2 and particles. As for the hysteresis, nMg0 is characterized by H2-type loop, namely characteristic of interconnected and narrow pores. Conversely, nMg5 shows IIb-type curves with H3-type loop shape, associated with interstitial voids between aggregate of plate particles [135]. Accordingly, doped composition also shows larger total pore volume *TPV* and smaller interparticle pore dimensions (~10 nm).

Sample	*nMg0*	*nMg5*
TEM		
Ave. Length, nm	25 ± 3	18 ± 3
Ave. Diameter, nm	7 ± 2	4 ± 1
Ave. Volume, nm^3	1087 ± 525	275 ± 75
Ave. Surface, nm^2	660 ± 191	278 ± 50
Ave. SSA, $m^2 g^{-1}$	210 ± 41	329 ± 33
N_2 sorption		
SSA by BET, $m^2 g^{-1}$	116	158
TPV by BJH, $cm^3 g^{-1}$	0.402	0.493
$Ø_{ADS}$ *pore*, nm	14	12

Table III - 12. Morphology features of nMg-TCP particles, by TEM and N_2 sorption techniques.

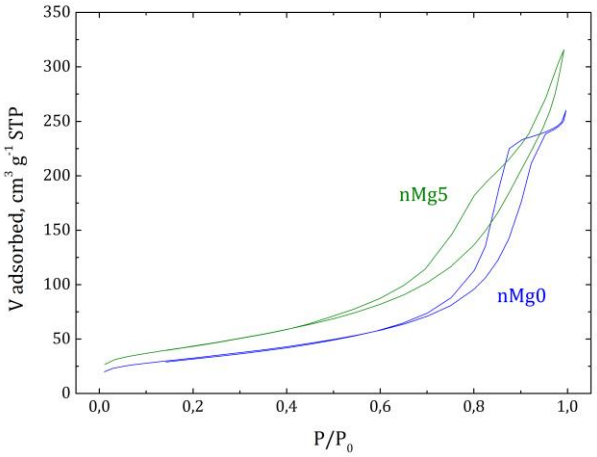

Figure III - 26. N_2 isotherms of Mg-TCP nanopowders: nMg0 (blue line), and nMg5 (green line).

The thermal behavior of synthesized Mg-TCP nanopowders is reported as TG-DTA plot in Fig. III-27. Both diagrams are characterized by a first endothermic weight loss in the 300-500 K range, simply due to adsorbed water evolution (8-10 wt%). Then, nanopowders slowly continue to release H_2O, from the protonated phosphate groups which form pyrophosphate ions as intermediate product [136]:

$$2\ HPO_4^{2-} \rightarrow P_2O_7^{4-} + H_2O \tag{65}$$

The weight loss is more evident (~2%) in nMg5, this accounting for the larger amount of adsorbed water, likely due to higher *SSA*, and the major presence of protonated phosphates HPO_4^{2-}. In addition, a small exothermal event is detected at 647 K, as a result of residual ammonium nitrate decomposition [137]:

$$NH_4NO_3 \rightarrow N_2O + 2\ H_2O \tag{66}$$

Finally, the formation of β-TCP takes place by the reaction between the pyrophosphate ions and the hydroxyl groups [110], related with the last and well defined weight loss at 1061-1114 K (nMg0):

$$P_2O_7^{4-} + 2\ OH^- \rightarrow 2\ PO_4^{3-} + H_2O \tag{67}$$

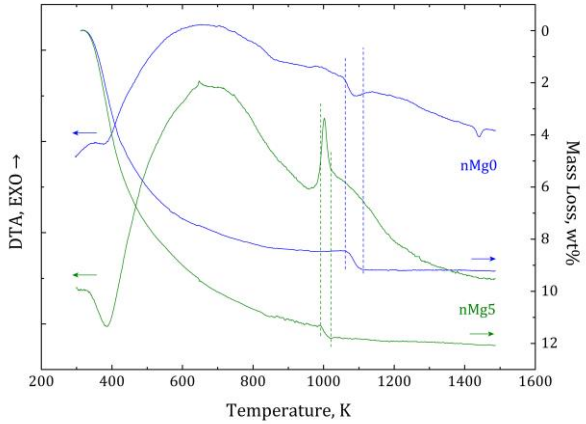

Figure III - 27. Differential Thermal Analysis (DTA, left axis) and thermogravimetry (TG, right axis) of Mg-TCP nanopowders (20 K min^{-1}): nMg0 (blue line), and nMg5 (green line). Vertical dashed lines represent the temperature range (by TG) of CDHA→β-TCP reactions.

CDHA→β	*nMg0*	*nMg5*
Thermogravimetry, 20 K min^{-1}		
Initial temperature, K	1061	992
Final temperature, K	1114	1022
Weight loss, %	0.73	0.51
Total Weight loss, %	9.21	12.08
Differential Thermal Analysis		
at 5 K min^{-1}	1045	/
at 10 K min^{-1}	1060	/
at 20 K min^{-1}	1084	/
at 40 K min^{-1}	1097	/
Kissinger fitting, Eq. 17		
Slope, K^{-1}	41428	/
Intercept	-27	/
R^2	0.977910	/
Q, kcal/mol	82	/

Table III - 13. Collected data about the thermal behavior of Mg-TCP powders: CDHA→β temperatures by TG and DTA, final weight loss and Kissinger fitting details.

Once again, the behavior of the doped composition is slightly different from pure CDHA: the transition is anticipated at 992-1022 K and its DTA signal is completely covered by a strong exothermal crystallization peak. Probably, a consistent fraction of apatitic amorphous phase was formed upon the first reaction, due to the inhibiting effect of Mg^{2+} on the crystallization. At the same time, magnesium decreases the activation energy of the second reaction, involving both crystalline and amorphous fractions in β-TCP formation.

Finally, nMg0 nanopowder show the endothermic signal of β→α-TCP transition at 1441 K, ~60 K before the corresponding Mg0 micropowder obtained by calcination, this proving the higher reactivity due to the nano-sized nature of the material. As expected, no transition was detected for the nMg5 composition up to 1470 K, the β stability field being increased by the dopant.

In summary, the two-step formation of β-TCP from CDHA for the synthesized powders is:

$$Ca_{10-3x-z}Mg_{3x}(HPO_4)_z(PO_4)_{6-z}(OH)_{2-z}$$

$$\downarrow -\frac{z}{2}H_2O$$

$$Ca_{10-3x-z}Mg_{3x}(P_2O_7)_{z/2}(PO_4)_{6-z}(OH)_{2-z}$$

$$\downarrow -\frac{z}{2}H_2O$$

$$Ca_{10-3x-z}Mg_{3x}(PO_4)_6(OH)_{2-2z}$$

$$\downarrow$$

$$3z\ Ca_{3-x}Mg_x(PO_4)_2 + (1-z)\ Ca_{10-3x}Mg_{3x}(PO_4)_6(OH)_2 \quad (68)$$

In other words, one molecule of Mg-CDHA precursor produces 3*z* Mg-TCP and 1−*z* Mg-HA. In this way, is quite evident that the crystalline composition of the final calcium phosphate, i.e. the Ca/P ratio of the precursor, is strictly dependent on the initial amount of HPO_4^{2-} groups, and consequently from the synthesis pH, rather than the Ca/P ratio of the mixed reagents [138][77].

Completely analogue results could be achieved by the level rule application on the CaO-P_2O_5-H_2O equilibrium diagram. Specifically, nMg0 and nMg5 should produce 3.96 mol% (12 wt%) and 1.37 mol% (4 wt%) of Mg-HA as secondary phase.

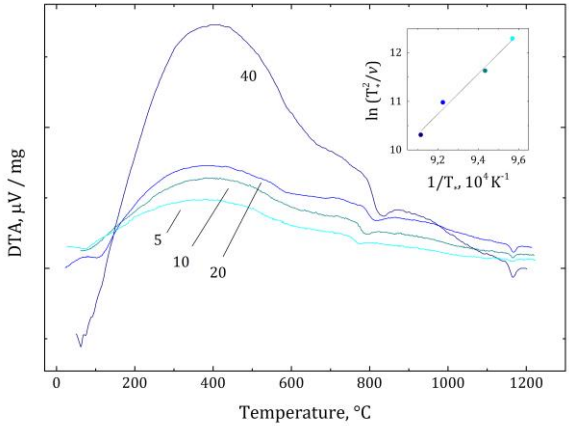

Figure III - 28. DTA curves of nMg0 composition, carried out at different constant heating rate, and corresponding Kissinger plot: light blue dots (5 K min^{-1}), turquoise dots (10 K min^{-1}), blue dots (20 K min^{-1}), and dark blue dots (40 K min^{-1}).

The kinetic of CDHA→β-TCP process for the undoped composition was further investigated by isochronal DTA approach (Fig. III-28). By using Kissinger equation (Eq. 17), linear fitting of the identified peak temperatures allows to calculate an activation energy of 82 kcal/mol, in perfect agreement with the value reported in the literature [42]. The whole set of TG-DTA data are reported in Tab. III-13.

The validity of the proposed reaction mechanism was tested for both compositions, by two heating treatments (20 °C min^{-1}) up to 730 and 750°C, followed by air quenching. All XRD spectra (Fig. III-29) match β-TCP reference lines; only nMg0, after calcination at 730°C, still shows the broad signal of CDHA. As expected, in the absence of doping the reaction requires higher temperature / time to completely occur. Moreover, the refined grain sizes are 102 ± 6 nm (nMg0) and 158 ± 7 nm (nMg5): once β-TCP is formed, magnesium promotes grain growth (Tab. III-14). No crystalline HA signals are detected in significant intensity, and therefore the slight Ca/P excess was completely accommodated by the TCP lattice.

Therefore, the obtained β-TCP powders can be more easily expressed by the general formula $Ca_{3-x}Mg_x(PO_4)_2$, where Mg mol% content is equal to *x*/0.03.

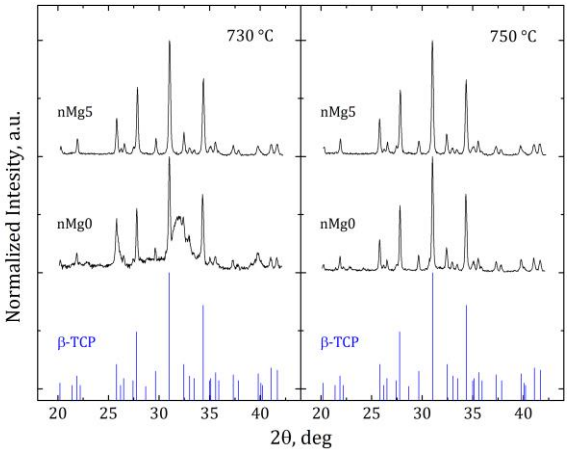

Figure III - 29. XRD patterns collected on the nMg-TCP powders, calcinated at 730°c (left) and 750°C (right). Blue vertical lines represent β-TCP (#09-0169) JCPDS reference.

Sample	*XS*, nm	*Formula*	*MW*, g mol^{-1}
nMg0	102 ± 6	$Ca_3(PO_4)_{1.97}$	307.80
nMg5	158 ± 7	$Ca_{2.86}Mg_{0.14}(PO_4)_{1.99}$	307.03

Table III - 14. Refined grain size (*XS*), proposed formula and estimated molecular weight (*MW*) of the calcined nMgTCP powders.

3.2.2 Conventional sintering

The high reactivity of nanostructured powders in terms of sintering is quite clear by observing the dilatometric plot of Fig. III-30, where nMg0 and nMg5 compositions are compared with pure TCP micropowder produced by solid-state route (i.e. Mg0). The basic idea is to convert upon sintering the CDHA precursor to dense β-TCP thus avoiding an intermediate calcination step.

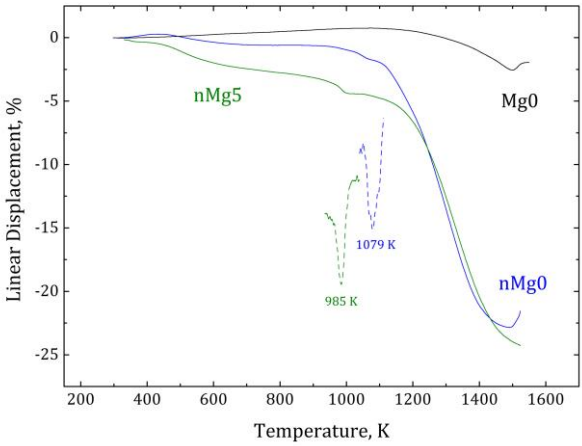

Figure III - 30. Dilatometric plot of the synthesized nMg-TCP nanopowders: blue line (nMg0), and green line (nMg5). Dashed lines represent, respectively, derivative curves near the CDHA→β-TCP transitions. For comparison, dilatometric plot of Mg0 powder (black line) is reported.

For both nanopowders, the shrinkage starts immediately as a consequence of the adsorbed water evolution and HPO_4^{2-} condensation. According to the TG-DTA data, the event is more pronounced in the doped composition. Then, CDHA→β-TCP transition occurs (easily identifiable by the derivative of the curves) and the material densification begins. The maximum shrinkage rate is basically the same (~1.2 μm s^{-1}) for both compositions; nMg0 is once again stopped by the β→α event at ~1500 K, whereas nMg5 is β-stabilized by the doping presence. In any case, large final shrinkage and densification values (86% and 91%) were achieved.

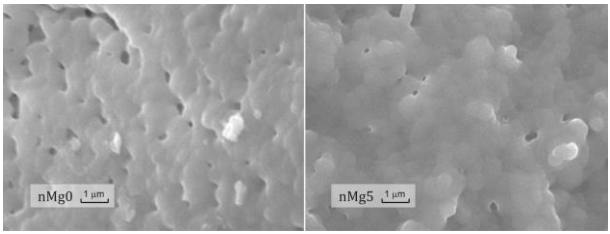

Figure III - 31. SEM images of nMg-TCP specimens subjected to conventional sintering at 10 °C min^{-1} up to 1000 °C. Bar scale is referred to 1 μm.

Similarly, conventional sintering at 10°C min^{-1} up to 1000°C was performed on nMg-TCP pellets produced by uniaxial pressing. SEM micrographs (Fig. III-31) are representative of homogeneous microstructures, characterized by residual sub-micrometric porosity, especially in nMg0, and polyhedral grains of ~500-600 nm. It must be pointed out that the sintering target temperature was limited at 1000°C to avoid the β→α transition in the undoped specimen. However, it would be possible to further optimize the treatment by introducing an isothermal step or, just for the Mg doped composition, by increasing the final temperature.

3.2.3 Isochronal flash sintering

Different flash sintering tests were performed in dilatometer at 20°C min^{-1} on circular green pellets of nMg-TCP nanopowders, as above described. In this case, the electric field was the only variable parameter, whereas sample length was assumed constant (~4.5 mm) by carefully weighing 0.2 g of nanopowder for each specimen. Compared to FS experiments carried out on TCP micropowder, the adopted length was sufficient to make the contact resistance contribution almost negligible. In addition, sample diameter was decreased from 8 to 6 mm, reducing in this way the ceramic / electrodes interface and promoting the oxygen exchange with the environment.

Fig. III-32a and b shows the linear displacement detected upon FS for nMg0 and nMg5 compositions. Conventional dilatometry (i.e. no field) is reported for comparison. Also in these cases, the onset temperature T_{on} for the flash event, i.e. the point where the material behavior deviates from the conventional shrinkage curve, is anticipated by *E*. Surprisingly, the effect is less pronounced here than in TCP micropowder (Chapt. 3.1); for instance, with the application of 1000 V cm^{-1} and 2 mA mm^{-2}, nMg0 shows the flash event at 1162 K, about 80 K above Mg0. As a matter of fact, green body resistivity should reasonably decrease with particle size, due to the larger contact area among particles, thus anticipating the condition for the flash event [139].

In any case, the shrinkage rate is much larger, with an average value of ~4 μm s^{-1}. As for the dopant influence, magnesium seems to promote the process, further decreasing the flash onset temperature (e.g. 1133 K at 1000 V cm^{-1}) and accelerating the shrinkage up to ~8 μm s^{-1}. It has to be pointed out that for the *E* here applied all flash events occur after the CDHA precursor transforms into β-TCP, and before its transition into α-TCP.

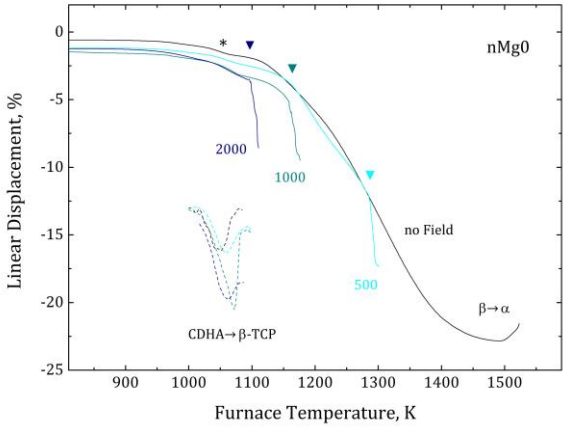

Figure III – 32a. Dilatometric plots of nMg0 under conventional (i.e. no field) and FS conditions (J_{max} = 2 mA mm^{-2}); the numbers refer to the applied electric field (in V cm^{-1}). Triangles represent the onset temperature of the flash event, while black star approximatively indicates the CDHA→β-TCP transition, determined by the first derivative of the curves (dashed lines).

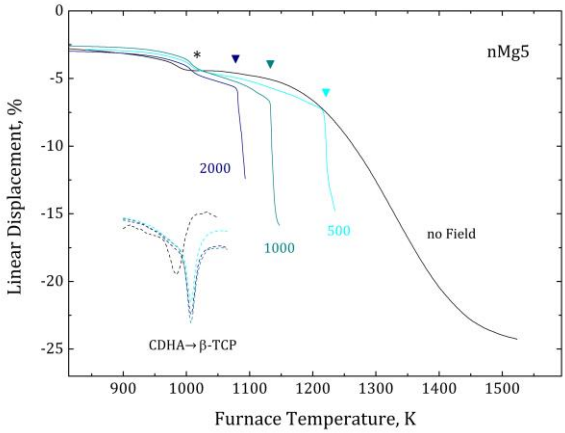

Figure III – 32b. Dilatometric plots of nMg5 under conventional (i.e. no field) and FS conditions (J_{max} = 2 mA mm^{-2}); the numbers refer to the applied electric field (in V cm^{-1}). Triangles represent the onset temperature of the flash event, while black star approximatively indicates the CDHA→β-TCP transition, determined by the first derivative of the curves (dashed lines).

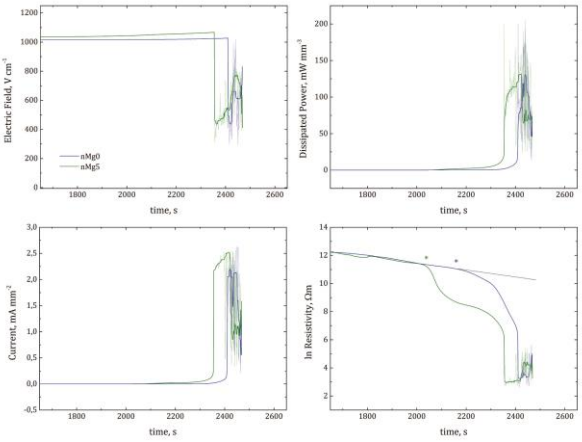

Figure III - 33. Representative example of FS tests carried out at 1000 V cm^{-1}: electric field, current, power density, and resistance as a function of the process time; nMg0 (blue lines) and nMg5 (green lines). Stars represent, respectively, CDHA→β-TCP transition.

Indeed, the evolution of the electrical features of the material as a function of time is strongly defined, before the flash event, by the crystallization of β-TCP as a new phase with completely different structure and properties with respect to the initial CDHA. Moreover, the reaction is correlated with a slight weight loss and consequent volumetric contraction, which add up to the water desorption contribution occurring up to 800 K. Therefore, being the electric field set up on the initial length L_0 of the specimens, the first stage of the FS process (i.e. voltage control) is characterized by gradually increasing E, as shown in Fig. III-33 for both compositions. Current and power follow the already described runaway-like behavior, with nMg5 reaching the flash condition ~60 s before nMg0. Then, upon FS event, the signals become very noisy, as previously observed for the plate electrode configuration.

Anyway, the most interesting trend concerns the resistivity, here reported as logarithmic plot. Before the CDHA→β-TCP transition (stars), curves show basically the same tendency; the linear regression according to the Arrhenius law (Eq. 32) leads to the thermal parameters ρ_{0s} = 45 Ωm and Q_s = 60 kJ mol^{-1} (nMg0), and ρ_{0s} = 202 Ωm and Q_s = 50 kJ mol^{-1} (nMg5). These values are quite unusual and would correspond to a resistivity of 60-80 kΩ m at 1000 K. Once the transition takes place, the slope dramatically decreases as consequence of β-TCP formation. Unfortunately, since the ionic conduction in polycrystalline solids is inhibited by the grain boundaries [140], β-crystallite growth (up to ~100 nm) leads to a not-linear reduction of the

resistivity, and this prevents the thermal parameters determination by the usual graphical linearization. For the doped composition the scenario is even more complicated, since the simultaneous exothermic crystallization event, detected by DTA, further reduces the material resistivity by supplying the reaction heat to the system. Anyway, the material resistivity at the flash event is 404 Ωm (1162 K) for nMg0, and 450 Ωm (1133 K) for nMg5.

In summary, it can be stated that:

- The temperature at which β-TCP is formed represents a lower limit for T_{on}, since CDHA is too resistive to allow a sufficient current flow through the material, at least for $E \leq 2000$ V cm^{-1};

- β-TCP resistivity, apparently, does not follow an Arrhenius-like trend due to the influence of not-linear grain growth;

- The presence of Mg seems to slightly decrease the material resistivity, leading to a more intense Joule heating (i.e. $W = E^2/\rho_s$) in the voltage-controlled step of the process, and therefore anticipating the flash onset. The effect could be related to the promoted grain growth, or to a secondary source of heat (i.e. exothermal event).

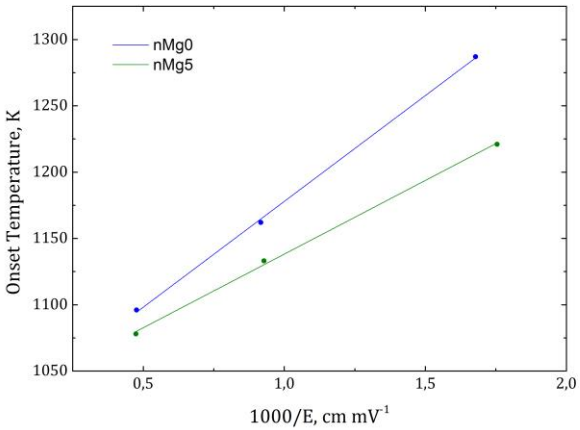

Figure III - 34. Experimental onset temperature T_{on} as a function of the inverse of the electric field E, for nMg0 (blue dots) and nMg5 (green dots) composition.

After these considerations, the quantification of the electric field influence on the overall process, in terms of onset temperature of the flash event, results quite difficult if the above thermal approach (Eq. 49) is adopted. Therefore, a semi-empirical model was proposed, trying to find the easiest relation between the experimental data for T_{on} and E. Specifically, if the electric field is determined for each test just before the corresponding flash event, thus taking into account the sample shrinkage up to these points, a simply inverse proportionality can be find (Fig. III-34), according to the equation:

$$T_{on} = a + \frac{b}{E_{on}} \tag{69}$$

where E_{on} represents the electric field at the onset point of the flash event.

Sample	E_{on}, V cm^{-1}	T_{on}, K	*a*, K	*b*, K V cm^{-1}	R^2
nMg0	596 1091 2099	1287 1162 1096	1018.35	159553	0.99973
nMg5	570 1077 2109	1221 1133 1078	1027.11	111074	0.99944

Table III - 15. Experimental data and linear fitting parameters of the flash onset temperature (T_{on}) as a function of the electric field (E_{on}).

The fitting parameters *a* and *b* are summarized in Tab. III-15 with the experimental data. Once again, the influence of Mg doping on the system is pointed out: the flash event is anticipated and less sensitive to field variations.

Conversely, sample temperature estimation (T_s), according to Eq. 37, does not require the material resistivity, but it is based on the direct measurement of *V* and *I*. Representative examples of temperature profiles are reported in Fig. III-35 for both the compositions, referred to FS treatments with E = 1000 V cm^{-1}, and 2 mA mm^{-2} of current limit (solid lines). Also in these cases, the curves show a runaway-like tendency, exceeding the β→α transition temperature determined by dilatometry (i.e. 1490 K) and scattering around ~1520 K for the entire current-control stage. The maximum temperature reached by the material could be decreased by further limiting

the current (i.e. 0.5 mA mm^{-2}, dashed line) but, at the same time, the Joule heating contribution to sintering will be lower, as well as the shrinkage rate after the flash event. In other words, a compromise between process time and amount of α-phase should be found by choosing the optimum J_{max}.

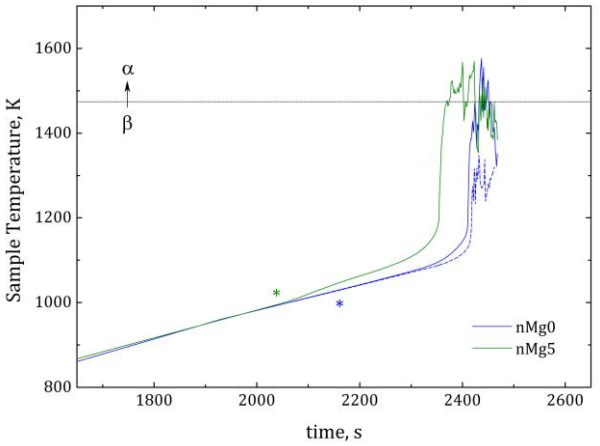

Figure III - 35. Time evolution of the sample temperature T_s according to Eq. 37, for nMg0 (blue lines) and nMg5 (green line) compositions. Tests were carried out at 1000 V cm^{-1} with different current limits J_{max}: solid lines (2 mA mm^{-2}), and dashed line (0.5 mA mm^{-2}). Horizontal dotted line represents β→α transition temperature.

Moreover, as it was previously described for TCP micropowder, higher current limits promote the blackening phenomenon at the specimen cathodic side. For what concerns nMg-TCP compositions, it was observed that extending the heating ramp for ~10 min after the current was turned off, specimens FS at 0.5 mA mm^{-2} appear completely white, whereas at 2 mA mm^{-2} a small black spot (~300 μm) is still detectable.

As a matter of fact, XRD spectra of FS specimens (Fig. III-36) processed with a current limit of 2 mA mm^{-2}, show the presence of 39 wt% of α-phase for nMg0 composition. As expected, nMg5 sample is completely constituted by β-phase, since magnesium postponed the transition temperature.

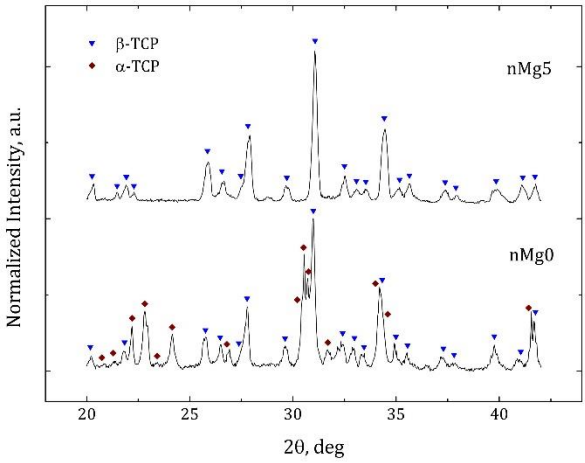

Figure III - 36. XRD patterns of nMg-TCP specimens after flash sintering (1000 V cm^{-1} and 2 mA mm^{-2}). Symbols are referred to JCPDS cards #09-0169 (β-TCP, blue triangles), and #09-0348 (α-TCP, red squares), respectively.

3.2.4 Isothermal flash sintering

The undoped composition (i.e. nMg0) was additionally subjected to isothermal flash tests carried out on dog-bone-shaped specimens. Before that, samples were subjected to pre-sintering treatment at 800°C for 30 min, in order to convert the CDHA precursor into β-TCP and to obtain an easier system to investigate. However, the following discussion and data are specifically referred to a single FS test carried out at 900°C and 7.5 mA mm^{-2} of current limit, being the comparison more convenient. In detail (Fig. III-37), electric field was gradually increased by consecutive ramps and constant steps (500 and 620 V cm^{-1}). Since the final value of ~745 V cm^{-1} was reached, flash event occurred after few seconds and a maximum in the dissipated power function was detected (~68.5 s). As usual, system control switched immediately from voltage to current, slightly decreasing the electric field to compensate the material temperature raising. After ~10 s, power supply was shut down.

The most meaningful frames of the test are collected in Fig. III-38. The difference between sample and furnace temperature, and the thermal gradients as well, can be qualitatively appreciated by the coloration assumed by the specimen.

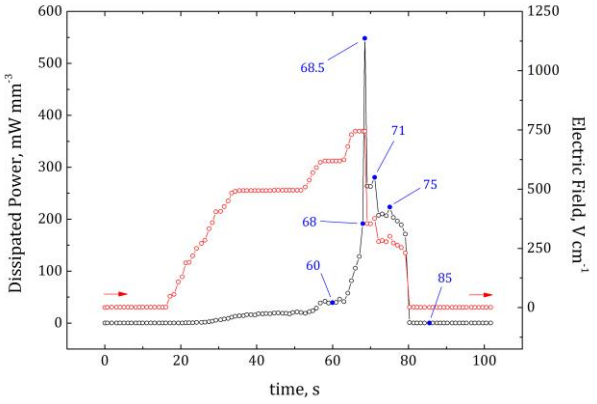

Figure III - 37. Representative example of isothermal flash sintering carried out on nMg0 composition at 900°C and 7.5 mA mm^{-2}: dissipated power (black line) and applied electric field (red line). Numbers are referred to the time (s) at which frames of Fig. III-38 were acquired.

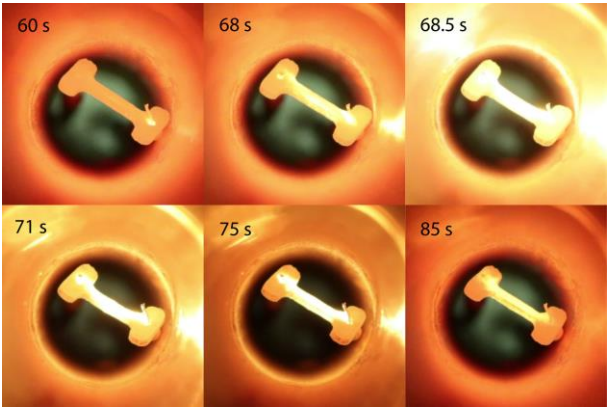

Figure III - 38. Video frames of the isothermal flash sintering test (900°C and 7.5 mA mm^{-2}) on nMg0 composition. Time values have been also reported for easier comparison with the other figures.

Initially (60 s), under the application of 620 V cm^{-1}, the flowing current is low, but sufficient to allow the identification of a brighter spot in proximity of the anodic junction, in agreement with previous observations on Mg0 micropowder (Chapt. 3.1). Then, the central portion of the dogbone becomes gradually hotter, up to the flash instant (68.5 s) at which very intense light emission occurs, combined with an almost instantaneous and asymmetric reduction of length. Anyway, few additional seconds are sufficient to make the shrinkage uniform along the entire sample, and balance the initial curvature. Finally, the last frame (85 s) proves that the material overheating, although less intense than during the current control stage, is maintained for at least five seconds since the system was switched off.

The treatment leads to an almost completely dense microstructure (Fig. III-39) with polygonal and submicrometric grains, homogeneous along the overall sample cross-section. Interestingly, the blackening phenomenon is restricted to a very narrow stripe (width ~150 μm) connecting the dogbone holes, clearly visible at different magnifications on the external surface (a and d) and identifiable as the preferential path crossed by the current.

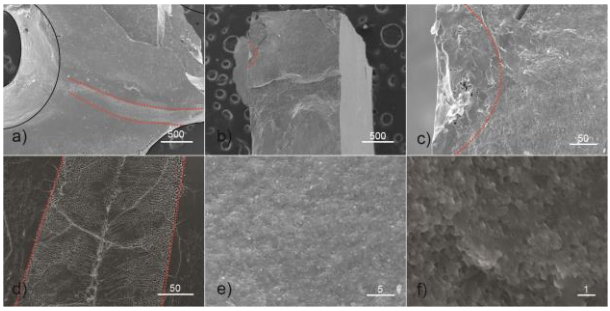

Figure III - 39. SEM images of a representative nMg0 specimen flash sintered at 900°C and 7.5 mA mm^{-2}: a) external surface of the specimen near the wire connection. Dog-bone shape (black lines) and current path (red lines) are reported for clarity; b) and c) specimen section (fracture surface); d) current path focusing on the external surface; e) and f) bulk microstructure (fracture surface). Values on the scale bars are in microns.

In this case, the typical features of a melted and slowly re-solidified material are present; starting from the center, it is possible to recognize shrinkage cavity, dendrites, intragranular cracks, equiaxial grains, and abnormal growth. However, such altered microstructure seems to present just a limited extension through the bulk material

(deep ~100 μm), being confined on the specimen skin (b and c). No remarkable differences between anodic and cathodic side were detected.

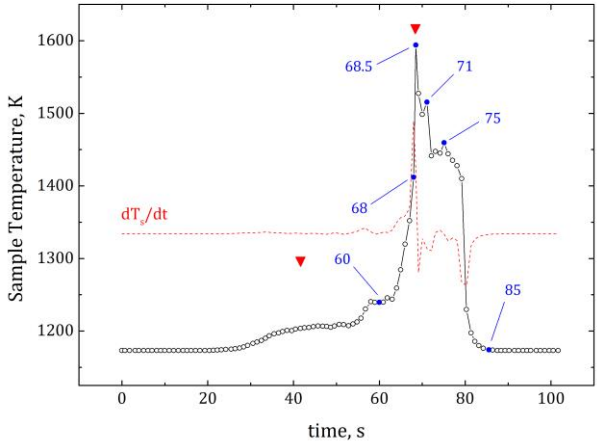

Figure III - 40. Sample temperature evolution (Eq. 51) as a function of time (black line) and its derivative (dashed red line) of nMg0 specimen flash sintered at 900°C and 7.5 mA mm^{-2}. Numbers are referred to the time (s) at which frames of Fig. III-38 were acquired; red triangles identify the linearity range of the resistivity.

Once again, Eq. 51 allows to estimate the sample temperature (Fig. III-40) during the test; the material achieved a maximum of 1594 K (for less than a second, at the flash event) and then is cooled down to ~1500 K (71 s) and ~1450 K (75 s). Shrinkage and related densification processes take place in this range, namely in 5-6 s. Anyway, it should be remembered that the model is affected by three main limitations:

- the starting sample dimensions were considered constant during the entire process. Obviously, this approximation is reasonable up to the flash event itself;

- the sample temperature was assumed uniform, at each instant, along the overall rectangular portion of the specimen. Although the core/skin gradient could be neglected due to the small sample dimensions, video frames showed asymmetries both for shrinkage (curvature) and emission (hotter anode).

- The specific heat of TCP (C_p) was considered constant during the entire process, despite of the large temperature range considered and the porosity influence.

As a matter of fact, the equation 51 would predict the thermal equilibrium between sample and furnace (T_s = T_{iso}) at 85 s, whereas the dogbone sample is still hotter. Moreover, power (and temperature) spike could have been mainly dissipated by the limited re-solidified area, accounting for the initial anisotropic shrinkage of the sample.

Despite the considered approximations, the thermal model is still well accurate to describe the material behavior at least up to the flash event, i.e. before any preferential current path or densification. Specifically, if the measured resistivity is correlated with the estimated sample temperature (Fig. III-41a and b), after an initial transient the material shows the conventional Arrhenius-like trend, characterized by an activation energy Q_s = 101 kJ mol^{-1} and a pre-exponential coefficient ρ_{0s} = 0.00533 Ω m. Conversely, the resistivity tendency with time appears quite irregular, due to the gradual increment of T_s, and the flash event is associated with the usual function drop.

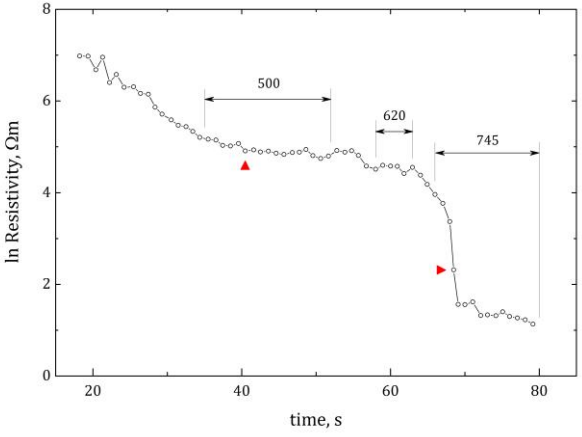

Figure III – 41a. Material resistivity as a function of time Numbers are referred to the constant field steps (V cm^{-1}); red triangles identify the linearity range of the resistivity (red line).

According to the estimated thermal parameters for resistivity, the isothermal approach described by Eqs. 56a and 56b provides the necessary conditions for the flash event at 1173 K, a critical electric field E^* of 720 V cm^{-1}, and a consequent material overheating ΔT^* of 188 K or, in other words, a sample temperature T_s^* equal to 1361 K. Such values are in good agreement with previous data, being both conditions achieved approximately 1 s before the flash event (67 s), when the sample temperature derivative abruptly increases.

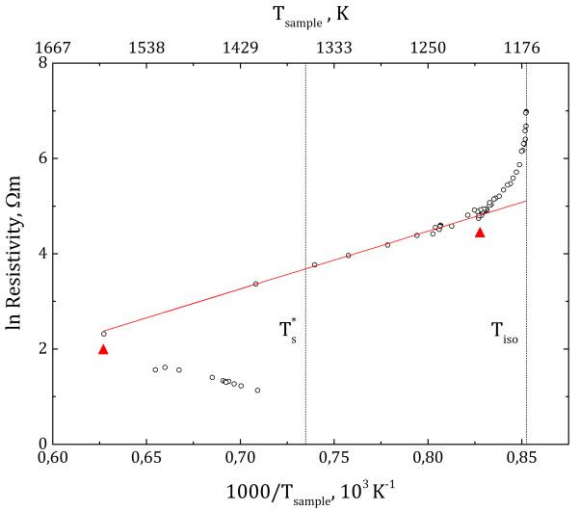

Figure III – 41b. Material resistivity as a function of sample temperature (right). Numbers are referred to the constant field steps (V cm^{-1}); red triangles identify the linearity range of the resistivity (red line).

Once the material resistivity behavior is defined by Q_s and ρ_{0s}, the isothermal model can be applied to different furnace temperature T_{iso} to calculate E^* and the corresponding sample temperature T_s^* (Fig. III-42). As expected, by increasing the furnace temperature, critical sample temperature grows almost linearly, whereas critical field exponentially decreases.

In this way, it is possible to build up a processing map (Fig. III-42), which takes into account the temperature limitations imposed by the phase transitions. Specifically, if the specimens are previously calcined or pre-sintered, CDHA→β-TCP transition (1084 K) does not constitute a lower limit for FS (orange area). Conversely, the single-step process (i.e. β-TCP conversion-and-sintering) requires a minimum isothermal

stage at 1084 K and fields in the range 695-1188 V cm^{-1}. For higher E value, the corresponding critical sample temperature would exceed β→α-TCP limit (1441 K); obviously, the same for T_{iso} (green area).

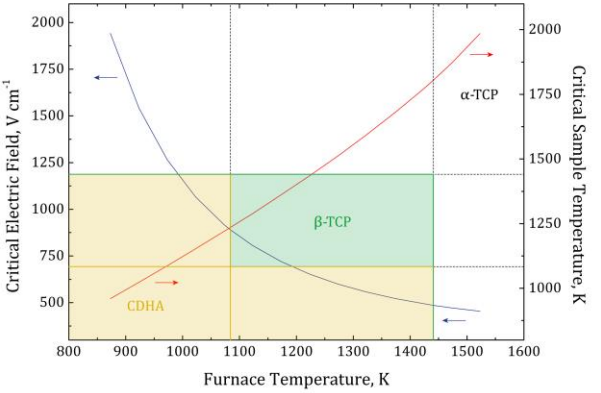

Figure III - 42. Processing map for isothermal flash sintering of nMg0 nanopowder, in terms of electric field and furnace temperature. Vertical and horizontal lines represent CDHA→β-TCP (1084 K) and β→α-TCP (1441 K) transition temperatures, determined by thermal analysis. Colored area represents the suitable range of E and T_{iso}, for as-synthesized powders (green) and for pre-calcined powders (orange).

Nevertheless, T_s^* is the critical value beyond which the system follows a thermal runaway path, and not the maximum temperature achieved by the sample, strictly dependent to the current limit. As a consequence, the real "safety zone" of the processing map should be further limited. In a much more conservative approach the maximum sample temperature T_{max} is estimated as the value at which the current limit is reached under the hypothesis of an Arrhenius-like behavior for the resistivity:

$$T_{max} = \frac{Q_s}{R_g}\left(\ln\frac{E}{\rho_{0s}\,J_{max}}\right)^{-1} \tag{70}$$

Therefore, by varying the current limit J_{max}, a family of curves can be drawn for different applied fields (Fig. III-43).

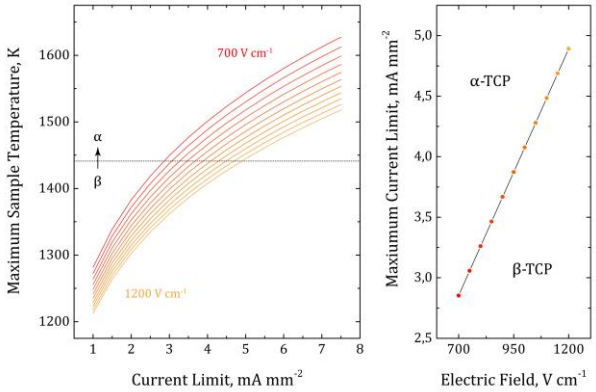

Figure III - 43. Estimated sample temperature at the flash event as a function of current limit (left), by changing the electric field (steps of 50 V cm^{-1}). β→α-TCP (1441 K) transition temperature is also indicated (dashed line). On the right, current limits at 1441 K, by varying the electric field.

Additionally, considering β→α-TCP limit at 1441 K (dashed line), a set of points defining the current limits at which the transition starts can be easily identified by the curve intersection. These points can be plotted as a function of *E* defining the straight line (i.e. $J = E/\rho_s$) between β and α-TCP stability fields. According to that, an isothermal FS treatment carried out at 1173 K and 720 V cm^{-1}, requires 2.93 mA mm^{-2} current at the most, in order to avoid any α-phase formation; by increasing the field up to 1188 V cm^{-1}, the limit is moved forward to 4.84 mA mm^{-2}.

In conclusion, it has to be pointed out that the last method could lead to excessive limitations on the process parameters, since the temperature reached by the material at the flash event ($J=J_{max}$) most likely affects only a restricted portion of the overall specimen, namely the preferential current path located on the surface.

3.3 Precipitation method: Strontium doping HA

This chapter is partially based on the published work:

Frasnelli M, Cristofaro F, Sglavo V.M, Dirè S, Callone E, Ceccato R, Bruni G, Cornaglia A.I, Visai L: Synthesis and characterization of strontium-substituted hydroxyapatite

nanoparticles for bone regeneration, Materials Science & Engineering C 71 (2017): 653-662.

3.3.1 Powder characterization

Starting from the chemical composition of nSr-HA powders, ICP-OES data (Tab. III-16) show that the real amount of Sr^{2+} in the synthesized powders is slightly lower than the nominal one. The metals-over-phosphorous atomic ratio, with respect of the stoichiometric Ca/P value of 1.667 for pure HA, appears very similar for the intermediate samples, whereas positive (+5%) or negative (−7%) deviations can be observed for the Sr poorest and richest compositions, respectively. Considering the chosen reaction synthesis (Eq. 15), the expected product should be expressed by the general formula $Ca_{10-y}Sr_y(PO_4)_6(OH)_2$, where Sr mol% is equal to y/0.1. Nevertheless, taking into account the measured amount of phosphorous and, consequently, the amount of phosphate ions, the electro-neutrality of the crystal is ensured by changing the quantity of hydroxylic groups, according to the formula:

$$Ca_{10-y}Sr_y(PO_4)_{6\pm z}(OH)_{2\mp 3z} \tag{71}$$

Essentially, the disproportion into the metals-over-phosphorous ratio is arranged by the OH^- ions. It should be pointed out that the possible presence of partially-protonated phosphate groups (e.g. HPO_4^{2-} or $H_2PO_4^-$) into the as-synthesized powders has not been considered in the proposed solution.

	nom. Sr^{2+}, mol%	*Sr/(Ca+Sr),* mol%	*(Ca+Sr)/P,* at. ratio	*Formula*	*MW,* g mol^{-1}
nSr0	0	0.0	1.743	$Ca_{10}(PO_4)_{5.74}(OH)_{2.78}$	993
nSr5	5	4.2	1.771	$Ca_{9.58}Sr_{0.42}(PO_4)_{5.65}(OH)_{3.06}$	1009
nSr10	10	7.4	1.614	$Ca_{9.26}Sr_{0.74}(PO_4)_{6.05}(OH)_{1.84}$	1042
nSr25	25	21.3	1.670	$Ca_{7.87}Sr_{2.13}(PO_4)_{5.99}(OH)_{2.04}$	1105
nSr50	50	45.2	1.652	$Ca_{5.48}Sr_{4.52}(PO_4)_{6.05}(OH)_{1.84}$	1222
nSr75	75	74.2	1.537	$Ca_{2.58}Sr_{7.42}(PO_4)_{6.50}(OH)_{0.49}$	1379
nSr100	100	100.0	1.570	$Sr_{10}(PO_4)_{6.37}(OH)_{0.89}$	1496

Table III - 16. Chemical composition of the synthesized nanopowders, determined by ICP-OES, proposed formula and estimated molecular weight MW.

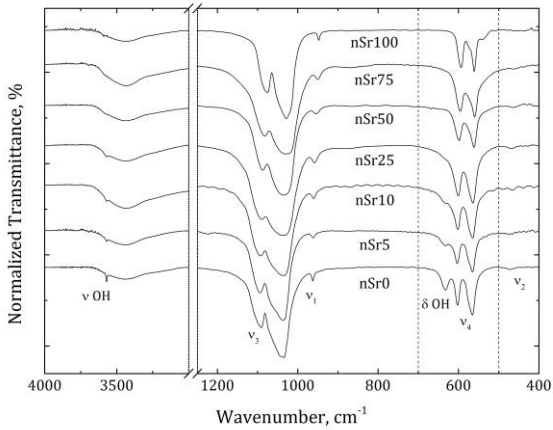

Figure III - 44. FT-IR spectra of the synthesized nSr-HA nanopowder. Vertical dashed lines are referred to the ν_4 domain (500-700 cm^{-1}) selected for the profile fitting.

The vibration bands related to PO_4^{3-} and OH^- groups detected in the FT-IR spectra (Fig. III-44), perfectly match with the values reported in literature [141]. In more detail, considering the undoped composition nSr0 (i.e. calcium hydroxyapatite), phosphate bands can be observed at 1092 and 1034 cm^{-1} (ν_3, broad), 962 cm^{-1} (ν_1), 602 and 565 cm^{-1} (ν_4, sharp), and 472 cm^{-1} (ν_2, very weak); hydroxyl bands can be found at 3572 cm^{-1} (ν stretching), and 633 cm^{-1} (δ bending). The peak description is completed by the very broad signals at 3440 cm^{-1} and 1630 cm^{-1}, associated to adsorbed water, whereas no evidence of CO_3^{2-} vibrations (1466 and 1411 cm^{-1}) can be pointed out, proving the reliability of the synthesis route avoiding apatite carbonatation. By increasing the dopant content, up to the complete $Sr^{2+} \rightarrow Ca^{2+}$ substitution (i.e. nSr100), the phosphate bands seem to shift to lower frequencies, reaching 1076 and 1028 cm^{-1} (ν_3, broad), 947 cm^{-1} (ν_1), 594 and 561 cm^{-1} (ν_4, sharp), and 463 cm^{-1} (ν_2, very weak). Conversely, OH signals maintain their positions, but gradually fade out until being almost negligible.

The effect is highlighted by investigating the FT-IR spectra in the 500-700 cm^{-1} range, corresponding to the ν_4 domain and to the OH bending vibration (Fig. III-45). According to the literature [7], deconvolution and peak integration were performed in this region, taking care to previously normalize the spectra by the ν_3 signal, by introducing six components: hydroxyls, surface phosphates [142] (HPO_x and PO_x), and three different internal phosphates PO_4^{3-} (Tab. III-17a and III-17b).

	internal PO_4^{3-} (1)		*internal PO_4^{3-} (2)*		*internal PO_4^{3-} (3)*	
	Pos., ±2 cm^{-1}	*Rel. Area,* %	*Pos.,* ±2 cm^{-1}	*Rel. Area,* %	*Pos.,* ±2 cm^{-1}	*Rel. Area,* %
nSr0	565	34.6	574	18.1	602	16.7
nSr5	564	29.1	574	18.1	603	22.6
nSr10	563	19.8	571	26.0	602	22.6
nSr25	563	34.4	573	11.4	600	30.9
nSr50	561	25.2	571	21.5	598	22.7
nSr75	559	25.5	572	12.1	595	25.5
nSr100	561	35.0	573	9.5	593	26.6

Table III - 17a. Deconvoluted signals of the FT-IR phosphate v_4 region (500-700 cm^{-1}): bulk components. Position and integrated area percentage for each component have been reported.

Focusing on the differences between nSr0 and nSr100 spectra (Fig. III-45), the latest clearly shows the HPO_x component at low frequencies, and the almost complete absence of the OH signal. More generally, by increasing the Sr amount, the sum of HPO_x and PO_x integrated areas (i.e. surface components) gradually grows.

	surface HPO_x		*surface PO_x*		*δ OH^-*	
	Pos., ±2 cm^{-1}	*Rel. Area,* %	*Pos.,* ±2 cm^{-1}	*Rel. Area,* %	*Pos.,* ±2 cm^{-1}	*Rel. Area,* %
nSr0	538	0.4	606	3.0	633	27.4
nSr5	537	8.2	616	3.7	634	18.4
nSr10	540	6.4	614	8.3	635	17.0
nSr25	538	4.2	610	5.6	633	13.6
nSr50	538	8.3	604	12.4	633	9.9
nSr75	538	17.0	603	13.8	633	6.0
nSr100	538	9.1	599	14.3	633	5.4

Table III - 17b. Deconvoluted signals of the FT-IR phosphate v_4 region (500-700 cm^{-1}): surface components. Position and integrated area percentage for each component have been reported.

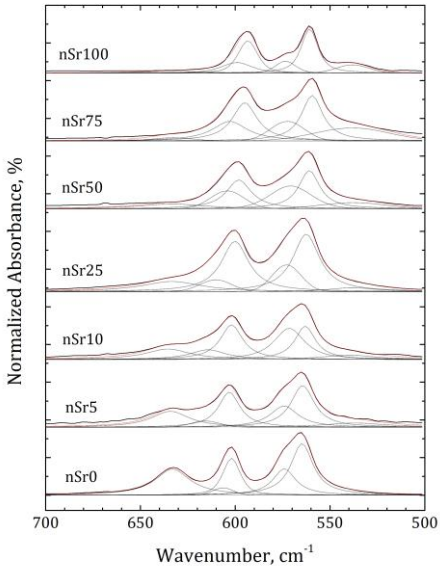

Figure III - 45. FT-IR profile fitting performed on the phosphate ν_4 region (500-700 cm^{-1}): experimental data (black line), deconvoluted peaks (grey line), and total fitted curve (red line).

Similarly, Sr^{2+} influence on the hydroxyapatite structures appears through the XRD patterns, reported in Fig III-46. For the mono-cationic compositions, i.e. nSr0 and nSr100, the quite resolved reflection perfectly fit the corresponding HA (calcium hydroxyapatite) and SrHA (strontium hydroxyapatite) references (see Tab. II-3), respectively. No others crystalline phases can be detected. Again, the intermediate compositions show a transitional behavior, with the peaks gradually broadening and shifting to lower angles, and a qualitative increase of the noise.

Therefore, it can be stated that the simultaneous presence of Sr^{2+} and Ca^{2+} has been completely arranged by the hydroxyapatite lattice by forming a single-phase, which appears progressively more defected and nanocrystalline, as it can be confirmed by the calculated crystallite size (XS) reported in Tab. III-18. For instance, the extension of the coherent crystalline domains is 52 nm (nSr0), 19 nm (nSr10) and 41 nm (nSr100).

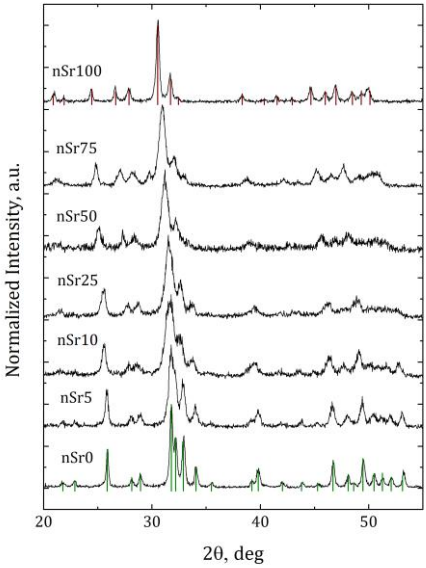

Figure III - 46. XRD patterns collected on the synthesized nSr-HA powders. Green and red vertical lines represent, respectively, HA (#09-0432) and SrHA (#33-1348) JCPDS references.

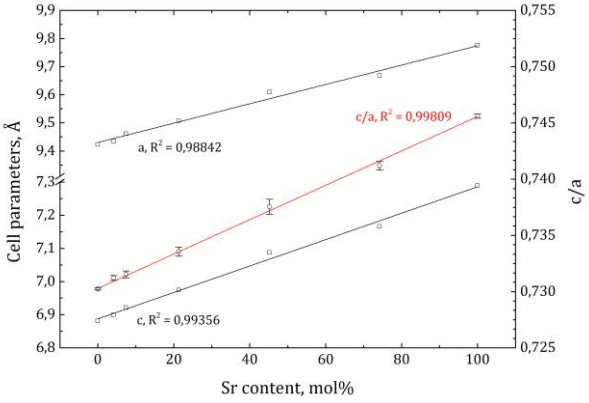

Figure III - 47. Linear interpolation of the refined cell parameters (by XRD) as a function of the real Sr amount (by ICP): *a* and *c* (black line), *c/a* ratio (red line). R^2 values have been also reported.

Conversely, the refined cell parameters *a* and *c*, as well their ratio *c/a* (Fig. III-47), both show a linear increment in dimension, explicable with the higher ionic radius of Sr (0.113 nm) respect to Ca (0.099 nm) [132]. In other words, the crystalline cell gradually grows by extending mainly the *c* dimension (z axis) than the basal one *a* (xy plane). From these data, it is possible to calculate the real density ρ of the powders by:

$$\rho = \frac{Z\ MW/2}{V_{cell}\ N_A} = \frac{Z\ MW/2}{a^2 c\ \sin(\pi/3)\ N_A} \tag{72}$$

where V_{cell} is the volume of the unit-cell considering the trigonal structure of hydroxyapatite, *Z* the number of atoms contained in the unit cell (equal to 2), and N_A the Avogadro number ($6.022 \cdot 10^{23}$ mol^{-1}). *MW* is the molecular weight, based on the ICP chemical composition of each powder (Tab. III-16), which needs to be divided by 2 since the considered formula is formed by two unit-cells. The obtained values are slightly larger (+ 1-8%) than the corresponding values extrapolated from the crystallographic densities ρ_{cry} of stoichiometric HA and SrHA (Tab. III-18). Most likely, *MW* values were overestimated by considering only PO_4^{3-} groups and disregarding HPO_x and PO_x surface species, as demonstrated by FT-IR.

Sample	*a*, Å	*c*, Å	*c/a*, ± 0.001	*XS*, ± 1 nm	ρ, ± 0.01 g/cm^3	ρ_{cry}, ± 0.01 g/cm^3
nSr0	9.423 ± 0.001	6.881 ± 0.001	0.730	52	3.12	3.08
nSr5	9.435 ± 0.003	6.899 ± 0.002	0.731	31	3.15	3.11
nSr10	9.461 ± 0.004	6.921 ± 0.003	0.732	19	3.22	3.14
nSr25	9.507 ± 0.005	6.974 ± 0.004	0.734	30	3.36	3.24
nSr50	9.609 ± 0.008	7.087 ± 0.007	0.738	25	3.58	3.42
nSr75	9.668 ± 0.005	7.166 ± 0.004	0.741	19	3.95	3.64
nSr100	9.776 ± 0.002	7.289 ± 0.002	0.746	41	4.12	3.84

Table III - 18. Refined unit cell parameters (*a* and *c*), crystallite sizes (*XS*) and real density (ρ) obtained by XRD. For comparison, crystallographic densities (ρ_{cry}) have been extrapolated from the values of stoichiometric HA and SrHA.

Fig. III-48 shows representative SEM and TEM image of the synthesized nanopowders. Particles exhibit a rod-like shape, with growing tendency to aggregation increasing the Sr amount. At the same time, the major axis of the particles significantly

increases, moving from 45 nm (nSr0) to 124 nm (nSr100) and showing an elongated morphology. Most likely, strontium presence decreases the surface energy γ_S of the apatite crystals, promoting both the particle growth and the grain boundary formation (i.e. larger number of smaller crystallites) during the synthesis reaction.

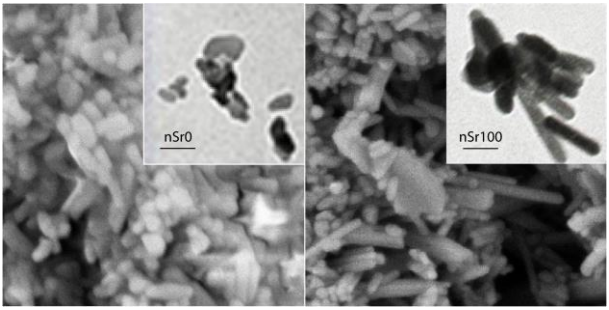

Figure III - 48. Representative SEM and TEM images of nSr0 and nSr100 compositions. Bar scale into the inserts are both referred to 100 nm.

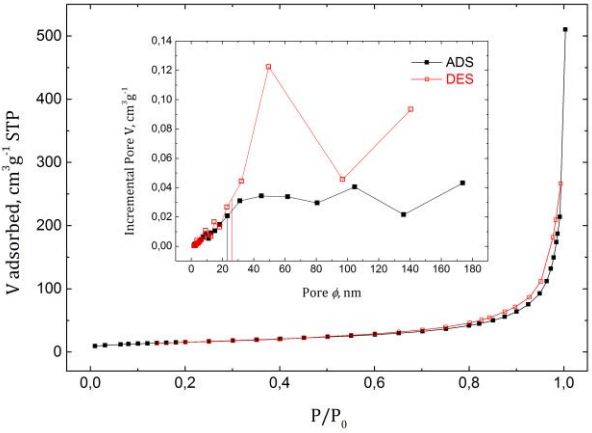

Figure III - 49. N_2 isotherms and pore size distribution (insert) of nSr50 nanopowder: adsorption data (black square and line), and desorption data (red square and line). In the insert, vertical lines represent the average pore diameter Ø under adsorption (black) and desorption (red) conditions.

Also N_2 sorption results (Fig. III-49) are in good agreement with the previous considerations. All samples show IIb-type isotherms with H3 hysteresis loop and no plateau at high pressures, this being representative of meso – macro porous powder aggregates.

Specific Surface Area and average pore diameters are randomly scattered around 50 $m^2 g^{-1}$ and 30 nm, respectively (Tab. III-19). By using Eq. 16, *SSA* can be related with particle dimension *D* measured by TEM, and the real density ρ computed by XRD spectra refinements, to calculate the geometrical parameter ψ, i.e. the adimensional ratio between particle length and diameter. Considering the wide size distributions, and the elongated morphology of powders as well, ψ values are quite reasonable and prove that the nanoparticles are completely dense. Therefore, the measured porosity is likely due to the interparticle voids within the aggregates.

	TEM	*BET*	*BJH*			*Eq. 16*
Sample	D, nm	*SSA*, $m^2 g^{-1}$	*Total Pore Volume*, $cm^3 g^{-1}$	$Ø_{ADS}$ *pore*, nm	$Ø_{DES}$ *pore*, nm	ψ
nSr0	45 ± 14	34	0.324	39	55	5 ± 1
nSr5	72 ± 15	47	0.308	27	38	11 ± 2
nSr10	83 ± 24	61	0.396	26	29	16 ± 5
nSr25	98 ± 17	35	0.170	19	20	12 ± 2
nSr50	113 ± 32	56	0.331	23	26	23 ± 6
nSr75	121 ± 22	53	0.262	17	21	25 ± 5
nSr100	124 ± 42	33	0.285	36	47	17 ± 6

Table III - 19. Particle length *D* (by TEM), *SSA* and pore distribution (by N_2 sorption), and geometrical parameters ψ.

Finally, the powder characterization was completed with the study of the local environment of phosphorous and hydrogen atoms in the apatitic structure, as reported for the representative composition (nSr50) in Fig. III-50.

^1H MAS spectra show the broad water peak at 5-7 ppm and, in some cases, a variable number of small signals (1-3 ppm) very likely due to surface adsorbed water [143]. The most meaningful output is the sharp peak at -0.21 ppm (nSr50) assigned to the apatitic hydroxyl resonance [144].

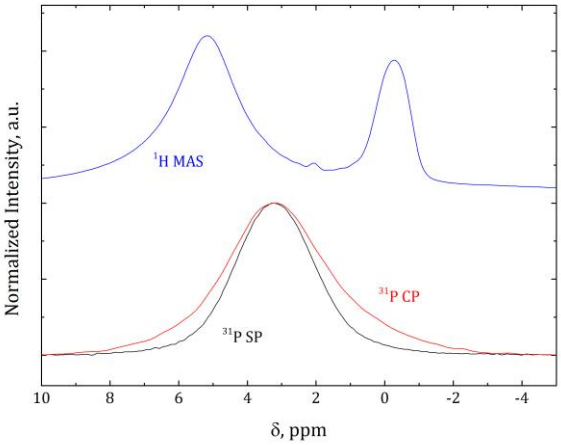

Figure III - 50. Representative solid-state NMR spectra (nSr50 composition): ^{1}H MAS (blue line), ^{31}P CP-MAS (red line) and ^{31}P SP-MAS (black line).

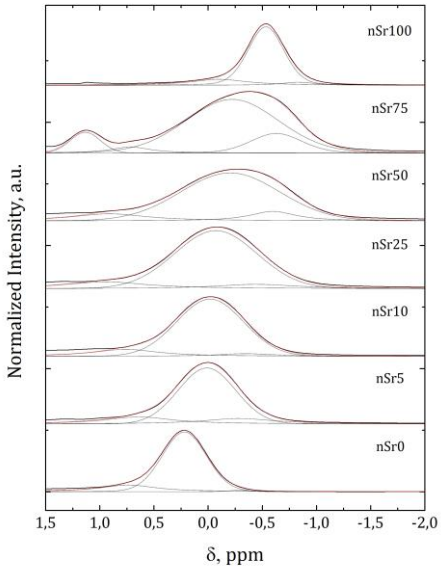

Figure III - 51. ^{1}H MAS profile fitting performed on the -2.0–1.5 ppm region: experimental data (black line), deconvoluted peaks (grey line), and total fitted curve (red line).

By observing the complete nSr-HA series (Fig. III-51), the effect of Sr amount is clearly pointed out by shift to higher fields (from 0.22 to -0.53 ppm) and enhanced asymmetry of the crystalline OH resonance. Deconvolution and peak integration in the region -2.0-1.5 ppm was performed to quantify such differences, by adopting a central main component (crystalline OH), and two additional species S_1 and S_2 to fit the peak sides. Since the spectra exhibit poorly resolved peaks, especially for the central compositions, signal elaboration was carried out by initially fixing the main component position at the corresponding peak maximum, and systematically refining the other features one at a time (position of the side components, widths and intensities). Eventually, a last computational cycle was performed by unlocking all previous bounds. The integrated area of the crystalline OH component (Tab. III-20) gradually decreases despite of the observed broadening. Once more, the complete $Sr^{2+} \rightarrow Ca^{2+}$ replacement leads to reverse this trend, with the narrowing of the OH peak. Unfortunately, no clear trend for the S_1 and S_2 components was found, not allowing any further discussion.

	S_1			*crystalline OH*			*S_2*		
Sample	*δ*, ±0.05 ppm	*FWHM*, ±15 Hz	*Rel. Area*, %	*δ*, ±0.05 ppm	*FWHM*, ±15 Hz	*Rel. Area*, %	*δ*, ±0.05 ppm	*FWHM*, ±15 Hz	*Rel. Area*, %
nSr0	-0.29	70	1.3	0.22	144	81.7	0.73	187	17.1
nSr5	-0.28	243	13.3	0.01	187	70.7	0.64	227	16.0
nSr10	-0.35	188	4.8	-0.02	218	80.8	0.76	216	14.4
nSr25	-0.44	265	8.3	-0.07	268	77.8	0.95	278	13.9
nSr50	-0.60	152	10.1	-0.21	322	77.0	0.91	250	12.9
nSr75	-0.63	167	16.6	-0.22	302	78.0	0.71	130	5.5
nSr100	-0.83	115	5.5	-0.53	117	76.9	-0.10	193	17.6

Table III - 20. Deconvolution of the OH signal in the ^{1}H MAS NMR spectral region -2.0–1.5 ppm. Position, broadening (as Full Width at Half Maximum) and integrated area percentage for each component have been reported.

The ^{31}P NMR spectra (Fig. III-50) reveal a single peak at 3.21 ppm (nSr50), associated to the phosphate PO_4^{3-} environment. However, by running the analyses under cross-polarized conditions (^{31}P CP-MAS), the signal appears more asymmetric, and two lateral components are clearly detectable below the main peak. Since this specific pulse program emphasizes the response of ^{31}P nuclei close to ^{1}H atoms, the minor components can be identified as partially-protonated phosphate groups, namely $-PO_x$ and $-HPO_x$ [145], placed on the particle surfaces.

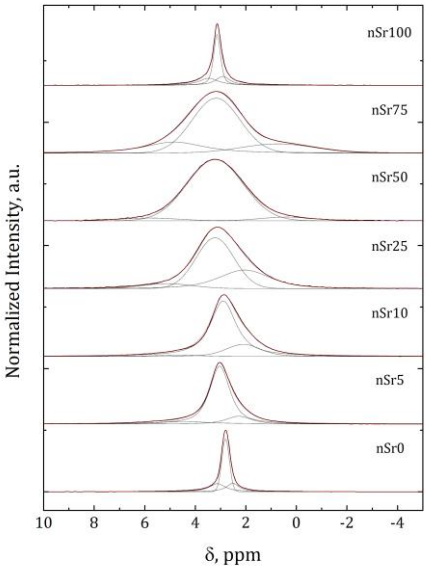

Figure III - 52. ^{31}P SP MAS profile fitting performed on the -5.0–10.0 ppm region: experimental data (black line), deconvoluted peaks (grey line), and total fitted curve (red line).

	surface PO_x			*internal PO_4^{3-}*			*surface HPO_x*		
Sample	*δ*, ±0.05 ppm	*FWHM*, ±6 Hz	*Rel. Area*, %	*δ*, ±0.05 ppm	*FWHM*, ±6 Hz	*Rel. Area*, %	*δ*, ±0.05 ppm	*FWHM*, ±6 Hz	*Rel. Area*, %
nSr0	3.13	93	25.8	2.80	43	53.0	2.51	74	21.2
nSr5	4.48	300	9.4	3.03	116	77.7	2.27	146	12.9
nSr10	4.71	222	1.9	2.89	148	79.9	2.10	193	18.2
nSr25	5.13	291	7.5	3.22	214	57.4	2.05	290	35.1
nSr50	5.82	331	4.3	3.21	316	90.5	0.39	296	5.2
nSr75	4.83	338	21.2	3.17	270	62.6	0.72	417	16.2
nSr100	3.46	111	24.5	3.14	39	52.7	2.91	82	22.8

Table III - 21. Deconvolution of ^{31}P SP-MAS NMR spectra in the range -5.0–10.0 ppm. Position, broadening (as Full Width at Half Maximum) and integrated area percentage for each component have been reported.

Therefore, ^{31}P SP-MAS spectra deconvolution was performed by adopting three components: a central main component (internal PO_4^{3-}), and two additional species -PO_x and -HPO_x to fit the peak sides (Tab. III-21).

Similarly to FT-IR and XRD, the main signal (Fig. III-52) gradually broadens and shifts to lower fields up to nSr50 composition. Beyond this value, trends are inverted: internal phosphate peak moves toward high fields and an abrupt decrease of linewidth occurs for the fully substituted nSr100 composition. Unfortunately, minor components seem to follow no regular trends with Sr amount.

3.3.2 Data comparison

Complementary analytical techniques, such as TEM, XRD, FT-IR and NMR, allowed to investigate the effect of $Sr^{2+} \rightarrow Ca^{2+}$ replacement under different points of view. In addition, by comparing data from various sources, additional considerations can be drawn. As discussed above, strontium causes a gradually reduction of the crystal surface energy γ_s of hydroxyapatite, leading to more elongated particles (i.e. higher ψ factors), smaller crystallite size *XS*, and an anisotropic expansion of the unit cell, being *c* axis more affected than *a* direction. Although *c/a* ratio linearly changes with the dopant content, the consequence on the final particle size appears relevant for limited Sr amounts, whereas it is more attenuated for larger Sr quantities (Fig. III-53).

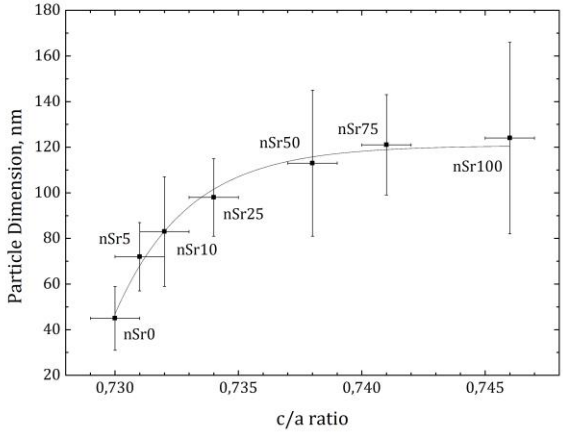

Figure III - 53. Particle dimension *D* (by TEM), as a function of *c/a* ratio (by XRD refinement), by increasing the Sr amount.

Further indications of the radical modifications induced by the cationic replacement can be deduced from FT-IR and NMR spectra, since both analytical techniques are extremely sensitive to the local chemical environment changes. The deconvolution of phosphate ν_4, ^{31}P SP-MAS, and ^{1}H MAS signals allowed to prove the existence of partially-protonated PO_x and -HPO_x surface groups, which qualitatively grow with the Sr content and the particle dimension. Moreover, clear trends about internal PO_4^{3-} and crystalline OH groups were identified by removing the contribution of the minor side species. By plotting the integrated area of FT-IR δ OH peaks vs. the refined *c/a* ratio (Fig. III-54), an inverse-proportional dependency is obtained. In other words, the preferential elongation of crystalline cell along the *c* axis induced a decrease of probability of allowed OH vibrations. If the crystalline structure of hydroxyapatite is considered, hydroxyl groups are embedded within planar triangle sites [58] formed by Me^{2+} ions (M(2) type), and oriented along the *c* axis. By increasing the Sr amount, and correspondingly the *c* parameters, the spatial density of O-H bonds decreases, as well as the related FT-IR signal intensity. In addition, the progressive presence of strontium (electron configuration [Kr] $5s^2$) instead of calcium (electron configuration [Ar] $4s^2$) into the M(2) sites, leads to higher electron densities around the hydroxylic groups (i.e. more shielded protons), thus inducing the observed upfield-shift of the OH component in ^{1}H MAS spectra.

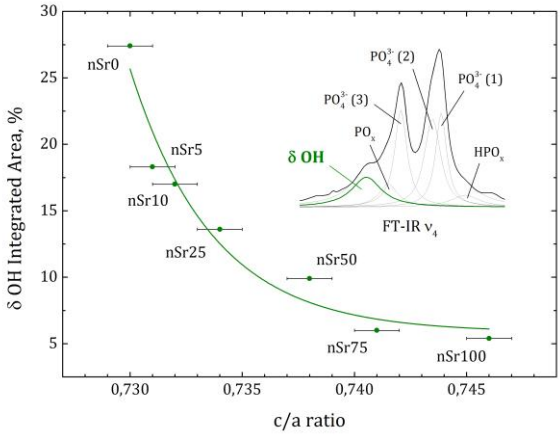

Figure III - 54. δ OH relative area (by FT-IR deconvolution), as a function of *c/a* ratio (by XRD refinement), by increasing the Sr amount.

Conversely, the vibrational frequency decrease of v_4 phosphate components (1) and (3), and the downfield-shifts of the internal PO_4^{3-} signals in ^{31}P SP-MAS spectra are due to the increment of the reciprocal distance between phosphate groups upon the lattice expansion, leading to the energy loss of some P-O bonds [146].

Further considerations can be drawn by plotting the linewidth of the internal PO_4^{3-} and crystalline OH deconvoluted signals, as a function of the Sr amount determined by ICP (Fig. III-55). Recalling that in NMR analysis line broadening is associated with the multiplicity of chemical species surrounding a specific nucleus (i.e. ^1H and ^{31}P, in this case), nSr50 composition is quite clearly the most disordered structure, where both Me^{2+} ions are perceived as point defects, being in equal number. Nevertheless, all nanopowders exhibit just one and homogeneous crystalline phase, gradually evolving between the two limit compositions nSr0 and nSr100. The latter composition appears coherently ordered and easier to crystallize (i.e. higher *XS*).

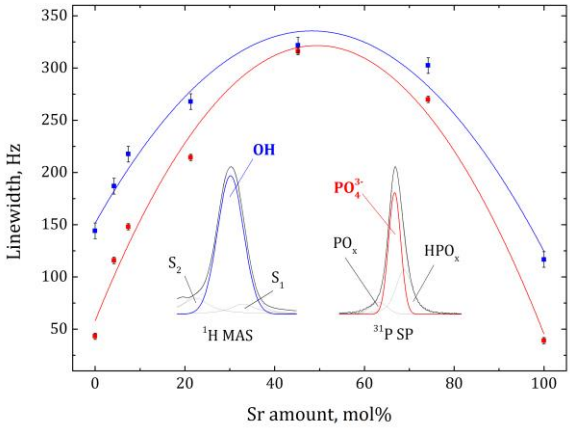

Figure III - 55. Linewidth (FWHM) of the central components of the deconvoluted NMR signals, as a function of Sr amount: crystalline OH (by ^1H MAS, blue line), and internal PO_4^{3-} (by ^{31}P SP-MAS, red line).

Finally, for nSrHA the properties are strictly related with the surface of the nanoparticles; no apparent regular trends were found as a function of dopant amount, or by comparing results from different techniques. In particular, *SSA* and HPO_x / PO_x deconvoluted components from FT-IR or NMR spectra seem to vary randomly, regardless the Sr content within the apatite lattice. It has to be considered that natural

or synthetic apatites are actually characterized by the presence of an amorphous hydrated layer on their surfaces [147], where the partially-protonated phosphate groups are mainly located, and thus forced to interact with the adsorbed water. Therefore, a more complete investigation of such surface features should be realized by previously removing the random contribution of water, for instance by drying the synthesized nanopowders before their characterization.

Chapter IV

Conclusions

4.1 Solid state reaction: Magnesium doping β-TCP

Magnesium-doped TCP powders with micrometric size were successfully produced by solid state synthesis, resulting in a monophasic β-phase able to completely accommodate the dopant presence (from 0 to 2 mol% Mg^{2+}). With respect to pure TCP, the partial substitution of Ca^{2+} by Mg^{2+} leads to a structural stabilization of the β lattice and to a consequent increment of the β→α activation energy, up to 420 kcal mol^{-1} for 2 mol% Mg^{2+} content. Therefore, the transition into the α phase is postponed upon heating, and a much higher densification level (85%) can be achieved by conventional sintering in spite of the poor reactivity of the starting powders, with better mechanical properties (hardness and flexural strength). At the same time, it is shown that magnesium promotes the α→β kinetic reconversion upon cooling, further limiting the presence of retained α-phase into the sintered TCP. Residual stresses due to the coexistence of both β and α polymorphs in similar amount (~50:50) were quantified as ~10 MPa.

Annealing treatment at ~750°C, performed on sintered TCP bodies to reconvert the possible metastable α-phase, was demonstrated to be effective only for the doped composition, since magnesium promotes β-formation both from the kinetic and thermodynamic points of view. With 1 mol% Mg^{2+}, the activation energy for the reconversion process was 66 kcal mol^{-1}.

Un-doped β-TCP was subjected to several tests under flash sintering configuration. The treatments were successfully realized on cylindrical green pellets at constant heating rate, and a dense microstructure was achieved at temperature lower than 1000°C in just 10 min (1500 V cm^{-1}, 2 mA mm^{-2}), thus avoiding any expansion related to β→α transition. The phenomenon seems to be triggered by the combination of Joule effect and Negative Thermal Coefficient for electrical resistivity, which induce a thermal runaway mechanism.

For the considered system, a simplified thermal-based model well describes the entire process: the flash onset can be accurately predicted as a function of the process parameters and the real temperature reached by the material can be estimated, as well. The flash event (i.e. the point where an abrupt resistivity drop and density

increase are observed) is anticipated, in terms of time and furnace temperature, by higher electric field and longer specimens (> 4 mm), whereas the maximum current influences the real temperature reached by the materials and, consequently, the shrinkage rate. As a matter of fact, current density higher than ~2 mA mm^{-2} can lead, for the considered geometry, to the gradual formation of α-phase in the final β-TCP sintered samples.

The present investigation pointed out that the use of planar electrodes and cylindrical specimens limits the oxygen exchange at the material/electrode interface. As direct consequences, the anodic surface develops an additional resistance contribution, predominant for specimens shorter than 3-4 mm, while at the cathodic side the partial reduction of the phosphate groups can occur, this resulting in a limited blackened area. Such secondary reaction mainly occurs upon the flash and it is proportional to the duration and the current intensity: the current flow can be channeled into the blackened area, locally leading to higher temperature gradient (~130 K s^{-1}) for few seconds and even to liquid phase formation.

In conclusion, it was shown that flash sintering represents a reliable consolidation technique for producing β-TCP ceramics starting from micrometric powders, sensibly reducing time and temperature of the process.

4.2 Precipitation method: Magnesium doping β-TCP

Magnesium-doped TCP nanopowders (0 and 5 mol% Mg^{2+}) were successfully produced by precipitation from aqueous solutions; highly-defected and nanostructured CDHA plate-like particles (~20 nm) with Ca/P ratio equal to 1.5 were obtained as first reaction product.

Also in this case, the Mg^{2+} presence in the apatitic lattice strongly influences the system: with respect to un-doped CDHA, crystalline cell is slightly contracted and its crystallization from the mother liquor is inhibited. As a consequence, thermal conversion into β-TCP is preceded by an intense exothermal event, and anticipated by ~50°C.

The powders were shown to be highly reactive when subjected to conventional conversion-and-sintering treatments at 10°C min^{-1} up to 1000°C and dense (~90%) β-TCP microstructures with final 500-600 nm grain size were achieved.

Flash sintering in isochronal mode was successfully applied on cylindrical green pellets produced with the synthesized nanopowders, and very rapid densification was

recorded especially for Mg-doped samples. Interestingly, it was demonstrated that CDHA phase is too resistive, at least for electric field lower than 2000 V cm^{-1}, to ensure the critical condition needed to trigger the thermal runaway mechanism; therefore, the flash event can occur only after β-TCP formation. In addition, β-phase is characterized by a rapid resistivity reduction with increasing the temperature, thus deviating from the expected Arrhenius-like behavior, most likely because of the non-linear grain growth of the new crystals. A semi-empirical relation describing the inverse proportionality between the applied field and the flash onset was found, pointing out the higher conductivity of Mg-doped material. On the other hand, the high reactivity of the nanopowders leads to larger amount of retained α-phase in the undoped sintered sample (absent in presence of Mg), if compared to TCP micropowders,

Flash sintering was also applied in isothermal mode on the undoped composition, previously calcinated to β-TCP, thus obtaining an almost fully dense microstructure (~500 nm) at 900°C in just few seconds (745 V cm^{-1} and 7.5 mA mm^{-2}). Once again, a thermal model was proposed to describe and predict the flash conditions and the real sample temperature. On these basis, and considering the limitation imposed by the β→α transition, it was possible to build two different processing maps including and relating furnace temperature, electric field and current limit.

4.3 Precipitation method: Strontium doping HA

Strontium-doped HA nanopowders (0, 5, 10, 25, 50, 75, and 100 mol% Sr^{2+}) were successfully synthesized by precipitation from aqueous solutions, always generating a single crystalline phase where Ca^{2+} and Sr^{2+} ions are placed in the same lattice positions.

It was shown how the progressive substitution of the cations induces several modifications in the considered system. For example, the presence of a second ion in the apatitic structure, being perceived as point defect, inhibits the crystallization and intermediate bi-cationic compositions are constituted by smaller crystallites (~25 nm) with respect to pure Ca-HA and Sr-HA nanopowders (~50 nm).

On the other hand, the powder morphology is influenced by the Sr presence, the particles being gradually elongated along the *c* direction. Analogously, crystalline structure is affected by the expansion of the unit cell, more pronounced for *c* parameter. As a direct consequence, functional groups are rearranged within the apatitic lattice, P-O bonds become progressively weaker and OH spatial density decreases.

References

[1] D. F. Williams, “On the nature of biomaterials,” *Biomaterials*, vol. 30, no. 30, pp. 5897–5909, 2009.

[2] R. Narayanan, S. K. Seshadri, T. Y. Kwon, and K. H. Kim, “Calcium phosphate-based coatings on titanium and its alloys,” *J. Biomed. Mater. Res. - Part B Appl. Biomater.*, vol. 85, no. 1, pp. 279–299, 2008.

[3] M. Roy, A. Bandyopadhyay, and S. Bose, “Induction plasma sprayed Sr and Mg doped nano hydroxyapatite coatings on Ti for bone implant,” *J. Biomed. Mater. Res. - Part B Appl. Biomater.*, vol. 99 B, no. 2, pp. 258–265, 2011.

[4] Y. Ramot, M. Haim-Zada, A. J. Domb, and A. Nyska, “Biocompatibility and safety of PLA and its copolymers,” *Advanced Drug Delivery Reviews*, vol. 107. Elsevier, pp. 153–162, 15-Dec-2016.

[5] L. L. Hench, “Bioglass: 10 milestones from concept to commerce,” *J. Non. Cryst. Solids*, vol. 432, pp. 2–8, 2016.

[6] O. Bretcanu, X. Chatzistavrou, K. Paraskevopoulos, R. Conradt, I. Thompson, and A. R. Boccaccini, “Sintering and crystallisation of 45S5 Bioglass® powder,” *J. Eur. Ceram. Soc.*, vol. 29, no. 16, pp. 3299–3306, 2009.

[7] M. Šupová, “Substituted hydroxyapatites for biomedical applications: A review,” *Ceram. Int.*, vol. 41, no. 8, pp. 9203–9231, 2015.

[8] J. T. B. Ratnayake, M. Mucalo, and G. J. Dias, “Substituted hydroxyapatites for bone regeneration: A review of current trends,” *J. Biomed. Mater. Res. - Part B Appl. Biomater.*, pp. 1–15, 2016.

[9] L. L. Hench, “Bioceramics,” *Stress Int. J. Biol. Stress*, vol. 28, pp. 1705–1728, 1998.

[10] K. Morsi, H. Keshavan, and S. Bal, “Hot pressing of graded ultrafine-grained alumina bioceramics,” *Mater. Sci. Eng. A*, vol. 386, no. 1–2, pp. 384–389, 2004.

[11] A. Kammermeier, M. Rosentritt, M. Behr, S. Schneider-Feyrer, and V. Preis, “In vitro performance of one- and two-piece zirconia implant systems for anterior application,” *J. Dent.*, vol. 53, no. 6, pp. 94–101, Jun. 2016.

[12] S. Sánchez-Salcedo, F. Balas, I. Izquierdo-Barba, and M. Vallet-Regí, "In vitro structural changes in porous HA/β-TCP scaffolds in simulated body fluid," *Acta Biomater.*, vol. 5, no. 7, pp. 2738–2751, Sep. 2009.

[13] J. Y. Rho, L. Kuhn-Spearing, and P. Zioupos, "Mechanical properties and the hierarchical structure of bone," *Med. Eng. Phys.*, vol. 20, no. 2, pp. 92–102, 1998.

[14] U. G. K. Wegst, H. Bai, E. Saiz, A. P. Tomsia, and R. O. Ritchie, "Bioinspired structural materials," *Nat. Mater.*, vol. 14, no. 1, pp. 23–36, 2014.

[15] J. P. Lafon, E. Champion, and D. Bernache-Assollant, "Processing of AB-type carbonated hydroxyapatite Ca10-x(PO4)6-x(CO3)x(OH)2-x-2y(CO3)y ceramics with controlled composition," *J. Eur. Ceram. Soc.*, vol. 28, no. 1, pp. 139–147, 2008.

[16] C. Combes and C. Rey, "Amorphous calcium phosphates: Synthesis, properties and uses in biomaterials," *Acta Biomater.*, vol. 6, no. 9, pp. 3362–3378, 2010.

[17] S. Kannan, F. Goetz-Neunhoeffer, J. Neubauer, and J. M. F. Ferreira, "Ionic substitutions in biphasic hydroxyapatite and β-tricalcium phosphate mixtures: Structural analysis by rietveld refinement," *J. Am. Ceram. Soc.*, vol. 91, no. 1, pp. 1–12, 2008.

[18] M. A. Rubin, I. Jasiuk, J. Taylor, J. Rubin, T. Ganey, and R. P. Apkarian, "TEM analysis of the nanostructure of normal and osteoporotic human trabecular bone," *Bone*, vol. 33, no. 3, pp. 270–282, 2003.

[19] R. Murugan and S. Ramakrishna, "Development of nanocomposites for bone grafting," *Compos. Sci. Technol.*, vol. 65, no. 15–16 SPEC. ISS., pp. 2385–2406, 2005.

[20] G. Daculsi, R. Z. Legeros, E. Nery, K. Lynch, and B. Kerebel, "Transformation of biphasic calcium phosphate ceramics in vivo: Ultrastructural and physicochemical characterization," *J. Biomed. Mater. Res.*, vol. 23, no. 8, pp. 883–894, 1989.

[21] T. P. Feenstra and P. L. De Bruyn, "The ostwald rule of stages in precipitation from highly supersaturated solutions: a model and its application to the formation of the nonstoichiometric amorphous calcium phosphate precursor phase," *J. Colloid Interface Sci.*, vol. 84, no. 1, pp. 66–72, 1981.

[22] M. L. Watson and R. A. Robinson, “Collagen-crystal relationships in bone. II. Electron microscope study of basic calcium phosphate crystals,” *Am. J. Anat.*, vol. 93, no. 1, pp. 25–59, 1953.

[23] S. V. Dorozhkin, “Nanosized and nanocrystalline calcium orthophosphates,” *Acta Biomater.*, vol. 6, no. 3, pp. 715–734, 2010.

[24] A. J. Ambard and L. Mueninghoff, “Calcium phosphate cement: Review of mechanical and biological properties,” *J. Prosthodont.*, vol. 15, no. 5, pp. 321–328, 2006.

[25] N. Eliaz and N. Metoki, “Calcium phosphate bioceramics: A review of their history, structure, properties, coating technologies and biomedical applications,” *Materials (Basel).*, vol. 10, no. 4, 2017.

[26] P. I. Branemark, “Osseointegration and its experimental background,” *J. Prosthet. Dent.*, vol. 50, no. 3, pp. 399–410, 1983.

[27] N. Eliaz and T. M. Sridh, “Electrocrystallization of hydroxyapatite and its dependence on solution conditions,” *Cryst. Growth Des.*, vol. 8, no. 11, pp. 3965–3977, 2008.

[28] K. A. Gross and C. C. Berndt, “Thermal processing of hydroxyapatite for coating production,” *J. Biomed. Mater. Res.*, vol. 39, no. 4, pp. 580–587, 1998.

[29] S. Serena, L. Carbajal, M. A. Sainz, and A. Caballero, “Thermodynamic assessment of the system CaO-P2O5: Application of the ionic two-sublattice model to glass-forming melts,” *J. Am. Ceram. Soc.*, vol. 94, no. 9, pp. 3094–3103, 2011.

[30] N. Rangavittal, a R. Landa-Cánovas, J. M. González-Calbet, and M. Vallet-Regí, “Structural study and stability of hydroxyapatite and beta-tricalcium phosphate: two important bioceramics.,” *J. Biomed. Mater. Res.*, vol. 51, no. 4, pp. 660–668, 2000.

[31] M. Yashima and A. Sakai, “High-temperature neutron powder diffraction study of the structural phase transition between a and a’ phases in tricalcium phosphate Ca3(PO4)2,” *Chem. Phys. Lett.*, vol. 372, no. 5–6, pp. 779–783, 2003.

[32] C. L. Camiré, U. Gbureck, W. Hirsiger, and M. Bohner, “Correlating crystallinity and reactivity in an a-tricalcium phosphate,” *Biomaterials*, vol. 26, no. 16, pp. 2787–2794, 2005.

[33] M. Mathew, L. W. Schroeder, B. Dickens, and W. E. Brown, “The crystal structure of α-Ca3(PO4)2,” *Acta Crystallogr. Sect. B Struct. Crystallogr. Cryst. Chem.*, vol. 33, no. 5, pp. 1325–1333, 1977.

[34] S. V. Dorozhkin and S. V. Dorozhkin, “Self-Setting Calcium Orthophosphate Formulations: Cements, Concretes, Pastes and Putties,” *Int. J. Mater. Chem.*, vol. 1, no. 1, pp. 1–48, 2011.

[35] N. Döbelin, L. Galea, U. Eggenberger, J. M. F. Ferreira, and M. Bohner, “Recrystallization of amorphized α-TCP,” *Key Eng. Mater.*, vol. 493–494, pp. 219–224, 2012.

[36] M. Yashima, A. Sakai, T. Kamiyama, and A. Hoshikawa, “Crystal structure analysis of β-tricalcium phosphate Ca3(PO4)2 by neutron powder diffraction,” *J. Solid State Chem.*, vol. 175, no. 2, pp. 272–277, 2003.

[37] N. Matsumoto, K. Yoshida, K. Hashimoto, and Y. Toda, “Thermal stability of B-tricalcium phosphate doped with monovalent metal ions,” *Mater. Res. Bull.*, vol. 44, no. 9, pp. 1889–1894, 2009.

[38] D. S. Metsger, T. D. Driskell, and J. R. Paulsrud, “Tricalcium Phosphate Ceramic—A Resorbable Bone Implant: Review and Current Status,” *J. Am. Dent. Assoc.*, vol. 105, no. 6, pp. 1035–1038, 1982.

[39] M. L. Weiner, W. F. Salminen, P. R. Larson, R. A. Barter, J. L. Kranetz, and G. S. Simon, “Toxicological review of inorganic phosphates,” *Food Chem. Toxicol.*, vol. 39, no. 8, pp. 759–786, 2001.

[40] H. S. Ryu, H. J. Youn, K. Sun Hong, B. S. Chang, C. K. Lee, and S. S. Chung, “An improvement in sintering property of B-tricalcium phosphate by addition of calcium pyrophosphate,” *Biomaterials*, vol. 23, no. 3, pp. 909–914, 2002.

[41] R. A. Van Santen, “The Ostwald Step Rule,” *J. Phys. Chem.*, vol. 88, no. 24, pp. 5768–5769, 1984.

[42] S. C. Liou and S. Y. Chen, “Transformation mechanism of different chemically precipitated apatitic precursors into B-tricalcium phosphate upon calcination,” *Biomaterials*, vol. 23, no. 23, pp. 4541–4547, 2002.

[43] J. S. Bow, S. C. Liou, and S. Y. Chen, “Structural characterization of room-temperature synthesized nano-sized β-tricalcium phosphate,” *Biomaterials*, vol. 25, no. 16, pp. 3155–3161, 2004.

[44] R. A. Surmenev, “A review of plasma-assisted methods for calcium

phosphate-based coatings fabrication," *Surf. Coatings Technol.*, vol. 206, no. 8–9, pp. 2035–2056, 2012.

[45] K. Itatani, T. Nishioka, A. Kishioka, and I. Introduction, "Sinterability of Beta-Calcium Orthophosphate Powder Prepared by Spray-Pyrolysis," *J. Am. Ceram. Soc.*, vol. 77, no. 3, pp. 801–805, 1994.

[46] H. Monma and M. Goto, "Behavior of in the a↔B Tricalcium Phase Transformation Phosphate," *Yogyo-Kyokai-Shi*, vol. 91, no. 10, pp. 55–57, 1983.

[47] E. Fernández *et al.*, "Kinetic study of the setting reaction of a calcium phosphate bone cement.," *J. Biomed. Mater. Res.*, vol. 32, no. 3, pp. 367–374, 1996.

[48] P. M. C. Torres *et al.*, "Influence of Mg-doping, calcium pyrophosphate impurities and cooling rate on the allotropic a ↔ B-tricalcium phosphate phase transformations," *J. Eur. Ceram. Soc.*, vol. 36, no. 3, pp. 817–827, 2016.

[49] R. G. Carrodeguas and S. De Aza, "a-Tricalcium phosphate: Synthesis, properties and biomedical applications," *Acta Biomater.*, vol. 7, no. 10, pp. 3536–3546, 2011.

[50] R. Enderle, F. Götz-Neunhoeffer, M. Göbbels, F. A. Müller, and P. Greil, "Influence of magnesium doping on the phase transformation temperature of β-TCP ceramics examined by Rietveld refinement," *Biomaterials*, vol. 26, no. 17, pp. 3379–3384, 2005.

[51] D. M. B. Wolff, E. G. Ramalho, and W. Acchar, "Phase Transition behaviour of Tricalcium phosphate (TCP) doped with MgO and TiO2 as additives," *Mater. Sci. Forum*, vol. 530–531, pp. 581–586, 2006.

[52] L. Carbajal, A. Caballero, and M. A. Sainz, "Design and processing of ZnO doped tricalcium phosphate based materials: Influence of B/a polymorph phase assemblage on microstructural evolution," *J. Eur. Ceram. Soc.*, vol. 32, no. 3, pp. 569–577, 2012.

[53] H. S. Ryu *et al.*, "Magnesia-doped HA/B-TCP ceramics and evaluation of their biocompatibility," *Biomaterials*, vol. 25, no. 3, pp. 393–401, 2004.

[54] A. Bandyopadhyay, J. Petersen, G. Fielding, S. Banerjee, and S. Bose, "ZnO, SiO 2, and SrO doping in resorbable tricalcium phosphates: Influence on strength degradation, mechanical properties, and in vitro bone-cell material interactions," *J. Biomed. Mater. Res. - Part B Appl.*

Biomater., pp. 2203–2212, 2012.

[55] S. Adzila, M. Murad, and I. Sopyan, “Doping Metal into Calcium Phosphate Phase for Better Performance of Bone Implant Materials,” *Recent Patents Mater. Sci.*, vol. 5, no. 1, pp. 18–47, 2012.

[56] N. Matsumoto, K. Yoshida, K. Hashimoto, and Y. Toda, “Dissolution mechanisms of β-tricalcium phosphate doped with monovalent metal ions,” *J. Ceram. Soc. Japan*, vol. 118, no. 1378, pp. 451–457, 2010.

[57] J. Ando, “Phase Diagrams of Ca3(PO4)2-Mg3 (PO4)2 and Ca3(PO4)2-CaNaPO4,” *Bull. Chem. Soc. Jpn.*, vol. 31, no. 2, pp. 201–205, 1958.

[58] D. Zahn and O. Hochrein, “On the composition and atomic arrangement of calcium-deficient hydroxyapatite: An ab-initio analysis,” *J. Solid State Chem.*, vol. 181, no. 8, pp. 1712–1716, 2008.

[59] J. Gómez-Morales, M. Iafisco, J. M. Delgado-López, S. Sarda, and C. Drouet, “Progress on the preparation of nanocrystalline apatites and surface characterization: Overview of fundamental and applied aspects,” *Prog. Cryst. Growth Charact. Mater.*, vol. 59, no. 1, pp. 1–46, 2013.

[60] W. Suchanek and M. Yoshimura, “Processing and properties of hydroxyapatite-based biomaterials for use as hard tissue replacement implants,” *J. Mater. Res.*, vol. 13, no. 1, pp. 94–117, 1998.

[61] V. P. Orlovskii, V. S. Komlev, and S. M. Barinov, “Hydroxyapatite and hydroxyapatite-based ceramics,” *Inorg. Mater.*, vol. 38, no. 10, pp. 973–984, 2002.

[62] E. Champion, “Sintering of calcium phosphate bioceramics,” *Acta Biomater.*, vol. 9, no. 4, pp. 5855–5875, 2013.

[63] M. Jarcho, “Hydroxylapatite Synthesis and Characterization in Sense Polycristalline Forms,” *J. Mater. Sci.*, vol. 11, pp. 2027–2035, 1976.

[64] R. Halouani, D. Bernache-Assolant, E. Champion, and A. Ababou, “Microstructure and related mechanical properties of hot pressed hydroxyapatite ceramics,” *J. Mater. Sci. Mater. Med.*, vol. 5, no. 8, pp. 563–568, 1994.

[65] X. Guo, P. Xiao, J. Liu, and Z. Shen, “Fabrication of nanostructured hydroxyapatite via hydrothermal synthesis and spark plasma sintering,” *J. Am. Ceram. Soc.*, vol. 88, no. 4, pp. 1026–1029, 2005.

[66] E. D. Eanes, J. D. Termine, and M. U. Nylen, “An electron microscopic study of the formation of amorphous calcium phosphate and its transformation to crystalline apatite,” *Calcif. Tissue Res.*, vol. 12, no. 1, pp. 143–158, 1973.

[67] F. Betts and a. S. Posner, “An X-ray radial distribution study of amorphous calcium phosphate,” *Mater. Res. Bull.*, vol. 9, no. 7, pp. 353–360, 1974.

[68] G. Treboux, P. Layrolle, N. Kanzaki, K. Onuma, and A. Ito, “Symmetry of Posner ’ s Cluster,” *J. Am. Chem. Soc.*, vol. 122, pp. 8323–8324, 2000.

[69] N. C. Blumenthal, F. Betts, and A. S. Posner, “Formation and structure of Ca-deficient hydroxyapatite,” *Calcif. Tissue Int.*, vol. 33, no. 1, pp. 111–117, 1981.

[70] E. Landi, E. Landi, A. Tampieri, G. Celotti, and S. Sprio, “Densification Behavior and Mechanisms of Synthetic Hydroxyapatite Densification behaviour and mechanisms of,” *J. Eur. Ceram. Soc. Eur. Ceram. Soc.*, vol. 2219, no. DECEMBER 2000, pp. 2377–2387, 2016.

[71] C. B. Carter and M. G. Norton, “Ceramic Materials Science and Engineering,” p. 716, 2007.

[72] M. N. Rahaman, *Ceramic processign and sintering*. 2003.

[73] D. Bernache-Assollant, A. Ababou, E. Champion, and M. Heughebaert, “Sintering of calcium phosphate hydroxyapatite Ca10(PO4)6(OH)2 I. Calcination and particle growth,” *J. Eur. Ceram. Soc.*, vol. 23, no. 2, pp. 229–241, 2003.

[74] P. Van Landuyt, F. Li, J. P. Keustermans, J. M. Streydio, F. Delannay, and E. Munting, “The influence of high sintering temperatures on the mechanical properties of hydroxylapatite,” *J. Mater. Sci. Mater. Med.*, vol. 6, no. 1, pp. 8–13, 1995.

[75] M. Descamps, J. C. Hornez, and A. Leriche, “Effects of powder stoichiometry on the sintering of β-tricalcium phosphate,” *J. Eur. Ceram. Soc.*, vol. 27, no. 6, pp. 2401–2406, 2007.

[76] M. Asada, K. Oukami, S. Nakamura, and K. Takahashi, “Microstructure and mechanical properties on non-stoichiometric apatite ceramics and sinterability of raw powder,” *J Ceram Soc Jpn Int Ed*, vol. 96, no. 1113, pp. 583–586, 1988.

[77] A. Destainville, A. Rolo, E. Champion, and D. Bernache-Assollant,

"Synthesis and Characterization of Beta Tricalcium Phosphate," *Key Eng. Mater.*, vol. 240–242, pp. 489–492, 2002.

[78] F. Zhang, K. Lin, J. Chang, J. Lu, and C. Ning, "Spark plasma sintering of macroporous calcium phosphate scaffolds from nanocrystalline powders," *J. Eur. Ceram. Soc.*, vol. 28, no. 3, pp. 539–545, 2008.

[79] Z. A. Munir, U. Anselmi-Tamburini, and M. Ohyanagi, "The effect of electric field and pressure on the synthesis and consolidation of materials: A review of the spark plasma sintering method," *J. Mater. Sci.*, vol. 41, no. 3, pp. 763–777, 2006.

[80] M. Cologna, B. Rashkova, and R. Raj, "Flash sintering of nanograin zirconia in <5 s at 850°C," *J. Am. Ceram. Soc.*, vol. 93, no. 11, pp. 3556–3559, 2010.

[81] R. Raj, M. Cologna, G. Prette, and V. Sglavo, "Methods of Flash Sintering. Patent Application US 13/562,040," 2013.

[82] A. Feteira, "Negative temperature coefficient resistance (NTCR) ceramic thermistors: An industrial perspective," *J. Am. Ceram. Soc.*, vol. 92, no. 5, pp. 967–983, 2009.

[83] M. Cologna, J. S. C. Francis, and R. Raj, "Field assisted and flash sintering of alumina and its relationship to conductivity and MgO-doping," *J. Eur. Ceram. Soc.*, vol. 31, no. 15, pp. 2827–2837, 2011.

[84] M. Biesuz and V. M. Sglavo, "Flash sintering of alumina: Effect of different operating conditions on densification," *J. Eur. Ceram. Soc.*, vol. 36, no. 10, pp. 2535–2542, 2016.

[85] J. C. M'Peko, J. S. C. Francis, and R. Raj, "Field-assisted sintering of undoped BaTiO3: Microstructure evolution and dielectric permittivity," *J. Eur. Ceram. Soc.*, vol. 34, no. 15, pp. 3655–3660, 2014.

[86] N. Shomrat, S. Baltianski, C. A. Randall, and Y. Tsur, "Flash sintering of potassium-niobate," *J. Eur. Ceram. Soc.*, vol. 35, no. 7, pp. 2209–2213, 2015.

[87] N. Shomrat, S. Baltianski, E. Dor, and Y. Tsur, "The influence of doping on flash sintering conditions in SrTi1−xFexO3−δ," *J. Eur. Ceram. Soc.*, pp. 1–10, 2016.

[88] S. K. Jha, J. M. Lebrun, and R. Raj, "Phase transformation in the alumina-titania system during flash sintering experiments," *J. Eur. Ceram. Soc.*, vol.

36, no. 3, pp. 733–739, 2016.

[89] Y. Zhang, J. Nie, and J. Luo, “Effects of phase and doping on flash sintering of TiO2,” *J. Ceram. Soc. Japan*, vol. 124, no. 4, pp. 296–300, 2016.

[90] Y. Zhang and J. Luo, “Promoting the flash sintering of ZnO in reduced atmospheres to achieve nearly full densities at furnace temperatures of <120°C,” *Scr. Mater.*, vol. 106, pp. 26–29, 2015.

[91] S. Grasso *et al.*, “Flash Spark Plasma Sintering (FSPS) of a and B SiC,” *J. Am. Ceram. Soc.*, vol. 99, no. 5, pp. 1534–1543, 2016.

[92] B. Niu, F. Zhang, J. Zhang, W. Ji, W. Wang, and Z. Fu, “Ultra-fast densification of boron carbide by flash spark plasma sintering,” *Scr. Mater.*, vol. 116, pp. 127–130, 2016.

[93] R. Muccillo and E. N. S. Muccillo, “Electric field-assisted flash sintering of tin dioxide,” *J. Eur. Ceram. Soc.*, vol. 34, no. 4, pp. 915–923, 2014.

[94] J. S. C. Francis and R. Raj, “Influence of the field and the current limit on flash sintering at isothermal furnace temperatures,” *J. Am. Ceram. Soc.*, vol. 96, no. 9, pp. 2754–2758, 2013.

[95] J. A. Downs and V. M. Sglavo, “Electric field assisted sintering of cubic zirconia at 390°C,” *J. Am. Ceram. Soc.*, vol. 96, no. 5, pp. 1342–1344, 2013.

[96] Y. Du, A. J. Stevenson, D. Vernat, M. Diaz, and D. Marinha, “Estimating Joule heating and ionic conductivity during flash sintering of 8YSZ,” *J. Eur. Ceram. Soc.*, vol. 36, no. 3, pp. 749–759, 2016.

[97] T. Jiang *et al.*, “Understanding the flash sintering of rare-earth-doped ceria for solid oxide fuel cell,” *J. Am. Ceram. Soc.*, vol. 98, no. 6, pp. 1717–1723, 2015.

[98] M. Biesuz, G. Dell’Agli, L. Spiridigliozzi, C. Ferone, and V. M. Sglavo, “Conventional and field-assisted sintering of nanosized Gd-doped ceria synthesized by co-precipitation,” *Ceram. Int.*, vol. 42, no. 10, pp. 11766–11771, 2016.

[99] A. Gaur and V. M. Sglavo, “Flash-sintering of MnCo2O4 and its relation to phase stability,” *J. Eur. Ceram. Soc.*, vol. 34, no. 10, pp. 2391–2400, 2014.

[100] E. Zapata-Solvas, D. Gómez-García, A. Domínguez-Rodríguez, and R. I.

Todd, “Ultra-fast and energy-efficient sintering of ceramics by electric current concentration,” *Sci. Rep.*, vol. 5, pp. 1–7, 2015.

[101] S. Grasso *et al.*, “Flash spark plasma sintering (FSPS) of pure ZrB2,” *J. Am. Ceram. Soc.*, vol. 97, no. 8, pp. 2405–2408, 2014.

[102] M. Biesuz, P. Luchi, A. Quaranta, A. Martucci, and V. M. Sglavo, “Photoemission during flash sintering: An interpretation based on thermal radiation,” *J. Eur. Ceram. Soc.*, vol. 37, no. 9, pp. 3125–3130, 2017.

[103] R. Raj, “Joule heating during flash-sintering,” *J. Eur. Ceram. Soc.*, vol. 32, no. 10, pp. 2293–2301, 2012.

[104] I. J. Hewitt, A. A. Lacey, and R. I. Todd, “A Mathematical Model for Flash Sintering,” *Math. Model. Nat. Phenom.*, pp. 1–16, 2015.

[105] R. I. Todd, E. Zapata-Solvas, R. S. Bonilla, T. Sneddon, and P. R. Wilshaw, “Electrical characteristics of flash sintering: Thermal runaway of Joule heating,” *J. Eur. Ceram. Soc.*, vol. 35, no. 6, pp. 1865–1877, 2015.

[106] Y. Dong and I.-W. Chen, “Predicting the Onset of Flash Sintering,” *J. Am. Ceram. Soc.*, vol. 98, no. 8, pp. 2333–2335, 2015.

[107] J. G. Pereira Da Silva, J. M. Lebrun, H. A. Al-Qureshi, R. Janssen, and R. Raj, “Temperature Distributions during Flash Sintering of 8% Yttria-Stabilized Zirconia,” *J. Am. Ceram. Soc.*, vol. 98, no. 11, pp. 3525–3528, 2015.

[108] I. Bajpai, Y. H. Han, J. Yun, J. Francis, S. Kim, and R. Raj, “Preliminary investigation of hydroxyapatite microstructures prepared by flash sintering,” *Adv. Appl. Ceram.*, vol. 115, no. 5, pp. 276–281, 2016.

[109] Y. Pan, J. L. Huang, and C. Y. Shao, “Preparation of beta-TCP with high thermal stability by solid reaction route,” *J. Mater. Sci.*, vol. 38, no. 5, pp. 1049–1056, 2003.

[110] I. Cacciotti and A. Bianco, “High thermally stable Mg-substituted tricalcium phosphate via precipitation,” *Ceram. Int.*, vol. 37, no. 1, pp. 127–137, 2011.

[111] A. Bigi, E. Boanini, C. Capuccini, and M. Gazzano, “Strontium-substituted hydroxyapatite nanocrystals,” *Inorganica Chim. Acta*, vol. 360, no. 3, pp. 1009–1016, 2007.

[112] L. Lutterotti, M. Bortolotti, G. Ischia, I. Lonardelli, and H. R. Wenk, “Rietveld texture analysis from diffraction images,” *Zeitschrift fur Krist. Suppl.*, vol. 1,

no. 26, pp. 125–130, 2007.

[113] C. W. Huang and C. H. Hsueh, “Piston-on-three-ball versus piston-on-ring in evaluating the biaxial strength of dental ceramics,” *Dent. Mater.*, vol. 27, no. 6, pp. e117–e123, 2011.

[114] Y. A. Cengel, *Introduction to Thermodynamics and Heat Transfer*, 2nd ed. 2009.

[115] E. P. Egan, Z. T. Wakefield, and K. L. Elmore, “High-Temperature Heat Content of Hydroxyapatite,” *J. Am. Chem. Soc.*, vol. 72, no. 6, pp. 2418–2421, 1950.

[116] Y. Dong and I. W. Chen, “Onset Criterion for Flash Sintering,” *J. Am. Ceram. Soc.*, vol. 98, no. 12, pp. 3624–3627, 2015.

[117] J. C. Araújo, M. S. Sader, E. L. Moreira, V. C. A. Moraes, R. Z. LeGeros, and G. A. Soares, “Maximum substitution of magnesium for calcium sites in Mg-β-TCP structure determined by X-ray powder diffraction with the Rietveld refinement,” *Mater. Chem. Phys.*, vol. 118, no. 2–3, pp. 337–340, 2009.

[118] M. Frasnelli *et al.*, “Synthesis and characterization of strontium-substituted hydroxyapatite nanoparticles for bone regeneration,” *Mater. Sci. Eng. C*, vol. 71, pp. 653–662, 2017.

[119] J. Janek and C. Korte, “Electrochemical blackening of yttria-stabilized zirconia - morphological instability of the moving reaction front,” *Solid State Ionics*, vol. 116, no. 3–4, pp. 181–195, 1999.

[120] M. Nagai *et al.*, “Electrical conductivity of calcium phosphate ceramics with various Ca/P ratios,” *J. Mater. Sci.*, vol. 26, no. 11, pp. 2949–2953, 1991.

[121] J. P. Gittings *et al.*, “Influence of Porosity on Polarisation and Electrical Properties of Hydroxyapatite Based Ceramics,” *Ferroelectrics*, vol. 390, no. 1, pp. 168–176, 2009.

[122] W. Wang, S. Itoh, N. Yamamoto, A. Okawa, A. Nagai, and K. Yamashita, “Electrical polarization of β-tricalcium phosphate ceramics,” *J. Am. Ceram. Soc.*, vol. 93, no. 8, pp. 2175–2177, 2010.

[123] S. Hoeges, M. Lindner, H. Fischer, W. Meiners, and K. Wissenbach, “Manufacturing of bone substitute implants using Selective Laser Melting,” *Analysis*, pp. 2230–2234, 2009.

[124] A. Lecomte, H. Gautier, and J. M. Bouler, “Biphasic Calcium Phosphate: A Comparative Study of Interconnected Porosity in Two Ceramics,” *J. Biomed. Mater. Res. B. Appl. Biomater.*, vol. 84B, no. 1, pp. 1–6, 2008.

[125] M. A. Ahmed, S. F. Mansour, S. I. El-Dek, S. M. Abd-Elwahab, and M. K. Ahmed, “Characterization and annealing performance of calcium phosphate nanoparticles synthesized by co-precipitation method,” *Ceram. Int.*, vol. 40, no. 8 PART B, pp. 12807–12820, 2014.

[126] R. M. Wilson, J. C. Elliott, and S. E. P. Dowker, “Formate incorporation in the structure of Ca-deficient apatite: Rietveld structure refinement,” *J. Solid State Chem.*, vol. 174, no. 1, pp. 132–140, 2003.

[127] E. I. Dorozhkina and S. V. Dorozhkin, “Mechanism of the solid-state transformation of a calcium-deficient hydroxyapatite (CDHA) into biphasic calcium phosphate (BCP) at elevated temperatures,” *Chem. Mater.*, vol. 14, no. 10, pp. 4267–4272, 2002.

[128] M. Frasnelli and V. M. Sglavo, “Effect of Mg2+ doping on beta-alpha phase transition in tricalcium phosphate (TCP) bioceramics,” *Acta Biomater.*, vol. 33, pp. 283–289, Mar. 2016.

[129] A. Yasukawa, S. Ouchi, K. Kandori, and T. Ishikawa, “Preparation and characterization of magnesium–calcium hydroxyapatites,” *J. Mater. Chem.*, vol. 6, no. 8, pp. 1401–1405, 1996.

[130] Y. Sakhno, L. Bertinetti, M. Iafisco, A. Tampieri, N. Roveri, and G. Martra, “Surface hydration and cationic sites of nanohydroxyapatites with amorphous or crystalline surfaces: A comparative study,” *J. Phys. Chem. C*, vol. 114, no. 39, pp. 16640–16648, 2010.

[131] C. Zhang *et al.*, “Self-activated luminescent and mesoporous strontium hydroxyapatite nanorods for drug delivery,” *Biomaterials*, vol. 31, no. 12, pp. 3374–3383, 2010.

[132] Z. Y. Li *et al.*, “Chemical composition, crystal size and lattice structural changes after incorporation of strontium into biomimetic apatite,” *Biomaterials*, vol. 28, no. 7, pp. 1452–1460, 2007.

[133] D. Laurencin *et al.*, “Magnesium incorporation into hydroxyapatite,” *Biomaterials*, vol. 32, no. 7, pp. 1826–1837, 2011.

[134] T. KIJIMA and M. TSUTSUMI, “Preparation and Thermal Properties of Dense Polycrystalline Oxyhydroxyapatite,” *J. Am. Ceram. Soc.*, vol. 62, no. 9–10, pp. 455–460, 1979.

[135] M. Thommes *et al.*, “Physisorption of gases, with special reference to the evaluation of surface area and pore size distribution (IUPAC Technical Report),” *Pure Appl. Chem.*, vol. 87, no. 9–10, pp. 1051–1069, 2015.

[136] A. Mortier, J. Lemaitre, L. Rodrique, and P. G. Rouxhet, “Synthesis and thermal behavior of well-crystallized calcium-deficient phosphate apatite,” *J. Solid State Chem.*, vol. 78, no. 2, pp. 215–219, 1989.

[137] S. Chaturvedi and P. N. Dave, “Review on Thermal Decomposition of Ammonium Nitrate,” *J. Energ. Mater.*, vol. 31, no. 1, pp. 1–26, 2013.

[138] M. T. Fulmer, R. I. Martin, and P. W. Brown, “Formation of calcium deficient hydroxyapatite at near-physiological temperature,” *J. Mater. Sci. Mater. Med.*, vol. 3, no. 4, pp. 299–305, 1992.

[139] J. S. C. Francis, M. Cologna, and R. Raj, “Particle size effects in flash sintering,” *J. Am. Ceram. Soc.*, vol. 32, pp. 3129–3136, 2012.

[140] D. P. Joshi and K. Sen, “Effect of grain size on the resistivity of polycrystalline material,” *Sol. Cells*, vol. 9, no. 4, pp. 261–267, 1983.

[141] J. H. Kim, S. H. Kim, H. K. Kim, T. Akaike, and S. C. Kim, “Synthesis and characterization of hydroxyapatite crystals: A review study on the analytical methods,” *J. Biomed. Mater. Res.*, vol. 62, no. 4, pp. 600–612, 2002.

[142] A. Kaflak and W. Kolodziejski, “Complementary information on water and hydroxyl groups in nanocrystalline carbonated hydroxyapatites from TGA, NMR and IR measurements,” *J. Mol. Struct.*, vol. 990, no. 1, pp. 263–270, 2011.

[143] F. Munarin *et al.*, “Micro- and nano-hydroxyapatite as active reinforcement for soft biocomposites,” *Int. J. Biol. Macromol.*, vol. 72, pp. 199–209, 2015.

[144] J. Kolmas and W. Kolodziejski, “Inverse 31P→1H NMR cross-polarization in hydrated nanocrystalline calcium hydroxyapatite,” *Chem. Phys. Lett.*, vol. 554, pp. 128–132, 2012.

[145] J. Kolmas, A. Slosarczyk, A. Wojtowicz, and W. Kolodziejski, “Estimation of the specific surface area of apatites in human mineralized tissues using 31P MAS NMR,” *Solid State Nucl. Magn. Reson.*, vol. 32, no. 2, pp. 53–58, 2007.

[146] B. O. Fowler, “Infrared studies of apatites. II. Preparation of normal and isotopically substituted calcium, strontium, and barium hydroxyapatites and spectra-structure-composition correlations,” *Inorg. Chem.*, vol. 13, no. 1,

pp. 207–214, Jan. 1974.

[147] Y. Wang *et al.*, "Water-mediated structuring of bone apatite," *Nat. Mater.*, vol. 12, no. 12, pp. 1144–1153, Nov. 2013.

Scientific Production

M. Frasnelli and V.M. Sglavo: Alpha–Beta Phase Transformation in Tricalcium Phosphate (TCP) Ceramics: Effect of Mg2+ Doping, *Advances in Bioceramics and Porous Ceramics VIII: Ceramic Engineering and Science Proceedings (CESP)*; 36(5), 2016: 63.

M. Frasnelli and V.M. Sglavo: Effect of Mg^{2+} doping on beta–alpha phase transition in tricalcium phosphate (TCP) bioceramics, *Acta Biomaterialia*; 33, 2016: 283-289.

M. Frasnelli, F. Cristofaro, V.M. Sglavo, S. Diré, E. Callone, R. Ceccato, G. Bruni, A.I. Cornaglia, L. Visai: Synthesis and characterization of strontium-substituted hydroxyapatite nanoparticles for bone regeneration, *Materials Science & Engineering C*; 71, 2017: 653-662.

M. Biesuz, L. Spiridigliozzi, M. Frasnelli, G. Dell'Agli, V.M. Sglavo: Rapid densification of Samarium-doped Ceria ceramic with nanometric grain size at 900–1100 °C, *Materials Letters*; 190, 2017: 17-19.

M.O. Prado, M. Biesuz, M. Frasnelli, F. Benedetto, V.M. Sglavo: Viscous Flow Flash Sintering of Porous Silica Glass, *Journal of Non-Crystalline Solids*; 476, 2017: 60-66.

M. Frasnelli, V.M. Sglavo: Flash sintering of tricalcium phosphate (TCP) bioceramics, *Journal of European Ceramic Society*; 38(1), 2018: 279-285.

R.S. Pillai, M. Frasnelli, V.M. Sglavo: HA/β-TCP Plasma Sprayed Coatings on Ti Substrate for Biomedical Applications, *Ceramics International*; 44(2), 2018: 1328-1333.

Participation to Congresses, Schools and Workshops

39th International Conference & Expo on Advanced Ceramics & Composites (ICACC 2015), American Ceramic Society, Daytona Beach (Florida, USA), 25 – 30 January 2015. *Oral presentation*: α-β Phase Transformation in Tricalcium Phosphate (TCP) Ceramics: Effect of Mg^{2+} Doping.

14th International Conference European Ceramic Society (ECERS 2015), European Ceramic Society, Toledo (Spain), 21 – 25 June 2015. *Oral presentation*: Effect of Mg^{2+} Doping on β-α Phase Transition in Tricalcium Phosphate (TCP) Ceramics.

Electric Field Assisted Sintering and Related Phenomena Far from Equilibrium (EFAS) - ECI conference, Tomar (Portugal), 6 – 11 March 2016. *Poster presentation*: Flash Sintering of β-TCP Bioceramics.

15th Conference & Exhibition of the European Ceramic Society (ECERS 2017), European Ceramic Society, Budapest (Hungary), 9-13 July 2017. *Oral presentation*: Flash sintering of TCP bioceramics.

Cermodel 2017 – Modelling and simulation meet innovation in ceramics technology, DICAM Unitn, Trento, 26-28 July 2017. *Oral presentation*: Model for flash sintering of TCP bioceramics.

Teaching Activities

November 2014 – February 2015: supervision of LT undergraduate, F. D'Incau: "Trattamento termico secondario sul tricalcio fosfato, TCP: effetto di ioni dopanti Mg^{2+}".

October – December 2014: tutoring within the Course of Ceramics Engineering and Processing - a.y. 2014 / 2015 (prof. V.M. Sglavo): "Effetto della temperatura di sinterizzazione su microstruttura, porosità e proprietà meccaniche dell'idrossiapatite" and "Sinterizzabilità e proprietà meccaniche di allumina tenacizzata con zirconia (ZTA)".

March – July 2015: supervision of LT undergraduate, G. Rossato: "Durezza e resistenza meccanica a flessione di provini in tricalcio fosfato dopato con Mg^{2+} temprati in aria".

March - November 2015: supervision of LT undergraduate, E. Bissoli: "Durezza e resistenza meccanica a flessione di provini in tricalcio fosfato dopato con Mg^{2+} raffreddati in maniera controllata".

October – December 2015: tutoring within the Course of Ceramics Engineering and Processing - a.y. 2015 / 2016 (prof. V.M. Sglavo): "Effect of Sintering Temperature on Microstructure, Porosity and Mechanical Properties of Hydroxyapatite HA" and "Sinterability, Microstructure and Mechanical Properties of Zirconia Toughened Alumina (ZTA)".

October – December 2016: tutoring within the Course of Ceramics Engineering and Processing - a.y. 2016 / 2017 (prof. V.M. Sglavo): "Effect of compaction pressure on microstructure and mechanical properties of HA bodies".

January – May 2017: supervision of LT undergraduate, A. Pedranz: "Sintesi e flash sintering di nanopolveri di tricalcio fosfato dopato con Mg^{2+}".

October – December 2017: tutoring within the Course of Ceramics Engineering and Processing - a.y. 2017 / 2018 (prof. V.M. Sglavo): "Effect of compaction pressure on microstructure and mechanical properties of HA bodies", "Production of alumina crucibles by slip casting: effect of processing parameters on final properties", and "Effect of processing conditions on alumina by tape casting".

Acknowledgments

Firstly, I would like to thank both my supervisors Prof. Vincenzo Maria Sglavo and Prof. Sandra Diré for their constant incentive, motivation and support throughout my Ph.D project, which gave me the possibility to join their research team and to access their laboratory resources. I would also like to express my gratitude to the Ph.D commission for their insightful comments and suggestions, which allowed me to improve my research work.

I thank my labmates and the technical staff for all the help and for the good moments we have spent in the last years. In particular, I am grateful to: Dr. Mattia Biesuz for the stimulating conversations, and for being a great fellow traveler; Dr. Mauro Bortolotti and Dr. Evgeny Borovin for the XRD assistance; Dr. Emanuela Callone for the NMR support; Alexia Conci e Livio Zottele for the kindliness with which they have always found a solution to my issues; and all the researchers and students who I have had the pleasure to collaborate with.

Last but not the least, I would like to thank my entire family and my dearest friends for their precious and strongly felt encouragement throughout this long academic path.